

# Non-Local/Local Gilbert Damping in Nickel and Permalloy Thin Films

Diplomarbeit

vorgelegt von

Jakob Walowski

aus

Ketrzyn

angefertigt im

IV. Pysikalischen Institut (Institut für  
Halbleiterphysik)  
der Georg-August-Universität zu Göttingen

2007



# Contents

1	Theoretical Foundations of Magnetization Dynamics	11
1.1	Magnetization Precession and Macro Spin	11
1.1.1	Quantum Mechanical Point of View	11
1.1.2	The Classical Equation of Motion	12
1.1.3	Connecting Classical and Quantum Mechanical Magnetic Moments	14
1.2	The Precession Damping	15
1.3	Energies Affecting Ferromagnetic Order	17
1.3.1	Exchange Energy	17
1.3.2	Magnetic Anisotropy Energy	18
1.3.3	Zeeman Energy	21
1.4	Spin Waves	21
1.5	The Angular Precession Frequency $\omega(\mathbf{H})$	22
1.5.1	Kittel Equation for the Experimental Geometry	24
1.6	Gilbert Damping in Experiments	26
2	The Experiments	31
2.1	Experimental Environment	31
2.2	The fs Laser Equipment	31
2.3	The Experimental Time-resolved MOKE Setup	32
2.4	Magneto-Optical Kerr Effect	34
2.4.1	Phenomenological Description	35
2.4.2	Microscopic Model	37
2.5	The Measurement Technique	38
2.5.1	Detection of the Kerr Rotation	39
2.5.2	The Time Resolved Kerr Effect	39
2.6	The Thermal Effect of the Pump Pulse	39
2.6.1	Laser-Induced Magnetization Dynamics	40
3	Sample Preparation and Positioning	43
3.1	UHV Vapor Deposition	43
3.2	Wedge Preparation	43
3.3	Alloyed Permalloy Samples	44
3.4	Positioning of the Wedge Samples in the Experimental Setup	45
4	The Experimental Results	47
4.1	Analysis of the Experimental Data	47
4.2	The Damping Mechanisms	48

4.2.1	Damping Processes . . . . .	48
4.2.2	Theoretical Models for Damping . . . . .	49
4.2.3	Non-local damping . . . . .	53
4.3	Results for the Non-Local Gilbert Damping Experiments . . . . .	57
4.3.1	The Intrinsic Damping of Nickel . . . . .	59
4.3.2	Non-local Gilbert Damping with Vanadium . . . . .	66
4.4	Results for the Local Gilbert Damping Experiments . . . . .	69
4.5	Chapter Summary . . . . .	75
5	Summary . . . . .	77
5.1	Future Experiments . . . . .	78
5.2	Other Techniques . . . . .	78

# List of Figures

1.1	The force $\mathbf{F}$ acting on a dipole in an external field $\mathbf{H}$ , taken from [24]	13
1.2	Magnetization torque ( <i>a</i> ) without damping, the magnetization $\mathbf{M}$ precesses around the $\mathbf{H}$ on a constant orbit. With damping ( <i>b</i> ) the torque pointing towards $\mathbf{H}$ forces the magnetization to align with the external field.	16
1.3	Polar system of coordinates	23
2.1	Pump laser, master oscillator, amplifier system and the expander/compressor box.	32
2.2	Scheme of the experimental setup for the TRMOKE experiments.	33
2.3	Possible MOKE geometries	34
2.4	Optical path through a thin film medium 1 of thickness $d_1$ and arbitrary magnetization direction. Taken from [29].	36
2.5	Transitions from $d$ to $p$ levels in transition metals (left) and the corresponding absorption spectra for photon energies $h\nu$ (right). Taken from [3].	38
2.6	Demagnetization by increase of temperature.	40
2.7	Laser-Induced magnetization dynamics within the first ns.	41
3.1	Schematic illustration of the nickel reference sample (Si/ $x$ nm Ni).	43
3.2	Schematic depictions of the prepared nickel vanadium samples. The Si/ $x$ nm Ni/3 nm V/1.5 nm Cu sample left and the Si/8 nm Ni/ $x$ nm V/2 nm Cu right.	44
3.3	Reflection measurement along the wedge profile.	45
4.1	Magnetization orientations of the $s$ and $d$ electrons with spin-flip scattering (right) and without spin-flip scattering (left).	51
4.2	Model of non-local damping for a ferromagnetic layer F of thickness $d$ between two normal metal layers N of thickness $L$ in an effective field $\mathbf{H}_{eff}$ (N/F/N). The precessing magnetization in the ferromagnetic layer is $\mathbf{m}$ .	54
4.3	Spectra measured for the nickel reference wedge Si/ $x$ nm Ni at 150 mT external field oriented $30^\circ$ out of plane. For nickel thicknesses $2 \text{ nm} \leq x \leq 22 \text{ nm}$ and their fits.	58
4.4	Precession frequencies for different external fields, left and the anisotropy field $H_{ani}$ deduced from the Kittel fit, plotted as a function of the nickel thickness from 1 nm – 22 nm, for the Si/ $x$ nm Ni sample.	60

4.5	The damping parameter $\alpha$ in respect of the nickel film thickness for the Si/ $x$ nm Ni sample, plotted for different external magnetic fields oriented $30^\circ$ out-of-plane. . . . .	60
4.6	The ripple effect. Spins are not aligned parallel anymore, the directions are slightly tilted. A schematic drawing (left). Kerr images of magnetization processes in a field rotated by $168^\circ$ and $172^\circ$ from the easy axis in a Ni <sub>81</sub> Fe <sub>19</sub> (10 nm)/Fe <sub>50</sub> Mn <sub>50</sub> (10 nm) bilayer (right), taken from [5]. . . . .	61
4.7	The fit to the measured data at 10 nm nickel layer thickness using a single sine function, compared to the artificially created spectra by the superposed functions with a frequency spectrum broadened by 5% and 7% (left). The frequencies involved into each superposition (right). The frequency amplitudes are divided by the number of frequencies involved. . . . .	62
4.8	Damping parameter $\alpha$ extracted from the measured data at 40 nm Ni, compared to the damping parameter calculated for the simulated artificial dataset from the superposed function for the 4 nm Ni. . . . .	63
4.9	Kerr microscopy recordings of the Si/ $x$ nm Ni sample with the external field applied in plane, along the wedge profile, provided by [12]. . . . .	65
4.10	Spectra for varied nickel thickness from 1 – 28 nm measured on the Si/ $x$ nm Ni/3 nm V/1.5 nm Cu sample with a constant 3 nm vanadium layer (left) and on the sample Si/8 nm Ni/ $x$ nm V/2 nm Cu, with a constant 8 nm nickel layer and varied vanadium thickness from 0 – 6 nm (right) measured in an external field $H_{ext} = 150$ mT oriented $30^\circ$ out of plane. . . . .	66
4.11	The precession frequencies $\nu$ for different external fields $H_{ext}$ (left) and the anisotropy fields $H_{ani}$ (right) in respect of the vanadium layer thickness, measured on the Si/8 nm Ni/ $x$ nm V/2 nm Cu sample. . . . .	67
4.12	The precession frequencies $\nu$ for different external fields $H_{ext}$ (left) and the anisotropy fields $H_{ani}$ (right) in respect of the nickel layer thickness, measured on the Si/ $x$ nm Ni/3 nm V/1.5 nm Cu sample. . . . .	68
4.13	The damping parameters $\alpha$ of the two samples. On the left side for varied nickel thicknesses with a constant vanadium damping layer thickness (Si/ $x$ nm Ni/3 nm V/1.5 nm Cu) and on the right side for a constant nickel layer thickness with a varied vanadium damping layer thickness (Si/8 nm Ni/ $x$ nm V/2 nm Cu). . . . .	69
4.14	Spectra of three differently doped permalloy samples at the same external magnetic field, 150 mT and $30^\circ$ out-of-plane. The beginning amplitudes of the three spectra are scaled to the same value. . . . .	70
4.15	Spectra for the 12 nm pure permalloy sample measured in different external fields, in the $30^\circ$ out-of-plane geometry and their fits. . . . .	71
4.16	Precession frequencies for the differently doped permalloy samples, extracted from the measured spectra. . . . .	72
4.17	Anisotropy fields $H_{ani}$ for the different impurities and amounts. . . . .	72
4.18	The damping parameter $\alpha$ for the permalloy samples with different doping. Calculated using equation 4.3. . . . .	73

---

4.19 Comparison of the mean damping parameters for the differently doped samples. . . . . 73



# Introduction

Almost every device or electronic gadget from pocket knife to cellphone has the capacity to store data, whether this may be useful or not. Furthermore, we, the users of e.g. hard drive based mp3/multimedia-players want to download as much music as possible, and, in future, even movies in the shortest possible time. This desire requires the development of faster reacting devices, in other words, hard drives with the ability to switch magnetization directions faster and faster. In order to be able to develop such devices more knowledge about the behavior and the properties of magnetization dynamics is needed.

The nanosecond regime is the timescale, that will be approached by magnetic memory devices in near future. For that reason fundamental research and knowledge of the magnetization behavior in this area is necessary. All-optical pump-probe experiments with ultra short laser pulses in the femtosecond-range are a powerful tool to gain an inside view into the behavior of the magnetization in ferromagnets on timescales up to one nanosecond after excitation. The experimental setup usually works, briefly described, as follows. A ferromagnetic sample is located in a constant external magnetic field. This external field forces the sample magnetization to line up with it. Two laser pulses, one a pump pulse, the other a probe pulse, arrive time delayed at the surface of the ferromagnetic sample. First the pump pulse excites the electrons. This excitation results in a process called demagnetization. Then the magnetization dynamics is followed by the probe pulse with a time delay constantly growing up to one nanosecond after demagnetization. This change is measured by the magneto-optical Kerr effect (MOKE) which is a common technique used by researchers studying the properties of thin film ferromagnetic materials.

What can be observed in these experiments is also a precession of the magnetization around its original direction. This precession is damped, and leads to the alignment of the magnetization  $M$  with the external field  $H$ , pointing in the original direction. This process is described by the LANDAU-LIFSHITZ-GILBERT equation, the equation of motion for spins. The damping limits the speed of the magnetization switching, therefore it is important to investigate it. In order to be able and compare different measurement techniques, magnetization damping is expressed by the dimensionless GILBERT-DAMPING parameter  $\alpha$ . An interesting fact is that the GILBERT-DAMPING can be affected by nonmagnetic damping materials. This gives two possibilities, how these damping materials can be applied. They can be either alloyed into the ferromagnetic layer (local GILBERT-DAMPING) or they can be positioned as a separate layer on top of the ferromagnetic layer (non-local GILBERT-DAMPING).

This thesis examines both these methods of damping enhancement. First the intrinsic damping of nickel is introduced. For this purpose, a nickel-wedge has been

prepared, to investigate the dependence of  $\alpha$  on the nickel thickness. After this, a nickel wedge with a constant vanadium layer on top will be discussed, to provide the dependency of the damping on the nickel thickness. Additionally a constant nickel layer, covered with a vanadium wedge will give some information about the dependency of damping on the damping layer thickness. These last two samples exemplify non-local Gilbert damping. Besides this, the damping of permalloy samples alloyed with different amounts of palladium and dysprosium as damping material is investigated. These will give some understanding of the local Gilbert damping mechanism.

The first chapter of this thesis gives an overview about the theoretical background of magnetization dynamics. It introduces the Landau-Lifshitz-Gilbert equation from the quantum mechanical as well as from the classical point of view. Damping is introduced in a phenomenological way. Further, the precession frequency and the damping parameter  $\alpha$  are analyzed for the specifications of the examined samples.

The second chapter describes the composition of the experimental setup and how the components work with and depend on each other. In addition to this, this chapter is devoted to the measuring techniques used in the experiments, the magneto-optical Kerr-effect (MOKE) and the time resolved MOKE.

The third chapter shortly introduces the analyzed samples, by giving information about the production process and techniques. Apart from this, the samples geometrical characteristics and layer properties are explained.

In the fourth chapter, first the theoretical models for the processes involved into magnetization precession damping are given, and then the experimental data is introduced and analyzed. Beginning with the non-local Gilbert damping measurement results, and then inspecting and discussing the results of the local damping measurements.

The final fifth chapter gives an outlook, to provide a context for this thesis. Furthermore, it gives a short outline about samples that can be examined to continue this work and other experiments, that can broaden the knowledge about the magnetization dynamics.

# 1 Theoretical Foundations of Magnetization Dynamics

## 1.1 Magnetization Precession and Macro Spin

The following chapter will introduce the phenomenon of magnetization precession from the quantum mechanical point of view and connect it to the magnetization precession derived from classical electrodynamics.

### 1.1.1 Quantum Mechanical Point of View

In practice it is generally not possible to observe the precession of a single electron spin. Therefore the **MACRO SPIN-APPROXIMATION** is used to describe the precession of magnetization. This model assumes that the exchange energy couples all spins of a sample strongly enough to act as one large single spin. According to quantum mechanics, the spin is an observable, represented by an operator  $\mathbf{S}$ . In order to gain the time evolution of  $\mathbf{S}$ , the Schrödinger equation needs to be stated in the Heisenberg picture [17]. In this case the time derivation of the mean value of  $\mathbf{S}$  equals the commutator of  $\mathbf{S}$  with the Hamiltonian  $\mathcal{H}$ . The equation of motion is then derived, as was done in [15], and reads

$$i\hbar \frac{d}{dt} \langle \mathbf{S} \rangle = \langle [\mathbf{S}, \mathcal{H}] \rangle. \quad (1.1)$$

If the spin interacts with a time dependent external magnetic field one can describe the system using the Zeeman Hamiltonian

$$\mathcal{H} = -\frac{g\mu_B}{\hbar} \mathbf{S} \cdot \mathbf{B}, \quad \text{where } \mathbf{B} = \mu_0 \mathbf{H}. \quad (1.2)$$

We will discuss the prefactor of the dot product later and concentrate on the commutator for now. First the commutator can be expressed giving the full components:

$$[\mathbf{S}, \mathcal{H}] = -\frac{g\mu_B}{\hbar} \begin{pmatrix} [S_x, S_x B_x + S_y B_y + S_z B_z] \\ [S_y, S_x B_x + S_y B_y + S_z B_z] \\ [S_z, S_x B_x + S_y B_y + S_z B_z] \end{pmatrix} \quad (1.3)$$

Where the  $S_i$  and  $B_i$  with  $i = x, y, z$  are time dependent. Then the expression of the commutator can be summed up to

$$[\mathbf{S}, \mathcal{H}] = -\frac{g\mu_B}{\hbar} \begin{pmatrix} B_y [S_x, S_y] + B_z [S_x, S_z] \\ B_x [S_y, S_x] + B_z [S_y, S_z] \\ B_x [S_z, S_x] + B_y [S_z, S_y] \end{pmatrix}. \quad (1.4)$$

With the commutator relations

$$[S_x, S_y] = i\hbar S_z, \quad [S_y, S_z] = i\hbar S_x, \quad [S_z, S_x] = i\hbar S_y, \quad (1.5)$$

a simple cross product relation is obtained:

$$[\mathbf{S}, \mathcal{H}] = -\frac{g\mu_B}{\hbar} i\hbar \begin{pmatrix} B_y S_z - B_z S_y \\ B_z S_x - B_x S_z \\ B_x S_y - B_y S_x \end{pmatrix}, \quad (1.6)$$

which finally transforms to the equation of motion for a single spin:

$$\frac{d}{dt} \langle \mathbf{S} \rangle = \frac{g\mu_B}{\hbar} (\langle \mathbf{S} \rangle \times \mathbf{B}). \quad (1.7)$$

### 1.1.2 The Classical Equation of Motion

The equation of motion can additionally be derived from classical mechanics. Starting with the dipole moment of a current loop as in [24]

$$|\mathbf{m}| = \mu_0 I S, \quad (1.8)$$

with  $I$  being the current and  $S$  the area inside of the loop. The current can also be seen as a charge  $q$  moving with the angular frequency  $\omega$  along the loop  $I = q \cdot \omega / 2\pi$ . The area enclosed in this loop of radius  $r$  is  $S = r^2 \pi$ . This leads to the equation in vector form

$$\mathbf{m} = \frac{q\mu_0}{2} r^2 \boldsymbol{\omega}. \quad (1.9)$$

Promptly, by assigning the charge  $q = -e$  for an electron, and since its position with respect to the center of the loop is  $\mathbf{r}$ , and its velocity  $\mathbf{v}$ , and knowing  $\mathbf{v} = \boldsymbol{\omega} \times \mathbf{r}$  the relation

$$\mathbf{m} = -\frac{e\mu_0}{2} (\mathbf{r} \times \boldsymbol{\omega}) \quad (1.10)$$

is obtained. In analogy to classical mechanics, where the angular momentum  $\mathbf{l}$  of a mass  $m_e$  circulating around the origin is

$$\mathbf{l} = m_e (\mathbf{r} \times \mathbf{v}) = m_e r^2 \boldsymbol{\omega}. \quad (1.11)$$

The magnetic momentum can now be expressed in terms of the classical momentum of a circulating electron by combining the last two momenta. Consequently, the classical relation

$$\mathbf{m} = -\frac{e\mu_0}{2m_e} \mathbf{l} \quad (1.12)$$

is acquired. In this case, the momentum  $\mathbf{m}$  can be imagined as two magnetic charges  $p^+$  and  $p^-$  separated by a distance  $d$  being placed in line perpendicular to an external

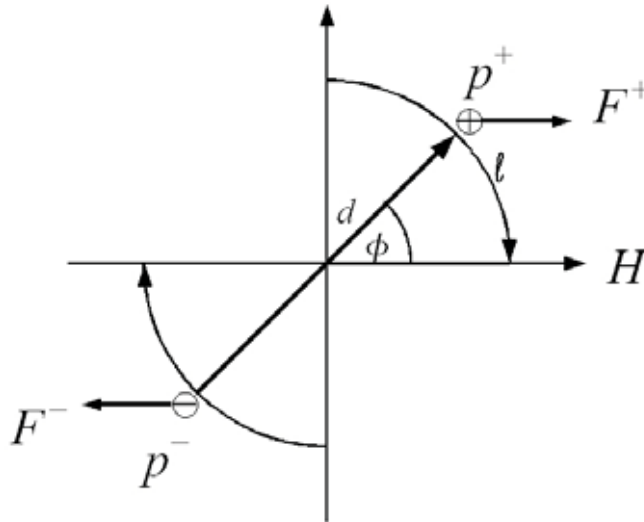


Figure 1.1: The force  $F$  acting on a dipole in an external field  $H$ , taken from [24]

field  $H$ , as depicted in figure 1.1. Under these circumstances, a force  $F^+ = p^+ H$  and, respectively,  $F^- = p^- H$  is acting on each charge. The net force adds up to zero, but a resulting torque  $T$  causes a rotation of the dipole towards the direction of the external magnetic field. Finally the mechanical torque defined by

$$\mathbf{T} = \mathbf{r} \times \mathbf{F}. \quad (1.13)$$

This implies, that a momentum exposed to a force experiences a torque demanding the change of its direction. That the torque acting on a magnetic momentum  $m$  is given by an equation similar to the definition above from classical mechanics, as was derived in [24]

$$\mathbf{T} = \mathbf{m} \times \mathbf{H}. \quad (1.14)$$

Moreover, per definition, the torque is the change of the momentum with time  $\frac{d\mathbf{l}}{dt} = \mathbf{T}$ . Combining this fact with equation 1.14 yields to

$$\frac{d\mathbf{l}}{dt} = \mathbf{T} = \mathbf{m} \times \mathbf{H}. \quad (1.15)$$

Finally, as can be seen from equation 1.12, the magnetic momentum can be expressed in terms of the angular momentum by a vector quantity. The relation is  $\mathbf{m} = \gamma \mathbf{l}$  with  $\gamma = -\frac{eg\mu_0}{2m_e} = -\frac{g\mu_B\mu_0}{\hbar}$ . All that needs to be done now is to substitute  $\mathbf{l}$  and rewrite equation 1.15 as

$$\frac{d\mathbf{m}}{dt} = \gamma[\mathbf{m} \times \mathbf{H}] = \gamma\mathbf{T}. \quad (1.16)$$

In the end one question remains open: How does this equation transform for a spin momentum? As will be seen in the next section, quantum mechanics is needed to answer this question.

### 1.1.3 Connecting Classical and Quantum Mechanical Magnetic Moments

Equations 1.7 and 1.16 have a similar form, the difference between these two being that, the former holds for a quantum mechanical spin, while the latter is derived in the classical way for a magnetic moment. But still the explanation is missing, how these two fit together. In other words, how equation 1.12 can be translated into quantum mechanics.

In quantum mechanics the value of  $l$  cannot be measured directly, but only the projection along the z axis, defined by the direction of the external field  $\mathbf{H}$ . This axis is also called the quantization axis. Therefore, only the expectation value of  $\langle l_z \rangle = \hbar l_z$  for a single electron is detectable. This yields in the quantum relation for the magnetic moment

$$\langle m^z \rangle = -\frac{e\mu_0}{2m_e} \hbar l_z \quad (1.17)$$

where the prefactor  $\frac{e\mu_0 \hbar}{2m_e} = \mu_B$  is the BOHR MAGNETON. It has the same units as the magnetic moment, so that the magnetic moment can be expressed in units of  $\mu_B$ .

Relation 1.17 describes the quantum mechanical orbital magnetic momentum, which can be expressed by its expectation value

$$\langle m_o^z \rangle = -\frac{\mu_B}{\hbar} \langle l_z \rangle. \quad (1.18)$$

In addition to the revolution on an orbit, the electron rotates around its own axis. This motion causes an intrinsic angular momentum called spin. The spin has a half-integer quantum number  $s = \frac{\hbar}{2}$  and its observable projections are  $s_z = \pm \frac{\hbar}{2}$ . One important fact about the electron spin is that it generates a magnetic momentum of a full Bohr magneton  $\mu_B$ , even though it has only a spin of  $\frac{\hbar}{2}$ . Thus, the magnetic moment for the spin reads

$$\langle m_s^z \rangle = -\frac{2\mu_B}{\hbar} \langle s_z \rangle. \quad (1.19)$$

In analogy to the orbital momentum the measured value of  $m_s$  is determined by the expectation value of the spin  $\langle s_z \rangle$  along the quantisation axis. On closer inspection the spin does not generate one full magnetic moment in terms of  $\mu_B$ . That's why the factor 2 in equation 1.19 has to be corrected by  $g = 2.002319304386$  for a free electron. The exact value for the gyro magnetic moment  $g$  has to be determined from the relativistic Schrödinger equation for a given environment. In solids the value of  $g$  can even go up to 10. Using the  $g$ -factor the term for  $m_s$  can be rewritten by

$$\langle m_s^z \rangle = -\frac{g\mu_B}{\hbar} \langle s_z \rangle. \quad (1.20)$$

The final step for obtaining the total magnetic moment  $\langle m_{tot} \rangle$  is simply adding the orbital and the spin moment.

Now that the connection of the classical and the quantum mechanical magnetic moment is accomplished, a subsequent examination of equation 1.16 can follow. To

start with, equation 1.16 can be identified as equivalent to equation 1.7. The difference in the notation comes from the assumption that the orbital momentum is about  $10^3$  weaker than spin momentum, so that solely the spin is relevant for the following observations. The other difference is the prefactor, since  $\mathbf{m} = \gamma \mathbf{s}$  we obtain the change of the magnetic momentum in

$$\frac{d\mathbf{m}}{dt} = -\gamma[\mathbf{m} \times \mathbf{H}], \quad (1.21)$$

where all subscripts of the total magnetic moment are neglected.

Before the final conclusions of equation 1.21 are drawn we will rearrange it one last time. For this we need the magnetization  $\mathbf{M}$ , defined as the sum of all magnetic moments per unit volume

$$\mathbf{M} = \frac{\sum \mathbf{m}}{V}. \quad (1.22)$$

The MACRO-SPIN model as mentioned in section 1.1.1 holds, since many magnetic moments within a volume are examined. For these moments it is assumed to precess rigidly coupled in the considered volume. At last equation 1.21 can be written for the magnetization  $\mathbf{M}$

$$\frac{d\mathbf{M}}{dt} = -\gamma[\mathbf{M} \times \mathbf{H}]. \quad (1.23)$$

This final equation is the LANDAU-LIFSHITZ equation of motion and describes the motion only phenomenologically.

Since the change of the magnetization  $d\mathbf{M}$  is perpendicular both to  $\mathbf{M}$  and  $\mathbf{H}$ , in a constant external magnetic field the following relations hold:

$$\frac{d}{dt}\mathbf{M}^2 = 0, \quad \frac{d}{dt}[\mathbf{M} \cdot \mathbf{H}] = 0. \quad (1.24)$$

This means that  $\mathbf{M}$  precesses around the direction of  $\mathbf{H}$  as shown in figure 1.2a).

The frequency of this precession is  $\omega = \gamma H$  where  $H$  is the amount of  $\mathbf{H}$ . This frequency is known as the LARMOR-FREQUENCY of the LARMOR-PRECESSION and is independent from the angle between  $\mathbf{M}$  and  $\mathbf{H}$ . For a free electron it is  $\omega = 28 \text{ MHz/mT}$ , which means that in a field of 1 T the magnetic moment needs  $\sim 36 \text{ ps}$  for one full precession.

## 1.2 The Precession Damping

A simple model for precession damping can be found, on much larger time and length scales, in a compass (a device with which most of those of us who went out camping in the wild before the days of GPS will be quite familiar).

The compass needle is nothing but a magnetic dipole suspended in the earth's magnetic field. Once the needle is turned out of its stationary position, it returns back, but not immediately. It swings back and forth around the magnetic fields direction.

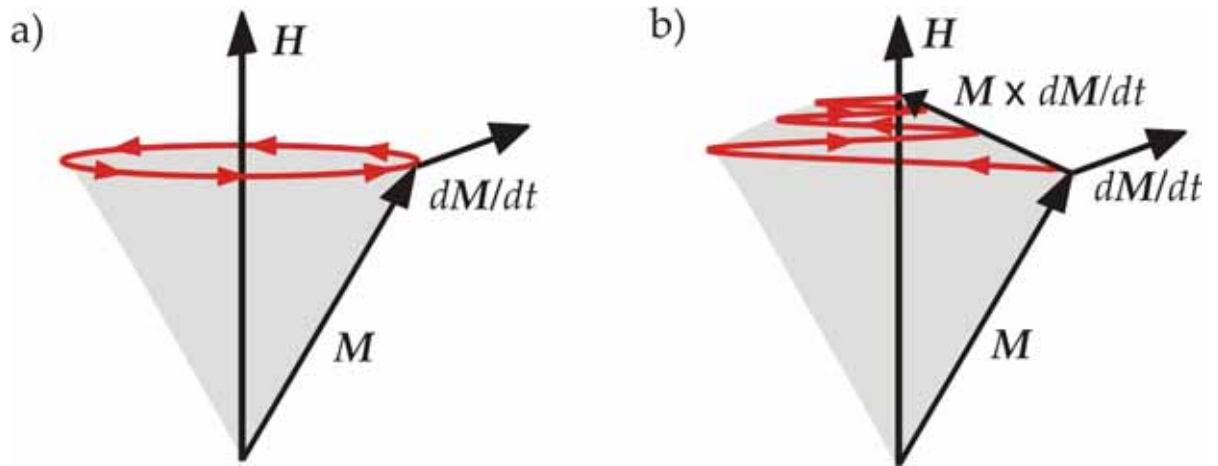


Figure 1.2: Magnetization torque (a)) without damping, the magnetization  $M$  precesses around the  $H$  on a constant orbit. With damping (b)) the torque pointing towards  $H$  forces the magnetization to align with the external field.

For a small compass needle the magnetic field of the earth is considered, locally and temporally, constant. The oscillation back and forth is like the precession of the magnetization derived in equation 1.23. But eventually the motion decays and the needle stays aligned showing in the direction of the external field. The example is a little inappropriate, because the damping of the compass needles motion is purely mechanical through the attachment to the rest of the compass device. Spin damping has different causes, as will be discussed later on. However, the effect can in both cases be described by adjusting equation 1.23. Recalling figure 1.2b) one can see that a further torque  $T_D$  is needed the direction of which needs to be perpendicular to  $M$  and to its temporal change. So the torque providing the damping reads

$$\mathbf{T}_D = \frac{\alpha}{\gamma M_s} \left[ \mathbf{M} \times \frac{d\mathbf{M}}{dt} \right]. \quad (1.25)$$

Here, the dimensionless prefactor  $\alpha$  is of purely phenomenological nature and can be determined from experiments. The torque is weaker for bigger saturation magnetization  $M_s$ . Inserting this torque into the LANDAU-LIFSHITZ equation it adds up to the LANDAU-LIFSHITZ-GILBERT (LLG) equation of motion

$$\frac{d\mathbf{M}}{dt} = -\gamma [\mathbf{M} \times \mathbf{H}] + \frac{\alpha}{M_s} \left[ \mathbf{M} \times \frac{d\mathbf{M}}{dt} \right] \quad (1.26)$$

In equation 1.26 the dimensionless parameter  $\alpha$  is called the GILBERT damping parameter.

Comparing equation 1.26 to the Landau-Lifshitz equation 1.23 one can deduce that the effective (resulting) field which determines magnetization dynamics depends on  $\frac{d\mathbf{M}}{dt}$ . This means that the magnetization motion causes another magnetic field, so

that  $\mathbf{H}$  is not the only magnetic field present, but can be imagined as an effective (resulting) field, which reads

$$\mathbf{H}_{res} = \mathbf{H} - \frac{\alpha}{\gamma M_s} \frac{d\mathbf{M}}{dt}. \quad (1.27)$$

Inserting  $\mathbf{H}_{res}$  into equation 1.23 also provides the LANDAU-LIFSHITZ-GILBERT equation. Although one has to be careful with the expression "effective field" because, as will be depicted in the next section, there are more mechanisms contributing to the final effective field. That's why the indication "resulting" field has been chosen in this place.

### 1.3 Energies Affecting Ferromagnetic Order

The magnetization direction of a ferromagnet is not necessary dominated by the applied field. There are several other energies accounting for the resulting magnetization direction. That means that a ferromagnetic samples magnetization might not point in the direction of the applied field, but depends on the energy landscape in total. Every energy is responsible for a magnetic field with a characteristic strength and direction. On that account all fields add up to form an effective field

$$\mathbf{H}_{eff} = \mathbf{H}_{ex} + \mathbf{H}_{magn-crys} + \mathbf{H}_{shape} + \mathbf{H}_{ext}. \quad (1.28)$$

The fields are the following. First, this is the strongest, is the exchange field  $\mathbf{H}_{ex}$  resulting from the exchange energy. This energy causes the spins to align parallel to each other. Second there is  $\mathbf{H}_{magn-crys}$  the field resulting from the magneto-crystalline anisotropy. This energy defines with  $\mathbf{H}_{shape}$  the easy axis of a material. Finally, there is  $\mathbf{H}_{ext}$  the applied magnetic field. Its interaction with the magnetization of the sample is described by the Zeeman energy term.

#### 1.3.1 Exchange Energy

The cause for the exchange interaction traces back to the Pauli-Principle. It states for fermions that there cannot be two particles matching in all their quantum numbers. Therefore, two electrons with spins  $\mathbf{s}_i$  and  $\mathbf{s}_j$  have always an energy difference. This difference arising from the electron correlation is expressed by the Heisenberg-Hamiltonian:

$$\mathcal{H}_{heis} = - \sum_{i \neq j}^N J_{ij} \mathbf{s}_i \cdot \mathbf{s}_j = -2 \sum_{i < j}^N J_{ij} \mathbf{s}_i \cdot \mathbf{s}_j \quad (1.29)$$

with  $J_{ij}$  being the exchange integral of the two electrons represented by the spin operators  $\mathbf{s}_i$  and  $\mathbf{s}_j$ . Because of the symmetry of the exchange integral  $J_{ij} = J_{ji}$  the Heisenberg-Hamiltonian can be simplified and multiplied by 2 as was done on the right side of the equation. From the Heisenberg-Hamiltonian can be recognized that

the energy is minimal with  $J_{ij} > 0$  for ferromagnetic coupling and with  $J_{ij} < 0$  for anti ferromagnetic coupling. The exchange interaction is very short ranged because the wave functions overlap only for the distance of two atoms. In consequence, increasing the atom distance  $J_{ij}$  decreases. This fact justifies the summation over the nearest neighbors and neglecting the influence of further distanced electrons. With this assumption  $J_{ij}$  can be connected to the Weiss field by considering the energy of an atomic moment [24]. By doing this, the spin alignment of a ferromagnet can be described by its temperature dependence. Then  $\sum_j J_{ij} = J_0$  for materials consisting of identical atomic spins. In this case the exchange parameter  $J_0$  corresponds to

$$J_0 = \frac{3k_B T_C}{2zs(s+1)} \quad (1.30)$$

where  $T_C$  is the Curie-temperature,  $z$  the number of nearest neighbors and  $s$  the total number of spins. At this point it is clear that, the higher  $T_C$  for a specific material, the stronger is also the coupling of the spins and the spins are more likely to align parallel or anti parallel, respectively according to the behavior ferromagnetic or anti ferromagnetic materials.

In order to calculate the exchange energy of the whole sample the sum of equation 1.29 needs to be replaced by an integral over the volume of the sample and the spins have to be extended to a continuous magnetization. Then

$$E_{ex} = A \int_V (\nabla \mathbf{m})^2 dV \quad (1.31)$$

with  $A = \frac{2Js^2}{a}$  as the material-specific exchange constant,  $a$  the lattice constant and  $\mathbf{m} = \frac{\mathbf{M}}{M_s}$  the magnetization normalized to the saturation magnetization of the ferromagnetic material. Finally the exchange field can be composed as the gradient of the exchange energy density differentiated by the magnetization vector

$$\mathbf{H}_{ex} = \vec{\nabla}_m (e_{ex}). \quad (1.32)$$

The exchange energy is responsible for the long range ordering between atoms and is needed to flip the spin of one atom aligned with the mean field of all other atoms in a volume of a material.

### 1.3.2 Magnetic Anisotropy Energy

The previously mentioned exchange energy accounts in particular for the alignment of spins in the same direction, but the definition of this direction is still missing. Therefore, a closer look at the anisotropy of solids is indispensable. Experiments show that there exists a specific direction along which the magnetization aligns easier than along other directions. Therefore two axes are introduced. First the easy axis, along which the magnetization in a sample prefers to align. Second the hard axis, the axis along

which energy needs to be expended to align the magnetization along it, e.g. by applying an external field along this direction. In short, the magnetic anisotropy is the energy needed to turn the magnetization of a ferromagnet from the easy to the hard axis.

In the following, the magnetic anisotropies, which originate from the crystal structure and the shape of the samples are described. These anisotropy builders can only be treated as polar vectors, thus no anisotropy direction exists, just a unique axis. This unique axis is usually parallel to the sample normal for thin films. The angle  $\theta$  is enclosed by the saturation magnetization  $M_s$  and the unique axis. The energy density  $e_{ani}$  for the conversion of the magnetization can be developed into a series of even powers of projection on the unique axis [24]

$$e_{ani} = K_1 \sin^2 \theta + K_2 \sin^4 \theta + K_3 \sin^6 \theta + \dots \quad (1.33)$$

Remarking that this depiction is only a series expansion with  $K_i$  ( $i = 1, 2, 3, \dots$ ) representing the anisotropy constants of dimension energy per volume, usually calculated with the unit J/cm<sup>3</sup>.

The anisotropy field can be derived as

$$H_{ani} = \frac{2K_1}{M_s} \cos \theta, \quad (1.34)$$

by neglecting the higher order terms [24]. For thin films the unique axis is usually defined as the surface normal, enclosing the angle  $\theta$  with the magnetization. For magnetization along the sample surface it delivers  $\theta = 90^\circ$ . This makes two cases possible, first, when  $K_1 > 0$  the easy axis is along the surface normal also called out-of-plane anisotropy and second when  $K_1 < 0$  the easy axis is parallel to the surface itself, also called in-plane anisotropy.

There are two main contributions to the anisotropy in thin films. The first is the magnetocrystalline anisotropy, arising from the atomic structure and the bonding in the thin film, that means the spin orbit interaction. This anisotropy is represented by the magnetocrystalline anisotropy constant  $K_u$ . The second is the shape anisotropy, arising from the classical dipole interaction, as discussed below. This part of the anisotropy is represented by the constant  $K_s$ . With these contributions the anisotropy constant is given by  $K_1 = K_u + K_s$  and the first order term of the anisotropy energy density reads

$$e_{ani} = (K_u + K_s) \sin^2 \theta + \dots \quad (1.35)$$

Now whether a sample magnetizes in plane or out of plane is a question of the balance between these two anisotropies. As is shown in [24] multilayers tend to possess a large and positive  $K_u$ . This dominates the anisotropy and results in an out of plane magnetization. For single layered thin films on the other hand  $K_1$  is usually smaller than zero which results in an in plane magnetization.

### The Magneto-Crystalline Anisotropy

The magneto-crystalline anisotropy arises as already mentioned from the spin-orbit interaction [28]. This interaction couples the isotropic spin moment to an anisotropic

lattice. In band structure calculations this is expressed by the largest difference of the spin-orbit energy resulting from magnetizing the sample along the hard and the easy direction. Nevertheless it is usually rather difficult to calculate  $K_u$  because of the complexity of band structures and its dependence on the temperature, therefore it is often treated as an empirical constant derived from experiments by measuring magnetization curves or ferromagnetic resonance.

#### The Shape Anisotropy

As explained in [24] spins tend to align parallel due to the dominating exchange interaction. To minimize their energy even further two neighboring atomic moments align parallel along the internuclear axis. For thin films, this axis is commonly oriented along the surface, i.e. in-plane. The dominant energy density remaining here is the shape anisotropy. This is the anisotropy arising from the classical dipole interaction.

In the following the derivation of the shape anisotropy will be introduced. Considering a magnetized disk without an external field, the magnetization inside and outside of the disk can be expressed as

$$\mathbf{B} = \mu_0 \mathbf{H} + \mathbf{M}. \quad (1.36)$$

Now two fields can be obtained, namely  $\mathbf{H}_d = \frac{1}{\mu_0}(\mathbf{B} - \mathbf{M})$  inside the disk and  $\mathbf{H}_s = \frac{1}{\mu_0}\mathbf{B}$  outside the disk. The field inside the disk is labeled demagnetization field and the one outside is the stray field. Combining the Maxwell equation with Gauss' theorem it can be obtained that the conservation of law holds for the sum of  $\mathbf{H}$  and  $\mathbf{M}$  as follows

$$\nabla \cdot \mathbf{B} = \nabla \cdot [\mu_0 \mathbf{H} + \mathbf{M}] = 0. \quad (1.37)$$

Hence sinks and sources of  $\mathbf{M}$  act like positive and negative poles for the field  $\mathbf{H}$  it turns out

$$\mu_0 \nabla \cdot \mathbf{H} = -\nabla \cdot \mathbf{M}. \quad (1.38)$$

Here again the field  $\mathbf{H}$  inside and outside the sample is defined as above with a demagnetizing field and a stray field. The field outside the sample contains energy expressed by

$$E_d = \frac{\mu_0}{2} \iiint_{all\ space} \mathbf{H}^2 dV = -\frac{1}{2} \iiint_{sample} \mathbf{H}_d \mathbf{M} dV. \quad (1.39)$$

Using Stoke's theorem for  $\mathbf{H}_d$  and  $\mathbf{H}_s$  it shows up that they are equal. Further  $\mathbf{H}_d$  is almost 0 for in plane magnetization and goes up to  $\mathbf{H}_d = -\frac{\mathbf{M}}{\mu_0}$  for out of plane magnetization. However in general a demagnetizing factor  $N$  has to be stated, then the demagnetization field is

$$\mathbf{H}_d = -\frac{N}{\mu_0} \mathbf{M}. \quad (1.40)$$

This factor is  $N = 0$  for an in plane magnetized thin film and  $N = 1$  for an out of plane magnetized thin film. Finally, the shape anisotropy is given by

$$E_D = K_s = -\frac{1}{2\mu_0} M_s^2, \quad (1.41)$$

with  $M_s$  being the saturation magnetization. In the end this means, that the shape anisotropy energy is limited to the specific saturation magnetization value for every individual material.

### 1.3.3 Zeeman Energy

The last energy contribution to be discussed is the Zeeman Energy. This energy takes into account the interaction between the magnetization and the externally applied magnetic field. The energy term is given by

$$E_z = -\mu_0 \int_V \mathbf{M} \cdot \mathbf{H}_{ext} dV \quad (1.42)$$

The importance of this energy lies in the excitation of the magnetization by the external field. In the experiments described later,  $\mathbf{H}$  will cause the rotation of the magnetization out of the easy axis and make precession possible. Conclusively the Zeeman Energy works against the anisotropy energy. In the case that  $\mathbf{H}_{ext}$  is not along the easy axis, it has to be stronger (higher  $\mathbf{H}_{ext}$ ) in order to rotate the magnetization out of the easy axis. The magnetization will be tilted from the easy axis, depending on the strength and orientation of the applied field  $\mathbf{H}_{ext}$ .

## 1.4 Spin Waves

Experiments prove that the magnetization decreases at low temperatures,  $T \ll T_C$  in ferromagnets. This decrease cannot be explained by the Stoner excitation model, because the spin-flip energies in this model are too big. Therefore, there has to be another thermal excitation causing the decrease. In 1930 Felix Bloch suggested an excitation model based on the so called SPIN WAVES or MAGNONS. To understand the mechanism behind the spin waves, one has to begin with the Heisenberg model (exchange energy). According to this model, all spins should align parallel at low temperatures and when the maximum saturation magnetization is reached. However, the energy arising from two spins in the crystal, oriented under the angle  $\varepsilon$  to each other, and at the distance  $a$ , is given by

$$\Delta E = 2Js^2[1 - \cos \varepsilon] \approx Js^2\varepsilon^2. \quad (1.43)$$

From this equation follows, that there can be a lot of small excitation energies, which vanish with  $\varepsilon^2$ . Therefore, looking at a chain of  $N$  spins with every spin rotated by an angle  $\varepsilon$  to the next spin, the energy difference

$$\Delta E = NJs^2\varepsilon^2 \quad (1.44)$$

arises. Relative to the macro spin, where all spins precess in phase, the energy expressed in equation 1.44 describes the system in which spins precess with a constant

phase difference  $\varepsilon$ . The magnon wavelength can be defined as the number of spins it takes to acquire a  $360^\circ$  rotation. Because of this spin waves or magnons can be defined as the amount of spins precessing coherently around the magnetization  $M$ .

Going further, the model, which, so far, has been a classical one, must be combined with quantum mechanics [24] and the energy difference becomes

$$\Delta E = \hbar\omega = Ja^2k^2 = Dk^2 \quad (1.45)$$

with  $k = 2\pi/\lambda$  being the wave vector of the spin wave,  $a$  the lattice constant and  $D$  the spin wave stiffness. With decreasing  $k$  or increasing  $\lambda$ , the energy of the spin wave also decreases. For the  $k = 0$  mode, also called the the Kittel mode, the spins precess in phase and therefore can be treated as a single macro spin. This is also the case in the experiments presented below. Because the ferromagnetic layers of the examined samples are thin (1 – 20 nm) compared to the penetration depth, all spins throughout the thickness of the samples are excited and precess in phase.

In the end it can be summed up that spin waves or magnons have a particle character with an energy  $\hbar\omega$ , a linear momentum  $\hbar k$  and an even angular momentum  $\pm \hbar$ . For the latter property magnons are classified as bosons and obey Bose-Einstein statistics.

## 1.5 The Angular Precession Frequency $\omega(H)$

As mentioned before the experiments carried out within this diploma thesis deal with magnetization dynamics, which is based on the precession of spins. The recorded data allow the determination of spin precession frequency, which can be observed experimentally and, because of this, plays an important role in the analysis of the experiments. In this section the relation between the precession frequency and the energies involved, the dispersion relation for the Kittel mode, will be derived in similarity to [7].

It is a lot easier to to derive the dispersion relation considering the precession without damping. We will start by writing the LANDAU-LIFSHITZ equation 1.23 in polar coordinates. In particular this means, that the components  $M$  and  $H_{eff}$  in polar coordinates need to be found.

With a choice of coordinates according to figure 1.3, the magnetization vector  $M$  reads

$$\mathbf{M} = M_s \begin{pmatrix} \sin \theta \cos \varphi \\ \sin \theta \sin \varphi \\ \cos \theta \end{pmatrix}, \quad (1.46)$$

and its infinitesimal change is

$$d\mathbf{M} = M_s dr \mathbf{e}_r + M_s d\theta \mathbf{e}_\theta + M_s \sin \theta d\varphi \mathbf{e}_\varphi. \quad (1.47)$$

Where  $M_s$  is the saturation magnetization, the angles  $\theta$  and  $\varphi$  represent the new polar coordinates of  $M$  in reference to the cartesian system of coordinates. The effective

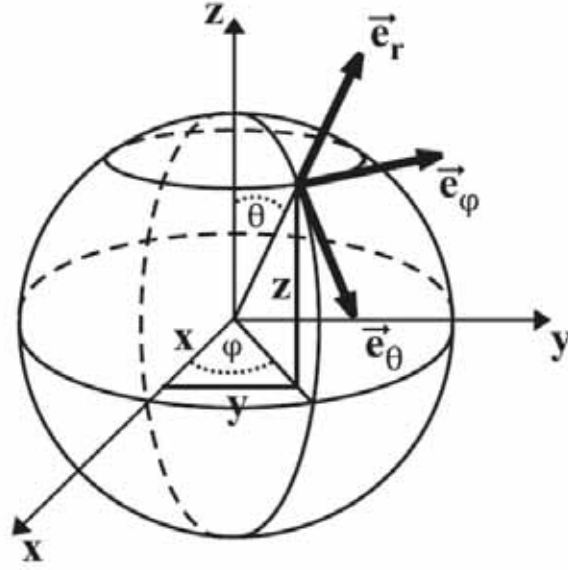


Figure 1.3: Polar system of coordinates

magnetic field can be obtained by the partial differentiation of the free magnetic energy  $F$  by the normalized magnetization  $\mathbf{m} = \mathbf{M}/M_s$  which reads

$$\mathbf{H}_{eff} = -\frac{1}{\mu_0 M_s} \frac{\partial F}{\partial \mathbf{m}}. \quad (1.48)$$

Changing to polar coordinates yields

$$\mathbf{H}_{eff} = -\frac{1}{\mu_0} \left( \frac{\partial F}{\partial r} \mathbf{e}_r + \frac{1}{M_s} \frac{\partial F}{\partial \theta} \mathbf{e}_\theta + \frac{1}{M_s \sin \theta} \frac{\partial F}{\partial \varphi} \mathbf{e}_\varphi \right). \quad (1.49)$$

With the help of these last three relations, the left hand side of equation 1.23 becomes

$$\frac{d\mathbf{M}}{dt} = M_s \frac{d\theta}{dt} \mathbf{e}_\theta + M_s \sin \theta \frac{d\varphi}{dt} \mathbf{e}_\varphi. \quad (1.50)$$

The first term vanishes because the total value of the magnetization is constant, only the direction changes. The right hand side requires some more manipulation, but finally yields to

$$\mathbf{M} \times \mathbf{H}_{eff} = M_s \frac{1}{\mu_0 \sin \theta} \frac{\partial F}{\partial \varphi} \mathbf{e}_\theta - \frac{1}{\mu_0} \frac{\partial F}{\partial \theta} \mathbf{e}_\varphi. \quad (1.51)$$

Finally the outcome is the LANDAU-LIFSHITZ equation 1.23 in polar coordinates

$$\frac{d\theta}{dt} = -\frac{\gamma}{\mu_0 M_s \sin \theta} \frac{\partial F}{\partial \varphi} \quad (1.52)$$

$$\frac{d\varphi}{dt} = \frac{\gamma}{\mu_0 M_s \sin \theta} \frac{\partial F}{\partial \theta}. \quad (1.53)$$

Next these expressions need to be simplified by expanding the free energy in a Taylor series up to the second order. Also note that the first order Taylor terms vanish, because the free energy is expanded for small  $\varphi$  and  $\theta$  around the equilibrium position  $\varphi_0$  and  $\theta_0$ , which is a minimum of  $F$ . The Taylor expansion reads then

$$F = F_0 + \frac{1}{2} \left[ \frac{\partial^2 F}{\partial \theta^2} \theta^2 + \frac{\partial^2 F}{\partial \theta \partial \varphi} \theta \varphi + \frac{\partial^2 F}{\partial \varphi^2} \varphi^2 \right]. \quad (1.54)$$

Inserting this approximation into the LANDAU-LIFSHITZ equation in polar coordinates leads to

$$\frac{d\theta}{dt} = -\frac{\gamma}{\mu_0 M_s \sin \theta} \left( \frac{\partial^2 F}{\partial \varphi^2} \varphi + \frac{\partial^2 F}{\partial \theta \partial \varphi} \theta \right) \quad (1.55)$$

$$\frac{d\varphi}{dt} = \frac{\gamma}{\mu_0 M_s \sin \theta} \left( \frac{\partial^2 F}{\partial \theta^2} \theta + \frac{\partial^2 F}{\partial \theta \partial \varphi} \varphi \right). \quad (1.56)$$

Now by choosing

$$\theta = \theta_0 + A_\theta \exp(-i\omega t) \quad (1.57)$$

$$\varphi = \varphi_0 + A_\varphi \exp(-i\omega t), \quad (1.58)$$

as the ansatz for small oscillations around the equilibrium for both angles, where  $A_\theta$  and  $A_\varphi$  compose the precession amplitude vector, the equation of motion is formed to

$$\left( \frac{\gamma}{\mu_0 M_s \sin \theta} \frac{\partial^2 F}{\partial \theta \partial \varphi} - i\omega \right) \theta + \frac{\gamma}{\mu_0 M_s \sin \theta} \frac{\partial^2 F}{\partial \varphi^2} \varphi = 0 \quad (1.59)$$

$$\frac{\gamma}{\mu_0 M_s \sin \theta} \frac{\partial^2 F}{\partial \theta^2} \theta + \left( \frac{\gamma}{\mu_0 M_s \sin \theta} \frac{\partial^2 F}{\partial \theta \partial \varphi} - i\omega \right) \varphi = 0. \quad (1.60)$$

This final set of homogeneous equations of motion 1.59 can only be solved non-trivially, when the following expression holds for the precession frequency

$$\omega = \frac{\gamma}{\mu_0 M_s \sin \theta} \sqrt{\frac{\partial^2 F}{\partial \theta^2} \cdot \frac{\partial^2 F}{\partial \varphi^2} - \left( \frac{\partial^2 F}{\partial \theta \partial \varphi} \right)^2}. \quad (1.61)$$

The precession frequency depends on the magnetic energies and their effective direction, given by the deviation angles  $\theta$  and  $\varphi$  from equilibrium.

This result having been derived, the next section deals with the question how the free energy  $F$  and the precession frequency  $\omega$  behave in the examined samples with respect to the sample geometry and the experimental setup.

### 1.5.1 Kittel Equation for the Experimental Geometry

In the experiments carried out during this thesis, the samples are exposed to a stationary external magnetic field. Initially, a pump laser pulse demagnetizes the sample

and causes the magnetization precession in the GHz regime back to its equilibrium position. This frequency is defined by  $\mathbf{H}_{eff}$ . In the macro spin approximation the effective field is composed from the external field  $\mathbf{H}_{ex}$ , the magneto-crystalline anisotropy field  $\mathbf{H}_{magn-cryst}$  and the shape anisotropy field  $\mathbf{H}_{shape}$ . The free energy  $F$  expressed in polar coordinates is considered with regard to the magnetization vector  $\mathbf{M}$  in equilibrium and takes the form

$$\begin{aligned} F = & -\mu_0 M_s (H_x \sin \theta \cos \varphi + H_y \sin \theta \sin \varphi + H_z \cos \theta) \\ & - K_x \sin^2 \theta \cos^2 \varphi - K_y \sin^2 \theta \sin^2 \varphi - K_z \cos^2 \theta \\ & + \frac{\mu_0}{2} M_s^2 \cos^2 \theta \end{aligned} \quad (1.62)$$

In order to calculate the derivatives needed for equation 1.61 from the free energy given by equation 1.62, some characteristics concerning the experimental setup have to be made. Firstly, the given angles are for small derivations out of the equilibrium position. Secondly, the external applied field can be rotated by  $\theta$  from  $0^\circ - 90^\circ$ , that means from the  $x$ -axis to the  $z$ -axis with a permanent angle  $\varphi = 0^\circ$ . Due to technical limitations, as will be explained later, the setup allows external fields of  $\mu_0 H_x \leq 150$  mT for angles  $\theta = 55^\circ - 90^\circ$ , that means  $0^\circ - 35^\circ$  out-of-plane in respect to the sample surface and  $\mu_0 H_z \leq 70$  mT for angles  $\theta = 0^\circ - 35^\circ$ , which means  $55^\circ - 90^\circ$  out of plane in respect to the sample surface. Thirdly, the easy axis is governed by the demagnetization field and lies in-plane for the small thickness of the samples. Fourthly, the Zeeman energy rotates the magnetization by an angle of at most  $7^\circ$  out of plane [7]. Fifthly, because no significant in plane anisotropies were observed, the magnetization aligns with the  $H_x$ , where it should be stated that  $\mathbf{H}_{ext} = (H_x, H_y, H_z)$ .

With these characteristics, the angle  $\varphi = 0$  and the external field component  $H_y = 0$ , the derivatives of the free energy are

$$\begin{aligned} \left. \frac{\partial^2 F}{\partial \theta^2} \right|_{\varphi=0} &= (-2K_x + 2K_z - \mu_0 M_s^2) \cos 2\theta + \mu_0 M_s (H_x \sin \theta + H_z \cos \theta), \\ \left. \frac{\partial^2 F}{\partial \varphi^2} \right|_{\varphi=0} &= (2K_x - 2K_y) \sin^2 \theta + \mu_0 M_s H_x \sin \theta, \text{ and} \\ \left. \frac{\partial^2 F}{\partial \theta \partial \varphi} \right|_{\substack{\varphi=0 \\ H_y=0}} &= 0. \end{aligned}$$

This indicates that the precession takes place around the equilibrium direction tilted by the angle  $\theta$  out-of-plane and  $\omega$  is

$$\omega = \frac{\gamma}{\mu_0 M_s \sin \theta} \sqrt{\mu_0 M_s (H_x \sin \theta + H_z \cos \theta) + (-2K_x + 2K_z - \mu_0 M_s^2) \cos 2\theta} \cdot \sqrt{\mu_0 M_s H_x \sin \theta + (2K_x - 2K_y) \sin^2 \theta}. \quad (1.63)$$

At this point, the formula can be simplified further. Due to the small rotation, one can assume that  $\theta \approx \frac{\pi}{2}$ . No precession without an external field leaves  $K_x \approx K_y$  and no

significant in-plane anisotropy yields  $K_z \gg K_x$ . Therefore,

$$\omega = \frac{\gamma}{\mu_0} \sqrt{\mu_0 H_x \left( \mu_0 H_x + \mu_0 M_s - \frac{2K_z}{M_s} \right)}. \quad (1.64)$$

The saturation magnetization for the examined materials, namely nickel and permalloy, is  $\mu_0 M_s(\text{Ni}) = 0.659 \text{ T}$  and  $\mu_0 M_s(\text{Py}) = 0.8 \text{ T}$ .

This final expression 1.64 is called the Kittel formula. It describes the frequency dispersion relation of the Kittel precession mode with  $k = 0$ . The precession frequency is measured by applying different external field strengths systematically. Then the Kittel formula can be fitted to the experimentally determined values of  $\omega$  over the different external fields and that way it can be used to determine the out-of-plane anisotropy constant  $K_z \left[ \frac{\text{J}}{\text{m}^3} \right]$ . As it will be presented later, the knowledge of the out-of-plane anisotropy constant is essential to determine the Gilbert damping parameter.

## 1.6 Gilbert Damping in Experiments

In this final section dealing with the theory on magnetization dynamics, the Gilbert damping parameter  $\alpha$  will be derived. This is the proffered parameter used to compare the precession damping from different experimental techniques and specifications. In time resolved experiments, the damping is observed in a form of the exponential decay time  $\tau_\alpha$  of the precession amplitude. The Gilbert damping parameter  $\alpha$  is related to  $\tau_\alpha$  for the Kittel  $k = 0$  mode. In order to derive this relation, we have to go back to the LANDAU-LIFSHITZ-GILBERT equation 1.26:

$$\frac{d\mathbf{M}}{dt} = -\gamma \mathbf{M} \times \mathbf{H}_{eff} + \frac{\alpha}{M_s} \mathbf{M} \times \frac{d\mathbf{M}}{dt}.$$

This equation needs to be linearized for the three components  $M_x, M_y, M_z$  of the magnetization, in order to extract the relevant parts.

$$\begin{pmatrix} \frac{dM_x}{dt} \\ \frac{dM_y}{dt} \\ \frac{dM_z}{dt} \end{pmatrix} = -\gamma \begin{pmatrix} M_y H_{eff,z} - M_z H_{eff,y} \\ M_z H_{eff,x} - M_x H_{eff,z} \\ M_x H_{eff,y} - M_y H_{eff,x} \end{pmatrix} + \frac{\alpha}{M_s} \begin{pmatrix} M_y \frac{dM_z}{dt} - M_z \frac{dM_y}{dt} \\ M_z \frac{dM_x}{dt} - M_x \frac{dM_z}{dt} \\ M_x \frac{dM_y}{dt} - M_y \frac{dM_x}{dt} \end{pmatrix} \quad (1.65)$$

The next step is to take a closer look at the relevant magnetization components which contribute to the precession. There are some properties the examined samples possess. Firstly, we are dealing with thin films therefore the magnetization takes mainly place in-plane which means  $M_z \ll \sqrt{M_x^2 + M_y^2}$ . Also the external field  $\mathbf{H}_{ex}$  is applied in the  $xz$ -plane, therefore  $\mathbf{M}$  is aligned with the  $x$ -direction and the precession proceeds in the  $yz$ -plane. This means  $M_y, M_z \ll M_x \approx 1$ . With these considerations the set of three coupled equations simplifies to two coupled equations

$$\begin{aligned} \dot{M}_y &= -\gamma(M_z H_{eff,x} - M_x H_{eff,z}) - \alpha \dot{M}_z \\ \dot{M}_z &= -\gamma(M_x H_{eff,y} - M_y H_{eff,x}) - \alpha \dot{M}_y \end{aligned} \quad (1.66)$$

For further calculations with this set of equations, explicit knowledge of the effective field  $\mathbf{H}_{eff}$  is required. In the case of the examined samples, again, the expressions obtained for the free energy consists of the Zeeman energy, also including the shape anisotropy and the magneto crystalline anisotropy with its anisotropy parameters for all directions  $K_x, K_y, K_z$  generally present. For simplification the normalized magnetization vector

$$\mathbf{m} = \frac{\mathbf{M}}{M_s} = \begin{pmatrix} m_x \\ m_y \\ m_z \end{pmatrix} = \begin{pmatrix} \sin \theta \cos \varphi \\ \sin \theta \sin \varphi \\ \cos \theta \end{pmatrix} \quad (1.67)$$

in polar coordinates is introduced. With this, the free energy, unchanged from section 1.5.1, reads

$$\begin{aligned} F = & -K_x m_x^2 - K_y m_y^2 - K_z m_z^2 \\ & - \mu_0 M_s (H_x m_x + H_y m_y + H_z m_z) \\ & + \frac{1}{2} \mu_0 M_s^2 m_z^2. \end{aligned} \quad (1.68)$$

From here on, the effective magnetic field is given by the derivative of the free energy derived above. The normalized magnetization vector then becomes

$$\begin{aligned} \mathbf{H}_{eff} = & -\frac{1}{\mu_0 M_s} \frac{\partial F}{\partial \mathbf{m}} \\ = & \begin{pmatrix} H_x + \frac{2K_x}{\mu_0 M_s} m_x \\ H_y + \frac{2K_y}{\mu_0 M_s} m_y \\ H_z + \left( \frac{2K_z}{\mu_0 M_s} - M_s \right) m_z \end{pmatrix}. \end{aligned} \quad (1.69)$$

Now, the components of the effective field can be inserted into the set of coupled equations 1.66, yielding in

$$\begin{aligned} \dot{M}_y = & -\gamma M_s H_z - \gamma \left( H_x + \frac{2K_x}{\mu_0 M_s} - \frac{2K_z}{\mu_0 M_s} + M_s \right) M_z - \alpha \dot{M}_z, \text{ and} \\ \dot{M}_z = & \gamma \left( H_x - \frac{2K_y}{\mu_0 M_s} + \frac{2K_x}{\mu_0 M_s} \right) M_y - \alpha \dot{M}_y. \end{aligned} \quad (1.70)$$

One method of solving this set of equations is by derivation in time as the time derivatives of higher order can be used to replace components in the equations. It is thus possible to uncouple the equations and make them dependent on only one component in a single direction. The time derivatives of equations 1.70 are

$$\begin{aligned} \ddot{M}_y = & -\gamma \left( H_x + \frac{2K_x}{\mu_0 M_s} - \frac{2K_z}{\mu_0 M_s} + M_s \right) \dot{M}_z - \alpha \ddot{M}_z, \text{ and} \\ \ddot{M}_z = & \gamma \left( H_x - \frac{2K_y}{\mu_0 M_s} + \frac{2K_x}{\mu_0 M_s} \right) \dot{M}_y - \alpha \ddot{M}_y. \end{aligned} \quad (1.71)$$

The magnetization vector precesses around the  $x$ -axis, describing a circle in the  $zy$ -plane. This means, both  $M_y(t)$  and  $M_z(t)$  differ in phase, and as will be seen later in the experiment only the projection on the  $y$ -axis of the magnetization is observed. Thus decoupling the expression 1.71 leads to one equation of motion which only depends on  $M_y$  and its time derivatives, but not on  $M_z$ .

$$(1 + \alpha^2)\ddot{M}_y + \alpha\gamma \left( 2H_x + \frac{4K_x}{\mu_0 M_s} - \frac{2K_y}{\mu_0 M_s} \frac{2K_z}{\mu_0 M_s} + M_s \right) \dot{M}_y + \gamma^2 \left( H_x + \frac{2K_x}{\mu_0 M_s} - \frac{2K_z}{\mu_0 M_s} + M_s \right) \left( H_x + \frac{2K_x}{\mu_0 M_s} - \frac{2K_z}{\mu_0 M_s} \right) M_y = 0. \quad (1.72)$$

It looks almost like the equation of motion for a damped harmonic oscillator. Therefore, the usual ansatz can be applied

$$M_y = A_{M_y} \exp(-i\omega t) e^{-t/\tau_\alpha}. \quad (1.73)$$

In this case  $A_{M_y}$  is the precession amplitude,  $\omega$  is the precession frequency and  $\tau_\alpha$  again the characteristic exponential decay time. In order to see a real oscillation the imaginary part of the solution needs to be zero. With the time derivatives of the ansatz

$$\dot{M}_y(t) = \left( -i\omega - \frac{1}{\tau_\alpha} \right) A_{M_y} \exp(-i\omega t) e^{-t/\tau_\alpha} \quad (1.74)$$

$$\ddot{M}_y(t) = \left( \frac{1}{\tau_\alpha^2} - \omega^2 + 2i\omega \frac{1}{\tau_\alpha} \right) A_{M_y} \exp(-i\omega t) e^{-t/\tau_\alpha} \quad (1.75)$$

one obtains for the imaginary part of the equation of motion

$$(\alpha^2 + 1) \frac{2i\omega}{\tau_\alpha} - i\omega\alpha\gamma \left( \underbrace{2H_x + \frac{4K_x}{\mu_0 M_s} - \frac{2K_y}{\mu_0 M_s} - \frac{2K_z}{\mu_0 M_s} + M_s}_{=H'} \right) = 0 \quad (1.76)$$

Where  $H'$  is constant for a given external field. This quadratic equation for  $\alpha$  can be solved as usual and provides

$$\alpha = \frac{1}{2} \left( \frac{\tau_\alpha \gamma H'}{2} \pm \sqrt{\left( \frac{\tau_\alpha \gamma H'}{2} \right)^2 - 4} \right). \quad (1.77)$$

From these two solutions, one can be excluded by physical considerations: The amount of  $\tau_\alpha \gamma H'$  is  $\gg 1$  for the experimental setup. This would lead to over-damping  $\alpha \gg 1$  for the solution with the "+" in front of the square root. However, this is contrary to the observations, there are several oscillations observed, before the precession decays and fades out, as will be seen later. Therefore, the solution carrying the "-" sign is the physically relevant solution.

It can be simplified by expanding the square root by Taylor for small  $x$  with  $\sqrt{1-x} \approx 1 - \frac{1}{2}x + o(x^2)$ . Finally, the damping parameter can be determined from

$$\alpha = \frac{1}{\tau_\alpha \gamma \left( H_x + \frac{2K_x}{\mu_0 M_s} - \frac{K_y}{\mu_0 M_s} - \frac{K_z}{\mu_0 M_s} + \frac{M_s}{2} \right)}. \quad (1.78)$$

As mentioned before, the examined samples do not show any in-plane anisotropy, which justifies the negligence of the constants  $K_x$  and  $K_y$ . The remaining expression can then be simplified to

$$\alpha = \frac{1}{\tau_\alpha \gamma \left( H_x - \frac{K_z}{\mu_0 M_s} + \frac{M_s}{2} \right)}. \quad (1.79)$$

Obviously, the anisotropy constant  $K_z$  is necessary in order to determine the damping parameter  $\alpha$ . Because of this, it is necessary to apply equation 1.64 and fit the precession frequencies, to find out the value of  $K_z$ . Therefore, the frequency spectra for several external magnetic fields for a constant thickness and material selection have to be made. For high external fields, the anisotropy contribution becomes smaller and finally stops playing a role, which simplifies equation 1.79 to

$$\alpha = \frac{1}{\tau_\alpha \omega}. \quad (1.80)$$

Both of these parameters,  $\omega$  and  $\tau_\alpha$  can be obtained by fitting the measured spectra by a suitable function introduced later. So that 1.80 can be used for a rough estimation of  $\alpha$ .



## 2 The Experiments

### 2.1 Experimental Environment

Let us have a closer look at the experimental arrangement and its components. The experiments require stable laser pulses in time.

First a few words should describe the experimental environment shortly. The lab room is air-conditioned and held at a constant temperature, set to  $21^{\circ}\text{C}$  with fluctuations less than  $\pm 1^{\circ}\text{C}$  through the year. The experimental equipment and the experiment itself are situated on an air damped table of high mass to minimize oscillations of the table to about 1 Hz comparable to the oscillations of the building. Above the experimental table a filtered and temperature stabilized air duct delivers air through equally spaced holes equidistantly spread throughout the whole table area. This ensures that the area of the table is free of dust. Furthermore, the experimental table is separated from the lab room by rubber lamellae hanging from the fan of the table edge, thus creating a laminar air flow in the experimental area is created. This reduces turbulences and possible dust particles in the experimental area and, also the disturbance of the laser beam is minimized.

### 2.2 The fs Laser Equipment

The laser system is assembled out of five components as depicted in figure 2.1. It consists of the pump laser (Verdi 18), the Ti:Sapphire oscillator and the amplifier (RegA + Expander, Compressor). Before the required laser pulses arrive at the experiment, the creation of the fs-laser pulses begins with the self built Ti:Sapphire laser oscillator [11, 14]. The Ti:Sapphire crystal is pumped with ca. 5.2 W, at 532 nm. The cavity is built in z-configuration. Two prisms are used for dispersion compensation. Using kerr mode locking allows to generate  $\sim 60$  fs pulses with a repetition rate of 80 MHz and a power of about  $500\text{ mW} \hat{=} 2\text{ }\mu\text{J/pulse}$ . The wavelength spectra width of the coupled generated pulses is  $\sim 700\text{ nm} - 845\text{ nm}$ .

From here the beam is coupled into an expander where the pulses are stretched in time to be coupled to the regenerative amplifier, RegA 9050 (Coherent). Both the Ti:Sapphire and the RegA are optically pumped by a commercial Verdi V18, solid state (Nd : YVO<sub>4</sub>), frequency doubled (532 nm), continuous wave laser. The RegA with about 11.3 W and the Ti:Sapphire crystal with about 5.2 W. In the RegA the pulses are amplified to about  $4.5\text{ }\mu\text{J}$  per pulse and proceed to the Compressor. Here, the pulses are again compressed to a pulse duration of about 60 – 80 fs and loose a little of their energy to  $\sim 4\text{ }\mu\text{J}$ .

Before arriving at the experiment the laser beam carrying the pulses passes an arrangement consisting of a  $\lambda/2$  plate and a polarizer; this allows to adjust the pulse energy proceeding to the experiment in the range from zero up to about  $2.5 \mu\text{J}$  per pulse. As it can be seen in figure 2.1 there are four components. The expander and compressor are situated in the same box.

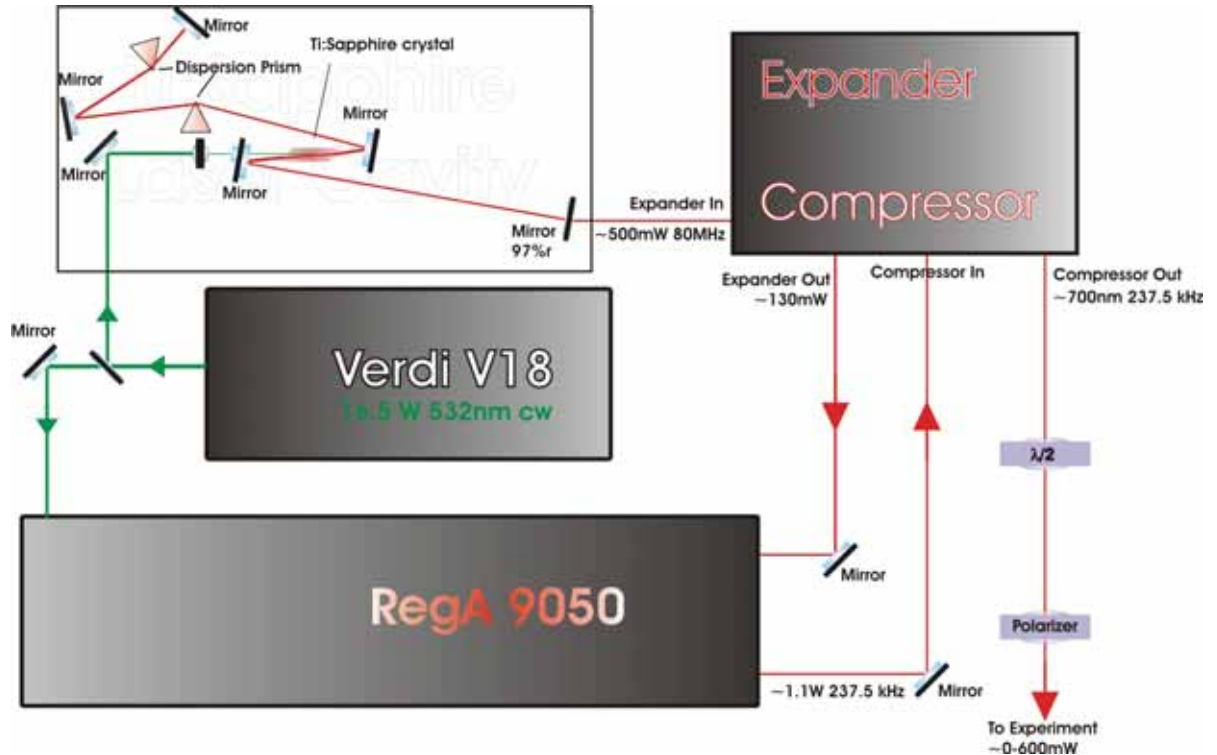


Figure 2.1: Pump laser, master oscillator, amplifier system and the expander/compressor box.

## 2.3 The Experimental Time-resolved MOKE Setup

The time resolved magneto-optical Kerr effect (TRMOKE) experiment is set up as schematically shown in figure 2.2. First, the beam is split into two beams, in a way that one still has about 95% of the energy and is called the pump beam. The other, much weaker beam holding about 5% of the original energy will be referred to as the probe beam.

From here on, the pump beam goes through a mechanical chopper and passes a delay stage. This is a mirror system positioned on a guide rail. By changing the mirror position on the delay stage, the path length for the pulses of the pump beam to the sample can be varied. This way the arrival of the pump pulses in relation to the probe pulses can be varied by the delay time  $\Delta\tau$ . After passing the delay stage the pump beam is directed straightly to the sample and focused to reach it with a spot size of  $\sim 60 \mu\text{m}$ . It arrives at the sample nearly perpendicular to the surface. A small

deviation from perpendicularity is necessary, so that the beam is not reflected back into the beam positioning optics.

The probe beam passes through a polarizer first, followed by a  $\lambda/4$ -plate, before the beam proceeds to the photo elastic modulator. Finally, the probe beam has to be directed to arrive at the sample surface in an angle of  $25^\circ$  to the surface normal and a spot size of  $30\mu\text{m}$ . The reflected beam in the end passes an analyzer, and its intensity is detected by a photo diode and the magneto-optical Kerr rotation  $\theta_k$  can thus be detected. It is proportional to the magnetization  $M$ .

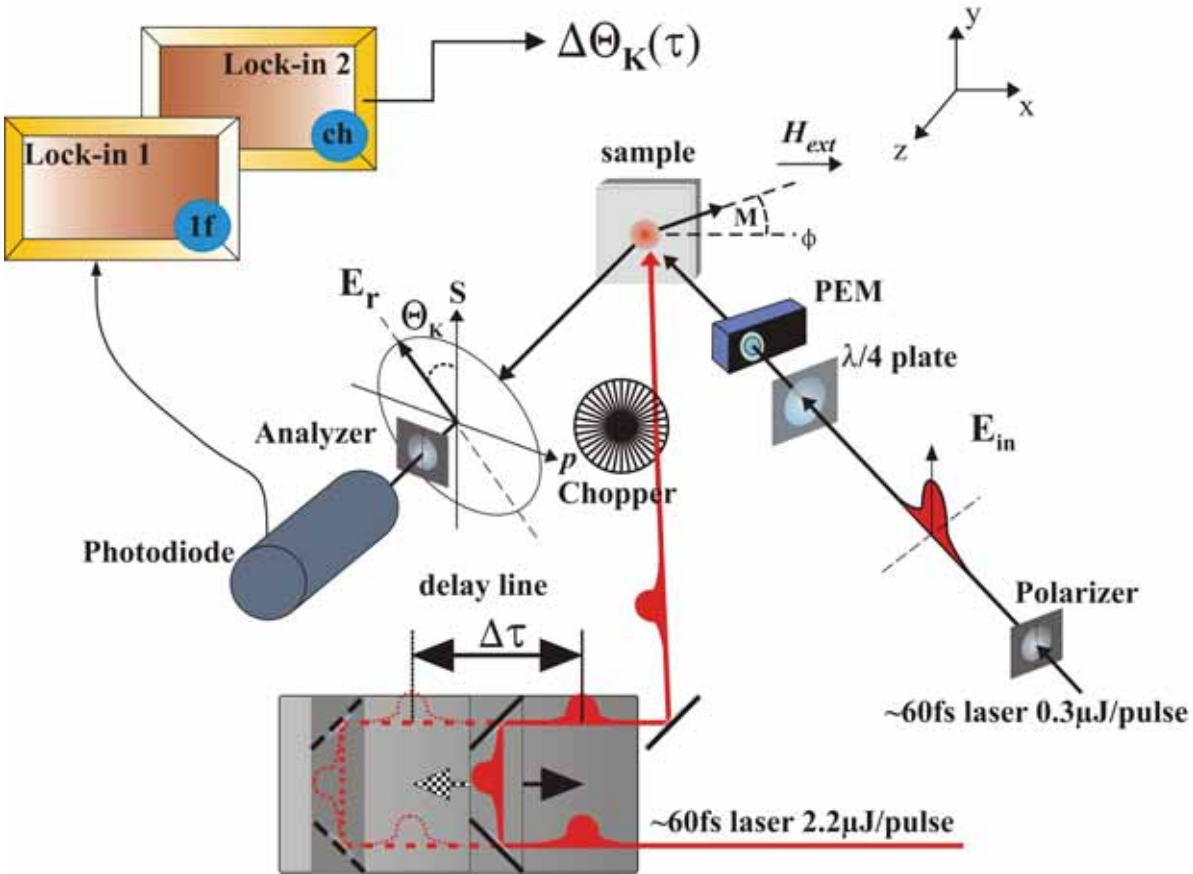


Figure 2.2: Scheme of the experimental setup for the TRMOKE experiments.

Knowing the optical path, the question arises which measurements are possible.

Considering a sample, located in an external field generated by an electromagnet as presented in [7], there are two possibilities to carry out measurements with this arrangement: The simple one is static MOKE. This means recording the Kerr rotation of the sample in respect to the applied field. Using ferromagnetic materials in the experiment yields in a hysteresis. Not all components available at the setup shown in figure 2.2 are needed. Only the first Lock-In amplifier is used to detect the polarization angle  $\theta_K$  of the reflected beam, as will be discussed later. The pump beam is not absolutely necessary for this kind of experiment, but can be used to determine the

hysteresis before and after electron excitation by the pump pulse at a specific delay time, so that the demagnetization rate can be determined.

Apart from this first possibility, also a time resolved kind of measurement is possible. These TRMOKE (Time Resolved Magneto-Optic Kerr effect) experiments, as the name suggests can be used to trace the change of magnetization. Here, the second Lock-In amplifier is used to record the change in the polarization in a specific time interval  $\Delta\theta_K$ . In our experiments, the change in magnetization has been observed, after demagnetizing the sample by the pump beam.

## 2.4 Magneto-Optical Kerr Effect

The change in polarization  $\theta_k$  of the light reflected from a sample is proportional to its magnetization  $M$ . A closer look is needed how both changes, in polarization and magnetization, are connected. First, we will take a look at the possible geometries to measure MOKE. There are three configurations as illustrated in figure 2.3. In the

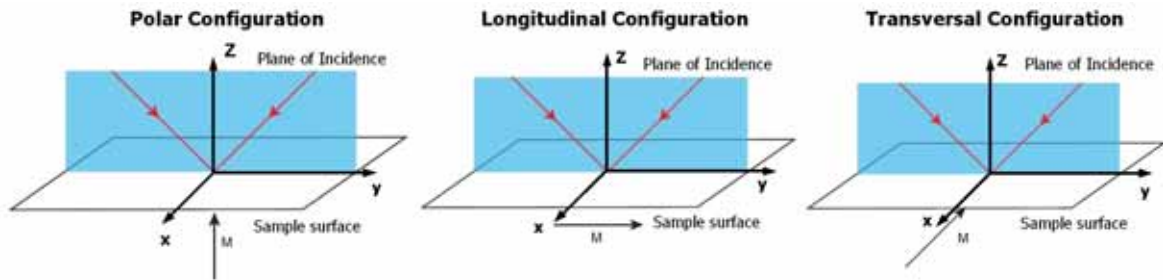


Figure 2.3: Possible MOKE geometries

polar Kerr geometry the magnetization is perpendicular to the sample surface and parallel to the optical plane, the plane formed by the incoming and reflected beam. In the longitudinal Kerr geometry, on the other hand, the magnetization is parallel to both, the sample surface as well as the optical plane. Finally, in the transversal Kerr geometry, the magnetization is parallel to the sample surface, but perpendicular to the optical plane. As described, the applied field  $H$  points in the same direction as the magnetization for every geometry. For one direction of the external field the magnetization aligns with the effective field which changes with the strength of the external field, and can be measured as follows.

In the polar geometry, the magnetization change is proportional to the  $z$ -component of the Kerr rotation and ellipticity respectively, whereas in the longitudinal geometry the change is proportional to the  $y$ -component of the Kerr rotation and ellipticity respectively. The transversal geometry eventually results in a change in reflectivity. In real experiments, the orientation of the external field  $H_{ext}$  is given by the available electro-magnet. Also, due to the high demagnetization fields, the magnetization is not aligned with  $H_{ext}$ . Therefore, the measurement signal is a mixture of polar, longitu-

dinal and eventually transversal Kerr effect. These will be addressed in detail in the following section.

### 2.4.1 Phenomenological Description

For the beginning we will examine the phenomenological description of the Kerr-effect before looking at the microscopic origin. Phenomenologically, we assume that direct interaction of the magnetic field  $\mathbf{H}$  with the magnetization can be neglected for optical frequencies. Therefore, the interaction of the electric field vector  $\mathbf{E}$  of the light with matter can be fully described by the electric polarization vector  $\mathbf{P}$ . For small electric fields the polarization or the dielectric displacement  $\mathbf{D}$  depends linearly on the electric field  $\mathbf{E}$  of the incoming light:

$$\begin{aligned}\mathbf{P} &= \chi\mathbf{E} \\ \mathbf{D} &= \varepsilon\mathbf{E} \\ \varepsilon &= 1 + 4\pi\chi,\end{aligned}$$

where  $\chi$  stands for the electric susceptibility and  $\varepsilon$  represents the dielectric function.  $\varepsilon$  is a symmetric tensor for paramagnets and an antisymmetric tensor for ferromagnets with, the Onsager relation holding for its components:

$$\varepsilon_{ij}(-\mathbf{M}) = \varepsilon_{ji}(\mathbf{M}).$$

The dielectric tensor in the case of non vanishing magnetization can be generally written with the help of Euler's angles as

$$\varepsilon = \varepsilon_{xx} \begin{pmatrix} 1 & -iQm_z & iQm_y \\ iQm_z & 1 & -iQm_x \\ -iQm_y & iQm_x & 1 \end{pmatrix}, \quad (2.1)$$

with  $(m_x, m_y, m_z) = \mathbf{M}/M_s$  and  $Q = i\varepsilon_{xy}/\varepsilon_{xx}$  being the magneto-optical constant. For simplicity  $\varepsilon_{zz} = \varepsilon_{yy} = \varepsilon_{xx}$ . As was done in [29], the magneto-optical Fresnel reflection matrix can be derived by solving the Maxwell equations for the above  $\varepsilon$ ; it is

$$\mathbf{R} = \begin{pmatrix} r_{pp} & r_{ps} \\ r_{sp} & r_{ss} \end{pmatrix} \quad (2.2)$$

with the definitions

$$\theta_K^p = \frac{r_{sp}}{r_{pp}} \quad (2.3)$$

$$\theta_K^s = \frac{r_{ps}}{r_{ss}} \quad (2.4)$$

for the complex Kerr rotation for  $p$ -polarized and  $s$ -polarized light.

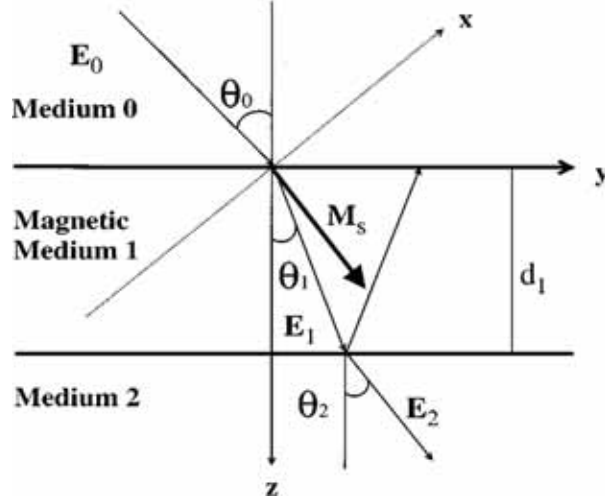


Figure 2.4: Optical path through a thin film medium 1 of thickness  $d_1$  and arbitrary magnetization direction. Taken from [29].

Simplified formulations for both MOKES (polar, longitudinal) are derived in the limit for ultra thin magnetic films. As shown in figure 2.4 the incoming light wave penetrates through a thin film into the substrate. With this approach double reflections have to be introduced into the calculations. In figure 2.4 the scheme of an incoming light wave with the electric vector  $\mathbf{E}_0$  and angle  $\theta_0$  to the surface normal from a medium 0 with a refraction index  $n_0$  into a magnetic medium 1 with a refraction index  $n_1$  and thickness  $d_1$  is shown. The light wave is partly reflected and partly propagates through medium 1 (here indicated with the wave vector  $\mathbf{E}_1$ ) into medium 2, with another refraction angle  $\theta_2$  and is again partly reflected and partly propagating into medium 2. This is the case if when a thin film is deposited on a much thicker substrate, medium 2. With these assumptions the following simplified relations for the complex Kerr angle are valid:

Firstly, for the polar configuration, we can assume that  $m_z = 1$  and  $m_x = m_y = 0$ . Then the Kerr rotation for  $p$ -polarized and  $s$ -polarized light are

$$(\theta_K^p)^{pol.} = \frac{\cos \theta_0}{\cos(\theta_0 + \theta_2)} \cos \theta_2 \Theta_n \quad (2.5)$$

$$(\theta_K^s)^{pol.} = \frac{-\cos \theta_0}{\cos(\theta_0 - \theta_2)} \cos \theta_2 \Theta_n \quad (2.6)$$

with  $\Theta_n$  being the complex polar Kerr effect for normal incidence in the limit for ultra thin films given by

$$\Theta_n = \frac{4\pi n_0 n_1^2 Q d_1}{\lambda(n_2^2 - n_0^2)}. \quad (2.7)$$

Secondly, for the longitudinal configuration, the field components are given by  $m_y =$

1 and  $m_x = m_z = 0$ . Which yields

$$(\theta_K^p)^{long.} = \frac{\cos \theta_0}{\cos(\theta_0 + \theta_2)} \frac{\sin^2 \theta_1}{\sin \theta_2} \Theta_n \quad (2.8)$$

$$(\theta_K^s)^{long.} = \frac{\cos \theta_0}{\cos(\theta_0 - \theta_2)} \frac{\sin^2 \theta_1}{\sin \theta_2} \Theta_n \quad (2.9)$$

Thirdly, the equations for both configurations can be combined in order to obtain the general, geometry independent relations

$$\theta_K^p = \frac{\cos \theta_0}{\cos(\theta_0 + \theta_2)} \left( m_y \frac{\sin^2 \theta_1}{\sin \theta_2} + m_z \cos \theta_2 \right) \Theta_n \quad (2.10)$$

$$\theta_K^s = \frac{\cos \theta_0}{\cos(\theta_0 - \theta_2)} \left( m_y \frac{\sin^2 \theta_1}{\sin \theta_2} - m_z \cos \theta_2 \right) \Theta_n. \quad (2.11)$$

One should note that these simplified analytic formulas have proven to be consistent with experiments carried out on thin films [29].

## 2.4.2 Microscopic Model

After these phenomenological considerations, a quantum mechanical model for the cause of the rotation will be derived. The complex Kerr rotation angle for a thin film of thickness  $D$  is given, if  $D \ll \lambda$ , by

$$\theta_K = \frac{i\sigma_{xy}}{\sigma_{xx}^s} \frac{4\pi D}{\lambda}, \quad (2.12)$$

where  $\sigma_{xy}$  is the complex off-diagonal component of the conductivity tensor,  $\sigma_{xx}^s$  is the optical conductivity of the substrate and  $\lambda = 2\pi c/\omega$  is the wavelength of light in vacuum. According to equation 2.12 a Kerr rotation exists, if the off diagonal matrix elements do not vanish. So let us have a look at the conductivity tensor as has been done in [3]. In terms of microscopic electronic structure the conductivity tensor can be obtained from Fermi's golden rule. Considering optical transitions from an initial state  $|i\rangle$  to the final unoccupied state  $|f\rangle$  the off-diagonal imaginary component  $\sigma_{xy}''$  of the conductivity tensor is

$$\sigma_{xy}'' = \frac{\pi e^2}{4\hbar\omega m^2 \Omega} \sum_{i,f} f(\epsilon_i) [1 - f(\epsilon_f)] \times [|\langle i|p_-|f\rangle|^2 - |\langle i|p_+|f\rangle|^2] \delta(\omega_{fi} - \omega), \quad (2.13)$$

with  $p_{\pm} \equiv p_x \pm p_y$ ,  $f(\epsilon)$  is the Fermi-Dirac function,  $\Omega$  the total volume and  $\hbar\omega_{f,i} \equiv \epsilon_f - \epsilon_i$  is the energy difference between the states. The factor  $\delta(\omega_{fi} - \omega)$  ensures the energy conservation condition and the matrix elements  $\langle i|p_-|f\rangle$  and  $\langle i|p_+|f\rangle$  express the dipolar transitions for left and right polarized light. Thus,  $\sigma_{xy}''$  depends

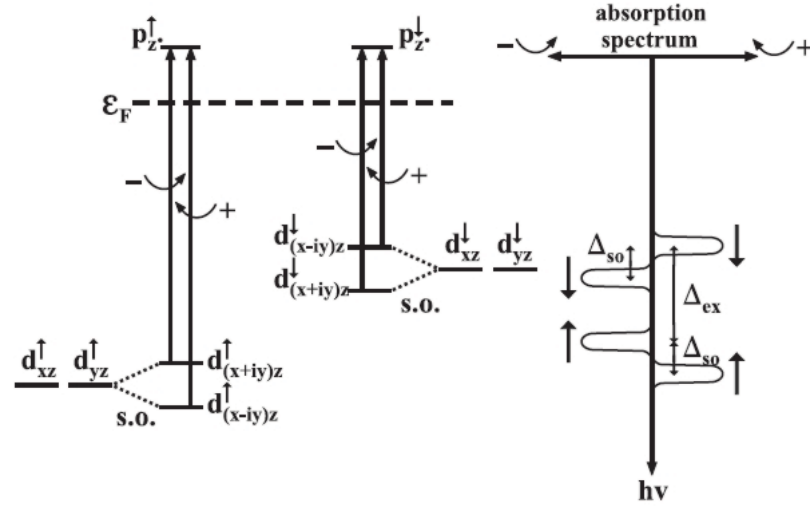


Figure 2.5: Transitions from  $d$  to  $p$  levels in transition metals (left) and the corresponding absorption spectra for photon energies  $h\nu$  (right). Taken from [3].

linearly on the absorption difference for both polarization directions. With the given selection rules for electronic dipolar transitions

$$\begin{aligned}\Delta l &= \pm 1 \\ \Delta m_l &= \pm 1,\end{aligned}$$

in transition metals only transitions between  $d$  and  $p$  levels are allowed. Further, the second rule confines the transitions to correspond to left ( $\Delta m_l = +1$ ) or right ( $\Delta m_l = -1$ ) polarized light. As illustrated in figure 2.5 in transition metals the transition takes place from the  $d_{xz,yz}$  levels with  $l = 2$  and  $m_l = \pm 1$  to  $p_z$  levels with  $l = 1$  and  $m_l = 0$ . The exchange energy  $\Delta_{ex}$  causes a partition between the spin up and spin down levels. Spin-orbit coupling  $\Delta_{so}$  splits the levels into  $d_{(x+iy)z}$  with  $m_l = +1$  and  $d_{(x-iy)z}$  with  $m_l = -1$ . Both sorts of spins are split differently. While for spin up,  $m_l = +1$  is the higher energy level, the reverse is valid for spin down. This shows that in a transition ferromagnet the Kerr rotation is caused by the simultaneous appearance of exchange splitting and spin-orbit splitting.

## 2.5 The Measurement Technique

For a better understanding of the carried out experiments a short introduction into the applied measurement technique is necessary. First, the detection of the Kerr effect by employing a Photo-Elastic Modulator (PEM), and second, the expansion to time resolved measurements applying the double-modulation technique is presented. The used experimental setup is identical with the one used in [7], and here the techniques will be just outlined shortly.

### 2.5.1 Detection of the Kerr Rotation

In our experimental setup the Kerr effect is detected making use of a polarisation modulation technique, by use of an active optical element, the PEM. As depicted in figure 2.2 linearly polarized light passes through a  $\lambda/4$ -plate, then the resulting circularly right polarized light is modulated by the PEM. The modulation is represented by the Jones matrix:

$$\mathbf{M}_{\text{PEM}} = \begin{pmatrix} e^{iA \sin \omega t} & 0 \\ 0 & 1 \end{pmatrix},$$

where  $\omega/2\pi = 50 \text{ kHz} = \nu_1$  is the modulation frequency of the PEM, which is passed on to the Lock-in and  $A = \pi/2$  is the maximum phase shift. The sample is located in an external magnetic field of an electro magnet as described previously. The reflected light passes through an analyzer to be detected by a photo diode. The measured signal  $I$  consists of a  $DC$  and an  $AC$  part. The Kerr angle  $\theta_K$  is then measured through an intensity change  $I$  by the Lock-In amplifier as follows

$$\begin{aligned} I_{DC} &= \frac{R}{2} \\ I_{\nu_1} &= J_1\left(\frac{\pi}{2}\right) R (\alpha_A - \theta_K) \\ I_{2\nu_1} &= -2J_2\left(\frac{\pi}{2}\right) R \varepsilon_K. \end{aligned}$$

The  $DC$  signal  $I_{DC}$  gives the reflectivity  $R$ . Locking the signal  $I_{\nu_1}$  at the modulation frequency  $\nu_1$  gives a change in the Kerr angle in respect to the analyzer angle  $\alpha_A$ . Locking the signal  $I_{2\nu_1}$  at the double modulation frequency  $2\nu_1$ , the ellipticity  $\varepsilon_K$  is detected.

### 2.5.2 The Time Resolved Kerr Effect

In order to extract the timed resolved Kerr effect from the measurement a double modulation technique is needed. Whereas the Kerr rotation is extracted with the probe beam in the same way as in the previous section. To obtain the change in the Kerr rotation  $\Delta\theta_K$  the pump beam intensity is modulated by a mechanic chopper at a frequency of  $\nu_2 = 800 \text{ Hz}$ , as depicted in figure 2.2. The signal obtained by the first Lock-In  $L_1$  is passed to a second Lock-In  $L_2$  locking the signal at the frequency  $\nu_2$ . The time constants ( $\tau(L_1) = 10 \mu\text{s}$ ,  $\tau(L_2) = 300 \text{ ms}$ ) and the sensitivities ( $V_{max}(L_1) = 20 \text{ mV}$ ,  $V_{max}(L_2) = 100 \text{ mV}$ ) of the Lock-In's are set to gain the maximum magnetic signal.

## 2.6 The Thermal Effect of the Pump Pulse

There is still one thing missing for a complete experiment description: The answer to this question is, what happens inside of the sample, after a pump pulse has arrived

and how this influences the magnetization within the sample on the ps time scale. Before the pump pulse arrives, the electrons of the sample are at the temperature

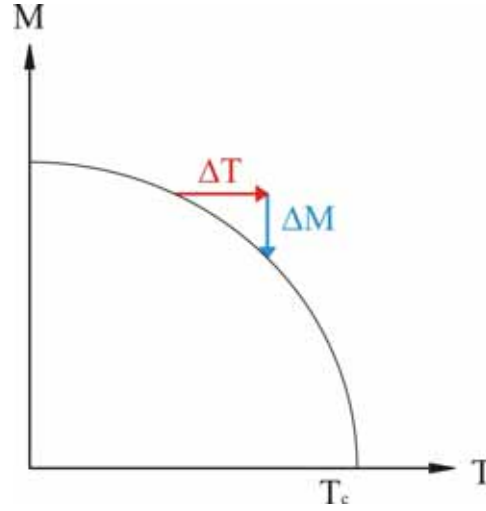


Figure 2.6: Demagnetization by increase of temperature.

$T$  distributed according to the Fermi-Dirac statistics. The energy deposited by the laser pulse causes a population inversion of the electrons above the Fermi level by optical transitions. The electrons thermalize through electron-electron scattering to a Fermi-Dirac distribution at a higher temperature  $T + \Delta T$ . After this the energy is transferred to the lattice (electron-phonon scattering) and to the spin system (electron-spin scattering). The spin scattering leads to a rise in temperature of the spin system and so the loss of ferromagnetic order as can be concluded from figure 2.6 (Curie-Weiss-Law).

The time evolution of this scattering process is described by the three temperature model [13]. The temperatures  $T_e$ ,  $T_p$ ,  $T_s$  are coupled by the coupling constants  $g_{ep}$ ,  $g_{es}$ ,  $g_{sp}$  where the subscripts are  $e$  for electron,  $p$  for phonon and  $s$  for spin. With the heat capacities  $C_e$ ,  $C_p$ ,  $C_s$  the dependencies of the three temperature model are

$$\begin{aligned} C_e(T_e) \frac{dT_e}{dt} &= -g_{ep}(T_e - T_p) - g_{es}(T_e - T_s) + P(t) \\ C_s(T_s) \frac{dT_s}{dt} &= -g_{es}(T_s - T_e) - g_{sp}(T_s - T_p) \\ C_p(T_p) \frac{dT_p}{dt} &= -g_{ep}(T_p - T_e) - g_{sp}(T_s - T_p). \end{aligned}$$

where  $P(t)$  represents the laser field pulse energy.

### 2.6.1 Laser-Induced Magnetization Dynamics

Apart from the demagnetization, the excitation of the spin system has another effect triggering the precession of the spins. This effect is most clearly explained with the

help of figure 2.7. First, before the pump pulse arrives, the system is in equilibrium, i.e. the magnetization is aligned with the effective field  $\mathbf{H}_{eff}$ . The occurrence at the point in time when the pump pulse arrives is considered as the excitation by the pulse. The energy deposited by the pump pulse increases the temperature of the sample within the laser spot. The anisotropy changes due to the temperature increase, which leads to a change in the effective field. This process takes place on a timescale smaller than 1 ps. After the anisotropy has changed, the effective field the magnetization  $\mathbf{M}$  begins to align with  $\mathbf{H}_{eff}$  starting to precess around it. Meanwhile, the sample cools down to the equilibrium temperature and the anisotropy returns to its original value with the effect that  $\mathbf{M}$  is out of equilibrium at this time ( $< 10$  ps after excitation). The change in anisotropy field pulse resulting from the change in temperatures triggers the precession. This can be implemented into the LLG 1.26 as follows:

$$\dot{\mathbf{M}} = -\gamma \mathbf{M} \times (\mathbf{H}_{eff} + \mathbf{H}_{pulse}(t)) + \frac{\alpha}{M_s} \mathbf{M} \times \dot{\mathbf{M}}. \quad (2.14)$$

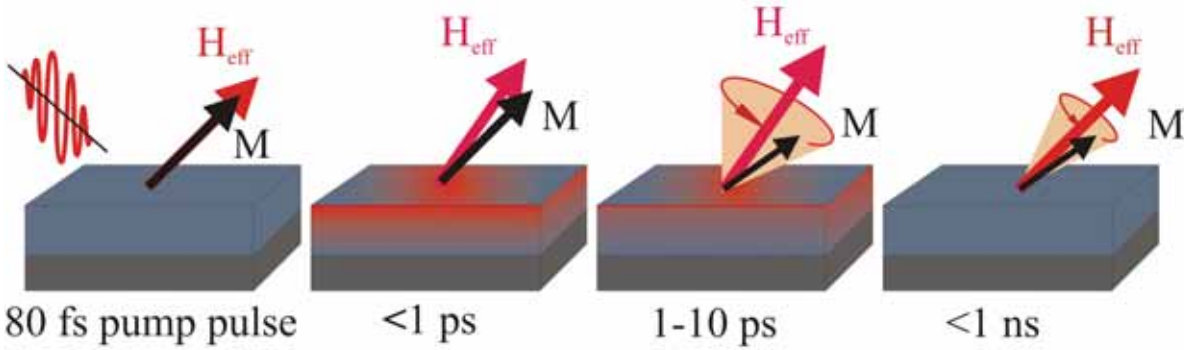


Figure 2.7: Laser-Induced magnetization dynamics within the first ns.

Finally, the magnetization has to align with the effective field which is back in the equilibrium position again. This alignment process is a precession of the magnetization in the effective field. The process starts around 30 ps after the excitation and takes place on a timescale up to a few ns. In order to describe the precession of the magnetization aligning back with the effective field in equilibrium again the LLG equation without the anisotropy field pulse is used.

Additionally, in the case of samples thinner than the laser pulse penetration depth all spins are excited and precess in phase. In this case, the macro spin approximation is valid for the analysis and only the Kittel  $k = 0$  mode is present. This justifies an analysis using a damped sine-like precession. For this case, the analysis of the data is easier than for the occurrence of several precession modes, because the precession frequency and declination time can be obtained by fitting the function introduced in the next chapter. The latter case requires the application of fourier transforms in order to extract the involved precession frequencies.



## 3 Sample Preparation and Positioning

Two kinds of ferromagnetic materials, namely nickel and permalloy ( $\text{Ni}_{80}\text{Fe}_{20}$ ), are subject to this thesis, the former of which were self-prepared by vapor deposition in the UHV-laboratory. The latter were prepared by Mathias Kläui using MBE.

### 3.1 UHV Vapor Deposition

The UHV chamber can reach base pressures of  $p < 5 \cdot 10^{-10}$  mbar; it was built at the University of Göttingen (for a detailed description see [8]). The deposition process takes place as follows. The deposited materials are heated by an electron beam coming from an e-gun in order to be evaporated and deposited on a Si 100 substrate. The thickness is controlled with an oscillating crystal, obtaining an accuracy  $< 1 \text{ \AA}$ . This accuracy is achieved by the positioning of the oscillating crystal. It is positioned closer to the evaporated material than the substrate on which the material is deposited.

Before the deposition the substrates are cleaned in an ultrasonic bath in the first step with acetone, following a cleaning with propanol for about four minutes each.

### 3.2 Wedge Preparation

The primal approach was to determine the intrinsic damping of pure nickel. In order to do this, a pure nickel wedge of 15 mm length with a slope of 3 nm/mm as depicted in 3.1 was prepared. This reference wedge was prepared in order to determine the

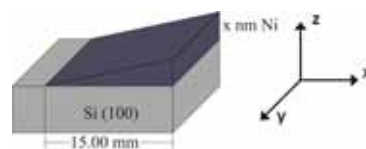


Figure 3.1: Schematic illustration of the nickel reference sample ( $\text{Si}/x \text{ nm Ni}$ ).

damping parameter  $\alpha$  in dependence of the thickness of pure nickel.

Because the damping depends on the thickness of the ferromagnetic and the non-magnetic damping material, wedge samples of both, nickel and vanadium were grown. In this way, more flexibility in the choice of the desired thickness is given and the growth conditions are kept constant for every thickness, making this method preferable to preparing several samples of different thicknesses. The dimensions of the wedges and the other layers of the sample can be seen in figure 3.2.

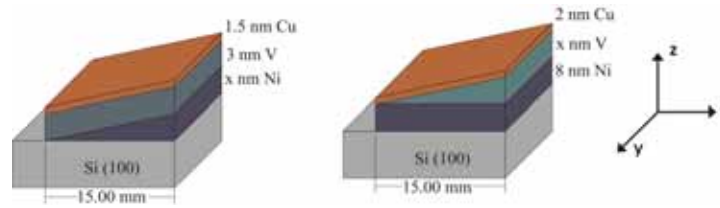


Figure 3.2: Schematic depictions of the prepared nickel vanadium samples. The Si/ $x$  nm Ni/3 nm V/1.5 nm Cu sample left and the Si/8 nm Ni/ $x$  nm V/2 nm Cu right.

The wedges were built-up as follows:

Technically, there is a shutter positioned directly below the substrate that can be moved between the substrate surface and the deposition source. This way the deposition can be stopped, as soon as the required thickness is obtained. The motor which moves the shutter is synchronized with the oscillating crystal. After the desired thickness of the deposited layer is achieved, the shutter is closed systematically according to the aimed slope of the wedge.

The length of the deposited wedges is usually 15 mm. For a wedge with a slope of 3 nm/mm, the thickness is varied from 0 – 45 nm. In figure 3.2 left is a nickel wedge on silicon, on top of it is a constant vanadium layer of 3 nm deposited. Further the vanadium layer is covered with a 1.5 nm copper layer in order to prevent the sample surface from oxidation. On the right side of figure 3.2 the opposite sample wedge is prepared, this time a constant nickel layer is covered with a vanadium wedge. The copper layer is again deposited to avoid oxidation of the vanadium. All materials are deposited with a deposition rate of 0.4 – 0.5 Å/s to maintain comparability. Within the spot size of 60  $\mu$ m the thickness of the wedges changes by  $\sim 0.2$  nm which can be neglected and the thickness in this area can be considered as constant.

### 3.3 Alloyed Permalloy Samples

In addition to the non-local Gilbert damping on Nickel thin films also another damping mechanism on permalloy thin films were studied. The permalloy samples are doped locally with the damping material. In order to do this, permalloy samples alloyed with up to 2% Dysprosium and 1% Palladium were prepared. The preparation took place in a UHV at a base pressure of  $10^{-10}$  mbar. The preparation technique is MBE. The substrate is held at room temperature and a growth rate of about 0.03 Å/s is applied. This assures a uniform distribution of the doping material throughout the sample thickness and the required ratio between nickel (80%) and iron (20%). As an oxidation protection, the samples were finally capped with gold at room temperature. The doping is estimated from the evaporation rates.

### 3.4 Positioning of the Wedge Samples in the Experimental Setup

In order to probe a wedge sample at a defined thickness, the sample needs to be placed in the external magnetic field in a way, that the laser spot strikes it at a defined wedge position. For this purpose, the sample holder is installed on top of a micrometer stage and the sample can be moved relative to the probe laser spot. The stage can be moved in  $x$ -direction according to figures 2.2, 3.1 and 3.2. Moving the micrometer stage using a stepper motor with a resulting resolution of  $3 \mu\text{m}/\text{step}$ , controlled by a computer program, allows to record a reflection profile of the wedge. In figure 3.3, a profile of a nickel wedge on a silicon substrate is depicted as an example.

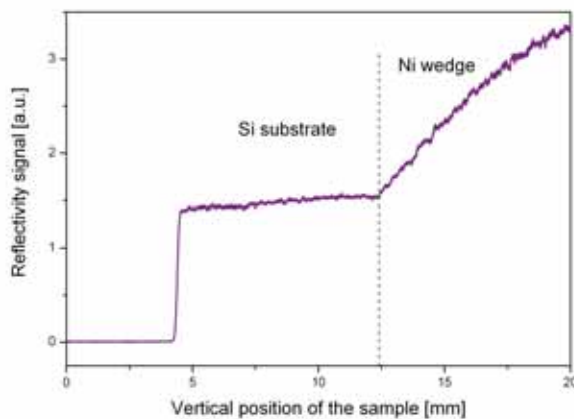


Figure 3.3: Reflection measurement along the wedge profile.

For the first 5 mm, the sample is not situated within the measurement arrangement, so that the laser spot does not strike it and the reflected signal is zero. At 5 mm the signal suddenly increases and stays constant for about 7.5 mm. This is the point at which the edge of the silicon substrate is moved in front of the laser spot. The reflected signal remains constant, because there is no material deposited on the substrate, until it reaches the nickel wedge. At the position, at which the nickel layer starts, also the reflected signal begins to increase linearly with the nickel layer thickness. When the wedge thickness reaches the penetration depth of light, which is around 15 nm in nickel for a wave length of 800 nm, the reflected signal stops increasing linearly and reaches its saturation point, although the thickness continues to grow. Due to experimental limitations, a reflectivity scan can only be recorded for 20 mm; therefore, only a part of the nickel wedge has been recorded (up to a thickness of 37.8 nm). This can be seen from the reflection profile, as the increase in the reflected signal is not linear for the whole wedge; in the end it bends down. However, knowing the starting position of the wedge, and the slope of the increasing thickness of the nickel layer, it is easy to set the sample to a defined thickness and measure magnetization dynamics.



## 4 The Experimental Results

### 4.1 Analysis of the Experimental Data

Before discussing the experimental results and the different damping mechanisms, the concept of how the relevant parameters are obtained from the measured spectra shall be given briefly. The measured quantity is the transient Kerr rotation  $\Delta\theta_k(\Delta\tau)$ , this means the change in magnetization depending on the delay time between the pump and probe pulse. The time scale is chosen in a way that for  $\Delta\tau < 0$  the system is in equilibrium, in this case long enough after excitation, thus the magnetization is aligned with the effective field  $\mathbf{H}_{eff}$  again. By fitting the measured spectrum with

$$\Delta\theta_k = \exp\left(-\frac{\Delta\tau}{\tau_\alpha}\right) \cdot \sin(2\pi(\Delta\tau - \tau_0)\nu) + B, \quad (4.1)$$

two parameters can be obtained, namely the precession frequency  $\nu$  and the exponential decay time  $\tau_\alpha$ , where  $\tau_0$  is a phase shift for the sine function. The additional constant  $B$  takes care of the reflectivity contribution to the measurement signal, arising from phonon excitations and non coherent magnetic excitations. This part of the function represents the background of the measured spectra which is simply subtracted and not further analyzed in this thesis. The function is fitted from 30 ps to 1 ns after excitation, this means after the easy axis returned back to its original position and the precession takes place around  $\mathbf{H}_{eff}$ . Knowing the precession frequency and the decay time for various external fields  $\mathbf{H}_{ext}$  further calculations can be made. First, the Kittel formula can be applied to fit the precession frequencies for the various external fields for obtaining the anisotropy constant  $K_z$ . Generally, the frequency will be given instead of the angular frequency. Equation 1.64 in section 1.5.1 can be modified to obtain  $\nu(H_{ext})$ , thus yielding

$$\nu = \frac{g\mu_B}{\hbar 2\pi} \sqrt{\mu_0 H_{ext} \cos \phi \left( \mu_0 H_{ext} \cos \phi + \mu_0 M_s - \frac{2K_z}{M_s} \right)}. \quad (4.2)$$

Here,  $g$  is the gyromagnetic factor being  $g_{Ni} = 2.21$  for nickel and  $g_{Py} = 2.12$  for permalloy. The angle  $\phi$  is the angle between the direction of the external field  $\mathbf{H}_{ext}$  and the easy magnetization axis of the sample,  $H_{ext}$  is the magnitude of the external field. The saturation magnetization corresponds to 0.659 T for nickel and 0.8 T for permalloy. The last term of the square root denotes the anisotropy field  $H_{ani}$ , by  $\frac{2K_z}{M_s} = H_{ani}$ .

In our experiments, the measurements were carried out for external fields  $H_{ext} \leq 150$  mT in 10 mT steps. The anisotropy constant  $K_z$  is obtained by fitting the extracted precession frequencies, to the squareroot function in equation 4.2. Knowing

the anisotropy constant, further calculations concerning the damping factor  $\alpha$  were made using a modified for the experimental setup equation 1.79 from section 1.6:

$$\alpha = \frac{1}{\tau_{\alpha}\gamma \left( \cos \phi H_{ext} - \frac{K_z}{\mu_0 M_s} + \frac{M_s}{2} \right)}. \quad (4.3)$$

This way the damping in respect of the strength of the external field can be determined. The measurements done on the samples with a varying thickness (wedge), allowed to determine the damping parameter in respect of the nickel layer thickness.

## 4.2 The Damping Mechanisms

For the discussion of the results, the knowledge of different damping mechanisms is necessary. The modeling of the damping parameter is still a challenging task to theorists, because even for magnetization precession without damping there are no constants of motion. The ability to control the damping will allow the fabrication of materials with specific magneto-dynamic properties, needed for memory devices. Besides this, it will also help to increase the speed of magnetic memory devices.

### 4.2.1 Damping Processes

Magnetic damping can be introduced by introducing an energy dissipation process. In the following I will adopt the concept given in the lecture by M. Fähnle [9, 7]. The equation of motion 1.26 is obeyed by the magnetization vector in the energy dissipation process. However, it is only suitable for one dynamic variable, while all other degrees of freedom have to be integrated out. In general, the equation of motion is non-local in time, which means, the considered dynamic variable transfers energy and momentum to the eliminated degrees of freedom.

There are two possibilities for energy dissipation by which damping is classified: The first is indirect damping, where the energy is transferred from the dynamical variable considered to other magnetic degrees of freedom. Energy transfer to the fast magnetic degrees of freedom, for example, the damping by Stoner excitations, that are single spin-flip processes.

The second way is called direct damping. Here, the energy is transferred to nonmagnetic degrees of freedom. This is usually the case when energy is dissipated to the lattice. Here, again, two cases can be distinguished which originate from spin-orbit coupling. On one hand, there is the intrinsic type of magnons scattering on phonons. This is an unavoidable, material specific occurrence which can not be influenced by any means. On the other hand, there is the extrinsic type of direct damping. This damping is on account of magnon scattering on phonons, caused by defects and interfaces. Extrinsic damping can be influenced by the growth parameters or the doping with impurities. Therefore, one way to engineer the damping is the manipulation of

defects. It will be introduced by means of permalloy samples alloyed with low concentration impurities.

In addition to the local dissipation processes, non-local damping on interfaces with ferro- or non-magnetic layers and the considered ferromagnetic layer occur. The emission of spin waves or spin currents on the ferromagnet-ferromagnet interface or the ferromagnet-non-magnet interface provide additional damping. This additional non-local damping depends on the kind and the geometry of the adjacent material, as will be seen from the measured nickel wedge double layer samples.

### 4.2.2 Theoretical Models for Damping

For the qualitative discussion of various direct damping mechanisms, the loss of energy by electromagnetic radiation or via dipolar interactions between nuclei and electrons can be neglected for the slow degrees of freedom. In this case, direct damping is caused by spin-orbit coupling. The corresponding theory can be divided into two classes:

The first class of theory is founded on the direct transfer from the slow degrees of freedom to the lattice. This happens mainly by magnon-phonon scattering. The spin-orbit coupling is included in a phenomenologic way by coupling the magnetization  $M(\mathbf{r}, t)$  to the elastic lattice strain  $\epsilon(\mathbf{r}, t)$ . The damping is then mainly generated by magnon-phonon scattering and the scattering of phonons at lattice defects.

The second class of theory is constructed on the basis of energy transfer from magnons via the electrons to the lattice. This happens as follows: the electrons absorb the moments of the slow degrees of freedom, and later pass these moments to the lattice via electronic scattering. There are three possibilities to transfer the energy from spins to electrons. First, there is the transfer by spin-current interactions, considered as damping by Eddy currents. Second, there is the transfer by Coulomb interaction, which is called the BREATHING FERMI SURFACE MODEL. The third possibility is the magnon-electron interaction, known as the s-d damping model.

Electronic scattering can be divided into different types. First it should be stated, that there are no pure spin-up and spin down states. Spin-orbit coupling leads to small spin mixing, as a result the spin-up and spin-down states are not perfectly orthogonal to each other. Under these circumstances, the scattering potentials have a non-vanishing amplitude at inhomogeneities, e.g. phonons or defects.

There are four sorts of scattering processes which contribute differently to the damping process. They are sorted by the conservation of spin and the corresponding energy band as follows:

ordinary scattering: The transitions take exclusively place between states of same spin, but different bands. There is no spin-flip. Momentum transfer is rather small.

spin-flip scattering: In this transition the spin of the initial state differs from the spin of the final state. The transfer of magnetic momentum is significant. Yet this effect is strongly reduced in ferromagnets by the molecular field .

intraband scattering: This scattering describes transition within one energy band. It is the dominating process for small relaxation times  $\tau$ . This leads to a damping parameter proportional to the conductivity  $\sigma$ .  $\Rightarrow \alpha \sim \sigma \sim \tau$ .

interband scattering: This type of scattering appears between states in different energy bands. It is the leading process for large relaxation times and proportional to the resistivity  $\rho$ .  $\Rightarrow \alpha \sim \rho \sim 1/\tau$ .

The first class of damping theory described previously is based on direct transfer of magnetic energy to the lattice. The newest approaches to model damping theoretically pertain to the second class of theory mentioned above. Namely the s-d current model and the Breathing Fermi surface model are based on the electronic scattering on phonons. Both models assume the near-adiabatic regime, which makes them only useful for long relaxation times and this way valid for slow degrees of freedom. These two models will now be discussed briefly.

#### s-d Current Model

The s-d model based on [30, 10] can be found in [9, 7] described in detail. The idea behind this model is, that both the delocalized s and p conduction electrons ( $\mathbf{m}(\mathbf{r}, t)$ ) near the Fermi surface and the localized d electrons far below the Fermi surface ( $\mathbf{M}_d(\mathbf{r}, t)$ ) contribute to the magnetization. The former are responsible for the spin-dependent transport, the latter for the magnetization dynamics. The orbital moments are neglected. The damping goes on the account of the scattering of the conduction electrons. The total magnetization  $\mathbf{M}(\mathbf{r}, t)$  then reads:

$$\mathbf{M}(\mathbf{r}, t) = \mathbf{M}_d(\mathbf{r}, t) + \mathbf{m}(\mathbf{r}, t). \quad (4.4)$$

This leaves to two possibilities for the dynamics, as clarified in figure 4.1. The first is  $\mathbf{M}_d(\mathbf{r}, t)$  and  $\mathbf{m}(\mathbf{r}, t)$  precessing in phase due to the s-d exchange interaction. In this case there is no spin flip scattering ( $\tau_{sf} \rightarrow \infty$ ). The second possibility is a phase shifted precession of the conduction electron magnetization around the localized d electron magnetization. This means in particular that a number of conduction electrons  $\delta\mathbf{m}$  is oriented perpendicular to the d electrons magnetization. This precession around the d electron magnetization generates a torque which is perpendicular to the precession direction of the d electron magnetization, turning the conduction electron magnetization in the direction of the d electrons. This additional torque increases the damping which is growing with the number of spin-flips.

The Landau-Lifshitz-Gilbert equation for the d moments then becomes

$$\dot{\mathbf{M}}_d = -\gamma (\mathbf{M}_d \times \mathbf{H}_{eff,d}) + \frac{1}{M_d} \mathbf{M}_d \times \alpha \dot{\mathbf{M}}_d + \mathbf{T}. \quad (4.5)$$

The first term on the right hand side is the precession of the d electrons influenced by the effective field. The second term stands for the damping of the d electrons. The third represents the additional torque from the scattering of the conduction electrons.

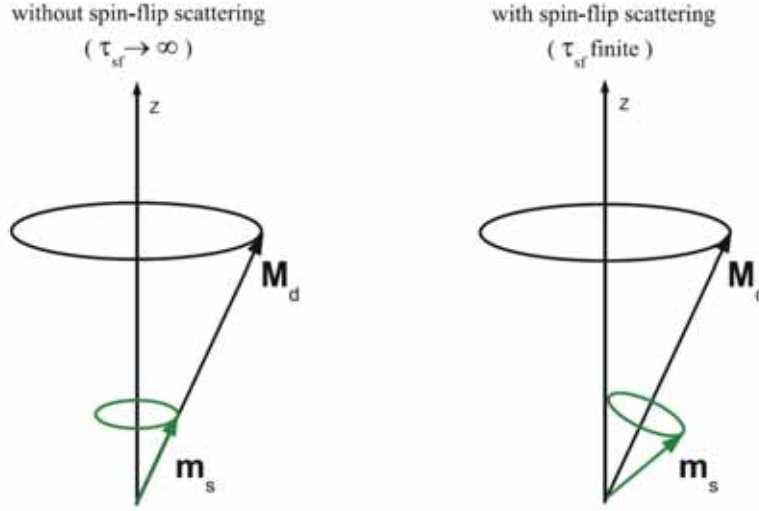


Figure 4.1: Magnetization orientations of the s and d electrons with spin-flip scattering (right) and without spin-flip scattering (left).

Considering the form of the additional torque and connecting it with the conduction electron magnetization through the continuity equation the Gilbert equation can be simplified to a form for the "effective" damping  $\alpha'$ . This is the damping without spin-flip scattering  $\alpha$  plus the damping originating from the spin-flip scattering  $\Delta\alpha$  ( $\alpha' = \alpha + \Delta\alpha$ ). The Gilbert equation is then:

$$\dot{\mathbf{M}}_d = -\gamma(\mathbf{M}_d \times \mathbf{H}_{eff,d}) + \frac{1}{M_d} \mathbf{M}_d \times \alpha' \dot{\mathbf{M}}_d. \quad (4.6)$$

This formulation of the "effective" damping parameter  $\alpha'$  gives a rise to regimes, in which the damping can be calculated in respect of the spin-flip scattering time  $\tau_{sf}$ . For small  $\tau_{sf}$  we have a direct proportionality of  $\Delta\alpha$  and obtain:

$$\tau_{sf} \rightarrow 0 \text{ and } \tau_{sf} < \tau_{ex} \Rightarrow \alpha' = \alpha + \frac{\tau_{sf}}{\tau_{ex}} \cdot \frac{m_s^0}{M_d},$$

with  $\tau_{ex}$  being the precession period of the conducting electrons around the d electrons and  $m_s^0$  representing the adiabatic part of the induced magnetization in the conduction electrons,  $\mathbf{m}_s$ .

For bigger  $\tau_{sf}$  the damping becomes overcritical and  $\alpha'$  is inversely proportional to the spin-flip scattering time. We obtain the relation:

$$\tau_{sf} \rightarrow \infty \text{ and } \tau_{sf} > \tau_{ex} \Rightarrow \alpha' = \alpha + \left(2\alpha + \frac{m_s^0}{M_d}\right) \cdot \frac{\tau_{ex}}{\tau_{sf}}$$

The following conclusions can be made for this model. First, high spin-flip rates ( $\tau_{ex} \gg \tau_{sf}, \alpha \propto \tau_{sf}$ ) imply fast transfer of angular momentum to the lattice. Further, for a growing  $\tau_{sf}$  the energy dissipation is faster and the damping parameter larger. Second,

for low spin-flip rates ( $\tau_{ex} \ll \tau_{sf}$ ), the damping originates from the same mechanism as described by Tserkovnyak et al. [26], damping by spin currents.

In the case of monotone scaling of the spin-flip time with the temperature, the damping parameter depends as follows on  $\tau_{sf}$ . On one hand, at low temperatures, this leads to small spin-flip times,  $\alpha$  is proportional to the conductivity  $\sigma$ . On the other hand, at high temperatures and longer spin-flip relaxation times, the damping becomes proportional to the resistivity  $\rho$ . The experimental confirmation of the concept that both the resistivity and the conductivity contribute to the damping considering the temperature dependence has been provided especially for nickel in FMR experiments. Furthermore, this model underestimates the contribution of the d electrons to the damping and predicts a smaller Gilbert damping parameter than found out in experiments.

Conclusively we can state that the s-d model is applicable to describe current transport in metals. It is also applied to describe damping in 3d systems with 4f impurities. For transition metals however the scattering of the d electrons has to be taken into account. This is the case in the Breathing Fermi Surface Model, which will be sketched in the following section.

#### The Breathing Fermi Surface Model

This model is introduced in detail in [7], so that we can restrict ourselves to discuss its outcome. In the Breathing Fermi Surface Model, the conduction s and p electrons as well as the d electrons are considered delocalized. The Fermi surface is determined by the dipolar, the Zeeman and the spin-orbit interaction energies in an external magnetic field. During the magnetization precession the direction of the magnetization changes or in other words the propagation of spin waves causes a deformation of the Fermi surface. After the deformation, the electrons near the Fermi surface, try to occupy the new states within the Fermi sea. This energy redistribution of energy, caused by electron scattering, delivers the damping parameter. The spin energy dissipation in this model is included phenomenologically by electron relaxation times, rather than microscopically.

The *ab-initio* density-functional theory using the single-electron functions to describe electron scattering, introduced by Fähnle and coworkers [23, 9] is an improvement of the original Breathing Fermi surface model developed in the 1970's.

In order to describe magnetization, the effective single-particle theory uses a wave function  $\Psi_{j,\mathbf{k}}$  for every electron in a band with the band index  $j$  and the wave vector  $\mathbf{k}$ . The orbital momenta are considered to be quenched to a high extend by molecular fields. The magnetization is then given by the sum of all spin components. The band structure energy is then calculated as the sum of the single electron energies  $\epsilon_{j\mathbf{k}}$ , according to the density functional electron theory. Further, using the strictly adiabatic approximation, the resulting time dependent wave function is a solution to the time independent wave equation for the effective potential, which depends on the momentary directions of the atomic magnetic moments  $\{\mathbf{e}_i(t)\}$ . This makes also the single electron energies dependent on the orientation of the atomic magnetic moments. Altogether, small changes in  $\{\mathbf{e}_i(t)\}$  cause modifications in the Fermi surface, hence the

name Breathing Fermi surface.

With approximations to a slightly non-adiabatic situation, the outcome is a direction dependent Gilbert damping parameter, represented by a matrix  $\alpha$ , which replaces the scalar damping parameter  $\alpha$  in the Gilbert equation:

$$\dot{\mathbf{M}} = -\gamma \mathbf{M} \times \mathbf{H}_{ani} + \frac{1}{M} \mathbf{M} \times \left( \boldsymbol{\alpha} \cdot \frac{d\mathbf{M}}{dt} \right) \quad (4.7)$$

with the anisotropy field  $\mathbf{H}_{ani}$  being responsible for the precession and the second term representing the damping part of the effective field.

This dependence of the damping on the direction of the magnetization turns out to be significant by a factor of 4 already for bulk materials in transition metal ferromagnets and even larger in systems with reduced symmetry like monolayers or wires. These latter systems have directions for which the damping is zero. This model provides an additional option to control the switching processes in structured materials, but has not been experimentally verified up to now.

The simple relation between the anisotropy energy and the damping parameter, the larger the damping, the larger the anisotropy, does not hold for the Breathing Fermi surface model.

Finally the limit of the Breathing Fermi surface model has to be discussed. The scattering process in this model includes only electrons near the Fermi surface, this allows only intraband scattering to contribute to the damping. The demagnetization process on the femtosecond time scale is dominated by relaxing electrons, excited by a laser pulse, into higher energy bands. Therefore, this near adiabatic model cannot be applied for this ultrafast processes, yet the processes in the sub ns regime investigated in below are well described by this model.

### 4.2.3 Non-local damping

This last section on damping mechanisms will deal with the non-local damping, investigated on the nickel vanadium samples. Generally, the damping parameter increases, when a normal metal layer is attached to the ferromagnetic layer. In principle, the non-local damping works as follows: spin currents are emitted by the magnetization torque to the interface of the ferromagnet with the normal metal layer. This way angular momentum is transferred to the normal metal layer, which affects the damping. The affection of damping is explained with the help of transport theory in multilayers as introduced in [26, 25, 27]. The approach to non-local damping will be introduced according to the description in [7]. Starting with a trilayer as in figure 4.2, where the ferromagnetic layer is enclosed by two normal metal layers. The additional damping, which adds up to the intrinsic damping, is due to spin dependent scattering at the interface between the normal metal layers and the ferromagnetic layer. This process is known as a spin pumping from the ferromagnetic to the normal metal layer and depends on the characteristics of the materials, as well the ferromagnetic  $F$ , as the normal metal layer  $N$ .

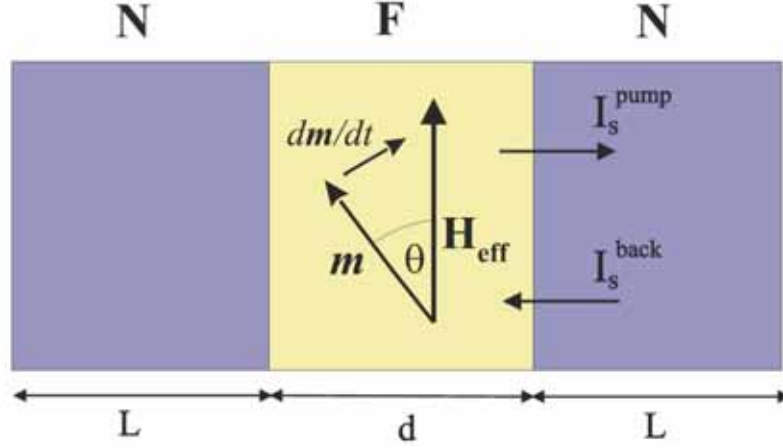


Figure 4.2: Model of non-local damping for a ferromagnetic layer F of thickness  $d$  between two normal metal layers N of thickness  $L$  in an effective field  $\mathbf{H}_{eff}$  (N/F/N). The precessing magnetization in the ferromagnetic layer is  $\mathbf{m}$ .

As a start, we want to implement the non-local damping as additional damping to the intrinsic damping. The origin is the Landau-Lifshitz-Gilbert equation for the magnetic unit vector  $\mathbf{m} = \mathbf{M}/M_s$  without non-local damping processes:

$$\dot{\mathbf{m}} = -\gamma \mathbf{m} \times \mathbf{H}_{eff} + \alpha_0 \mathbf{m} \times \dot{\mathbf{m}}, \quad (4.8)$$

with the effective field  $\mathbf{H}_{eff}$  derived from the free energy, like above, and  $\alpha_0$  the intrinsic damping constant. Taking the denotation from figure 4.2, the ferromagnetic layer F has the thickness  $d$  and the normal metal layers N, each the thickness  $L$  and the angle  $\theta$  between magnetization  $\mathbf{m}$  and the effective field  $\mathbf{H}_{eff}$ . The energy change caused by the scattering at the interfaces between ferromagnet and the normal metal N/F depends on the thickness  $L$  and the angle  $\theta$  is

$$E(L, \theta) = \frac{1}{2\pi i} \int_{-\infty}^{\epsilon_F} \epsilon \frac{\partial}{\partial \epsilon} \ln \det \mathbf{s}(L, \theta, \epsilon) d\epsilon,$$

where  $\mathbf{s}$  is the scattering matrix of the three layers. Bearing this in mind, what does spin transfer between the ferromagnet and the normal metal look like?

A torque  $\tau$ , which is the derivative of the energy change over the precession angle, is responsible for the energy transfer:

$$\tau = \frac{\partial E}{\partial \theta}.$$

According to the conservation of momentum law,  $\tau$  needs to be equal with the spin injection current  $\mathbf{I}_s$ , which is implemented into the Gilbert equation as an additional term:

$$\dot{\mathbf{m}} = -\gamma \mathbf{m} \times \mathbf{H}_{eff} + \alpha_0 \mathbf{m} \times \dot{\mathbf{m}} + \frac{\gamma}{M_s V} \mathbf{I}_s \quad (4.9)$$

The spin current is normalized to the volume  $V$  and the saturation magnetization  $M_s$  of the ferromagnet. The emission of spin currents is triggered by the precession of the magnetization. The net current  $\mathbf{I}_s$  consists of the DC spin current  $\mathbf{I}_s^0$ , the pump current  $\mathbf{I}_s^{pump}$  of spins pumped out of the ferromagnetic layer to the normal metal layer, and the spin current coming back from the normal metal layer  $\mathbf{I}_0^{back}$ :

$$\mathbf{I}_s = \mathbf{I}_s^0 + \mathbf{I}_s^{pump} + \mathbf{I}_0^{back}. \quad (4.10)$$

Without any bias voltage applied, the DC current is negligible. Therefore the net current consists out of the pump current out of the ferromagnetic layer and the current coming back to the ferromagnetic layer. These last two currents appear only when the magnetization direction changes.

When the magnetization starts precessing, e.g. after it has been brought out of equilibrium by an intensive laser pulse,  $\mathbf{I}_s^{pump}$  flows out of the ferromagnet. The spin current into a normal metal layer

$$\mathbf{I}_s^{pump} = \frac{\hbar}{4\pi} \left( A_r \mathbf{m} \times \frac{d\mathbf{m}}{dt} - A_i \frac{d\mathbf{m}}{dt} \right), \quad (4.11)$$

depends on the complex spin pumping coefficient  $A \equiv A_r + iA_i$ .  $A = g^{\uparrow\downarrow} - t^{\uparrow\downarrow}$  in turn depends on the scattering matrix  $s$ , since

$$g^{\sigma\sigma'} \equiv \sum_{mn} [\delta_{mn} - r_{mn}^\sigma (r_{mn}^{\sigma'})^*] \quad (4.12)$$

and

$$t^{\uparrow\downarrow} \equiv \sum_{mn} t_{mn}' (t_{mn}^{\downarrow\uparrow})^* \quad (4.13)$$

are the dimensionless conductance parameters consisting out of reflection coefficients  $r_{mn}^\uparrow (r_{mn}^\downarrow)$  for spin-up (spin-down) electrons on the normal metal layer and the transition coefficients  $t_{mn}' (t_{mn}^{\downarrow\uparrow})$  for the transmitted spin-up (spin-down) electrons through the ferromagnetic layer. The subscripts  $m$  and  $n$  label the incoming and outgoing states at Fermi energy in the normal metal layer. These coefficients are the matrix elements of the reflection and transition matrices  $r (r')$  and  $t (t')$  for the right (left) normal metal layer, which build up the scattering matrix:

$$s = \begin{pmatrix} r & t' \\ t & r' \end{pmatrix}.$$

For ferromagnetic films, thicker than their transverse spin-coherence length  $\lambda_{sc}$ ,

$$d > \lambda_{sc} = \pi / (k_F^\uparrow - k_F^\downarrow),$$

where  $k_F^{\uparrow(\downarrow)}$  are the spin-dependent Fermi wave vectors,  $t^{\uparrow\downarrow}$  can be neglected. For transition metals  $\lambda_{sc}$  is in the range of the lattice constant, a few Å, so that the interface F-N spin pumping is determined entirely by the DC conductance  $A = g^{\uparrow\downarrow} \equiv g_r^{\uparrow\downarrow} + i g_i^{\uparrow\downarrow}$ .

In addition to that, the imaginary part of  $g^{\uparrow\downarrow}$  is much smaller, than the real part. For F-N interfaces, this means, that the spin pumping coefficient can be approximated by  $A \approx g^{\uparrow\downarrow} \approx g_r^{\uparrow\downarrow}$ . For further simplification only one of the two interfaces will be considered.

There are two possibilities for spins pumped to the N-F interface. They can either accumulate at the interface or relax through spin-flip scattering. The spin current returning back into the ferromagnetic layer depends on the accumulation at the interface, which is material specific for the normal metal layer. It is given by:

$$\mathbf{I}_s^{back} = \beta g_r^{\uparrow\downarrow} \mathbf{I}_s. \quad (4.14)$$

As can be seen from the equation above, the returning current is governed by the "back flow" factor  $\beta$ ,

$$\beta \equiv \frac{\tau_{sf} \delta_{sd} / \hbar}{\tanh(L / \lambda_{sd})}. \quad (4.15)$$

The "back flow" factor depends on  $\tau_{sf}$ , the spin-flip relaxation time,  $\lambda_{sd}$  the spin-flip diffusion length and  $\delta_{sd}$  denoting the effective energy-level splitting of the states participating in the spin-flip scattering process.

With these findings for the spin current  $\mathbf{I}_s$ , the equation of motion 4.9 can be written in terms of the intrinsic damping  $\alpha_0$  plus the non-local damping  $\Delta\alpha$  from the injected current:

$$\dot{\mathbf{m}} = -\gamma [\mathbf{m} \times \mathbf{H}_{eff}] + (\alpha_0 + \Delta\alpha) [\mathbf{m} \times \dot{\mathbf{m}}] \quad (4.16)$$

with

$$\Delta\alpha = \frac{\gamma \hbar}{4\pi M_s V} \frac{g_r^{\uparrow\downarrow}}{1 + \beta g_r^{\uparrow\downarrow}}. \quad (4.17)$$

$\Delta\alpha$  is directly dependent on the mixing interface conductance  $g_r^{\uparrow\downarrow}$  and originates from energy dissipation due to non-local damping processes at the N-F interface.

To conclude, we have a non-local damping, which strength is defined by  $g_r^{\uparrow\downarrow}$  and the factor  $\beta$ . The largest damping is achieved, when there is no spin current returning back to the ferromagnetic layer, i.e. when  $\beta \rightarrow 0$ . Otherwise, when there is a significant returning current  $\mathbf{I}_s^{back}$ ,  $\Delta\alpha$  decreases. This is the case, when  $\beta \gg 1/g_r^{\uparrow\downarrow}$ . Then the spin current pumped into the normal metal layer is entirely returned back into the ferromagnetic layer.

For most metals with low impurities, the factor  $\beta$  depends on the number of transverse channels  $N_{ch}$  and the spin-flip probability at each scattering  $\epsilon$  and reads:

$$\beta = \left( 2\pi N_{ch} \sqrt{\frac{\epsilon}{3}} \tanh(L / \lambda_{sd}) \right)^{-1}. \quad (4.18)$$

In the first approximation,  $N_{ch} \approx g_r^{\uparrow\downarrow}$ , the damping parameter  $\Delta\alpha$  can be given by

$$\Delta\alpha = \frac{\gamma \hbar}{4\pi M_s V} g_r^{\uparrow\downarrow} \left( 1 + \frac{1}{2\pi \sqrt{\frac{\epsilon}{3}} \tanh(L / \lambda_{sd})} \right)^{-1} \quad (4.19)$$

At this point we see that the highest  $\Delta\alpha$  is found for a high spin-flip probability  $\epsilon$  and a layer thickness  $L$  of at least double the spin-diffusion length  $\lambda_{sd}$ . With a high enough spin-flip relaxation rate, the spin accumulation at the interface with the normal metal layer is overcome. The spin-flip relaxation time  $\tau_{sf}$  can be roughly estimated using the atomic number  $Z$ . The relation

$$\frac{1}{\tau_{sf}} \propto Z^4 \quad (4.20)$$

says, that heavier metals,  $Z \geq 50$  and p or d conduction electrons come up with a spin-flip probability of  $\epsilon \geq 10^{-1}$ , which makes them ideal spin sinks. Lighter metals however with  $Z \leq 50$ , and s conduction electrons the spin-flip probability drops to  $\epsilon \leq 10^{-2}$ , which makes them not effective as spin sinks. Therefore, vanadium, with  $Z = 23$ , is expected to be an ineffective damping material. By increasing the thickness  $L$  of the normal metal layer, the spin accumulation at the interface F-N can be reduced, but only to a certain extent, due to the saturating behavior of the  $\tanh(x)$  function for  $x > 3$ , this way a limit is set in the rising of  $\Delta\alpha$ . Therefore, increasing the vanadium thickness should not increase damping significantly.

Equation 4.19 suggests that the ferromagnetic layer needs to have a small volume  $V = d \cdot S$ , in order to gain additional damping from spin current emission. However, the entire cross section of the interface between the ferromagnetic and the normal metal layer is used to pump the spin current through. Therefore, this quality is not variable and the damping cannot depend on it. For that reason, the spin pumping coefficient  $A$  is to be replaced by a conductance parameter  $G$  normalized to the cross section  $S$ :

$$G^{\uparrow\downarrow} = \frac{A^{\uparrow\downarrow}}{S} [\Omega^{-1}\text{m}^{-2}]$$

This leads to an effective damping parameter  $\alpha$  for an ideal spin sink:

$$\alpha = \alpha_0 + \Delta\alpha = \alpha_0 + \frac{\gamma\hbar}{4\pi M_s d} G_r^{\uparrow\downarrow}, \quad (4.21)$$

which suggests that non-local additional damping  $\Delta\alpha$  is higher in thinner ferromagnetic layers.

### 4.3 Results for the Non-Local Gilbert Damping Experiments

To characterize the damping properties of nickel, we first determined the intrinsic damping parameter for pure nickel thin films at thicknesses 1 nm to 50 nm as a reference. Later on, in order to analyze the non-local Gilbert damping in the case of a light material, a vanadium layer on top of the nickel layer was studied. The results are presented in the following two sections.

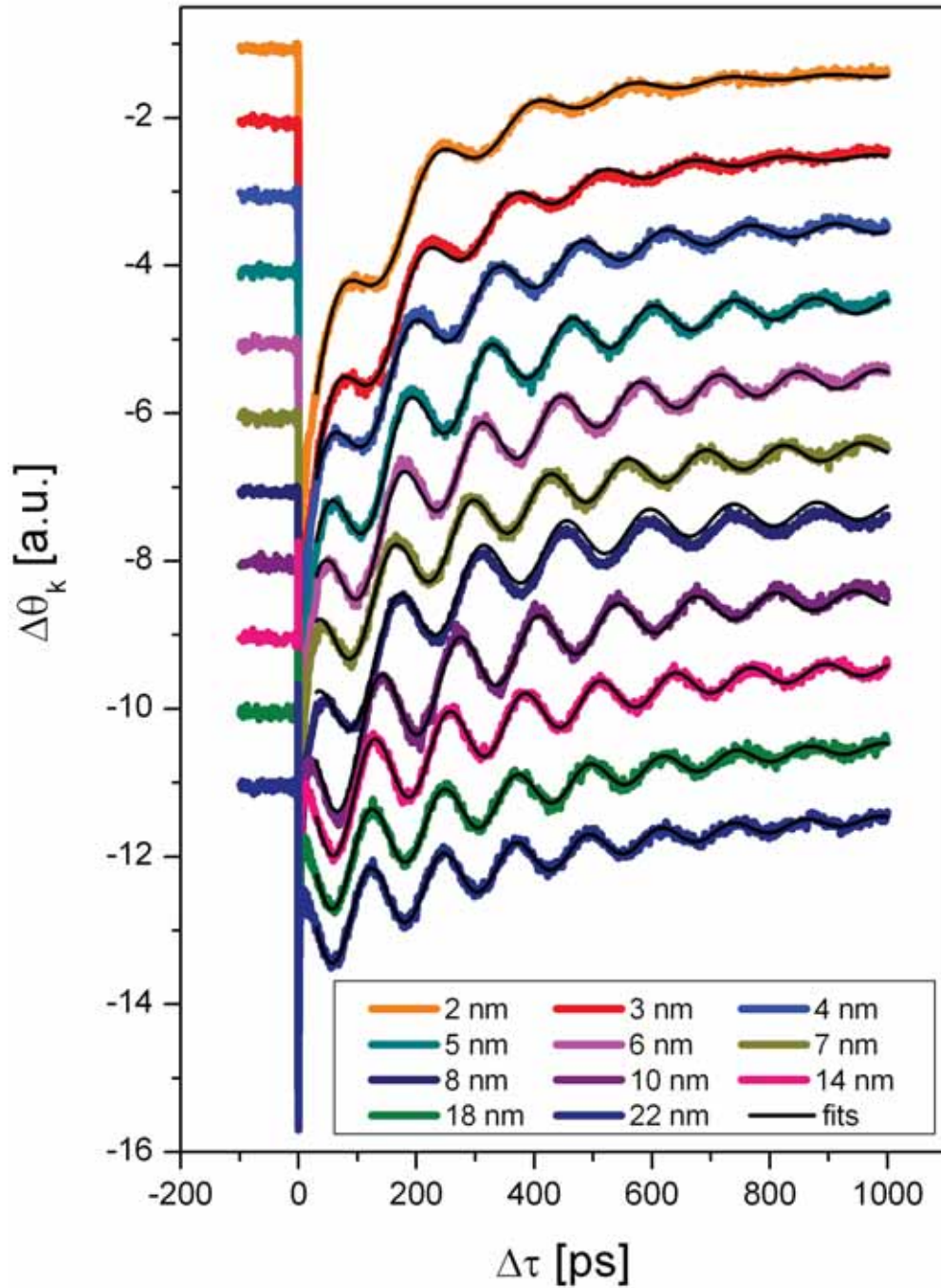


Figure 4.3: Spectra measured for the nickel reference wedge Si/ $x$  nm Ni at 150 mT external field oriented  $30^\circ$  out of plane. For nickel thicknesses  $2 \text{ nm} \leq x \leq 22 \text{ nm}$  and their fits.

### 4.3.1 The Intrinsic Damping of Nickel

To analyze the intrinsic damping properties of a nickel film a Si/ $x$  nm Ni/7 nm Cu sample was studied initially, where  $1 \text{ nm} \leq x \leq 50 \text{ nm}$ . The 7 nm copper layer served as a protection in order to prevent the nickel wedge from oxidation. Initially, copper was chosen, because it is a bad spin sink and does not influence the damping significantly. However, the evaluation, which will not be introduced any further within this thesis, shows that for nickel thicknesses below 10 nm the damping parameter increases by 300%. The increase shows also larger for smaller external fields (90 mT) than for bigger fields (150 mT).

In order to exclude any influence of the copper layer on the increase of the damping parameter for thicknesses below 10 nm, a nickel wedge without a protection layer was prepared. Details of the wedge dimensions are given in section 3.2. This wedge Si/ $x$  nm Ni, was only measured up to thicknesses of 22 nm, because the damping remained constant for thicker layers. Most important was to find out why the intrinsic damping increases for thin nickel layers.

The experiment was repeated with the Si/ $x$  nm Ni sample. Precession spectra for external fields of 90 mT, 120 mT and 150 mT oriented  $30^\circ$  out-of-plane to the sample surface. The spectra presented as an example in figure 4.3 were recorded in an external field of 150 mT. There it can be seen that the precession frequency hardly changes for nickel thicknesses above 10 nm, but decreases for nickel thicknesses below 10 nm. The decrease of the precession frequency indicates an increase in the out of plane anisotropy constant  $K_z$  and therefore the anisotropy field  $H_{ani}$ . Further treatment of the data proves this interpretation. The extracted precession frequencies  $\nu$  show an almost constant precession frequency for nickel thicknesses above 10 nm and a drop in frequency for thicknesses below 10 nm by a factor of two, as can be seen in figure 4.4 left. The same behavior is observed for different external fields. Further, the anisotropy field  $H_{ani}$  increases for nickel thicknesses below 10 nm, while it stays constant for thicknesses above, as can be seen in figure 4.4 right. The errors, of 1 nm for the thicknesses above 10 nm, are due to switching off the laser between measurements. The spectra for thicknesses from 1 nm to 8 nm were recorded on one day. The thicker layers were measured on the following day. Switching off the laser between measurements caused a laser spot displacement of altogether 0.5 mm at the sample surface, which gives a inaccuracy of 1 nm in thickness. This means that the distance between the data points measured later is indicated correctly, but the whole set of points might have to be shifted by about 1 nm.

The final result, the damping parameter  $\alpha$  calculated according to section 4.1 and plotted in respect of the thickness for different magnetic fields, is shown in figure 4.5. It shows that the damping parameter  $\alpha$  stays constant between 0.035 and 0.045, when the nickel thickness is above 10 nm for all applied fields. However, when the nickel layer becomes thinner than 10 nm, the value of the damping parameter  $\alpha$  rises up to 0.1 for 150 mT, and even up to 0.15 for a weaker external field of 90 mT. Although the Ni film is saturated for all field values.

The second set of measurements, on the Si/ $x$  nm Ni sample without a protection

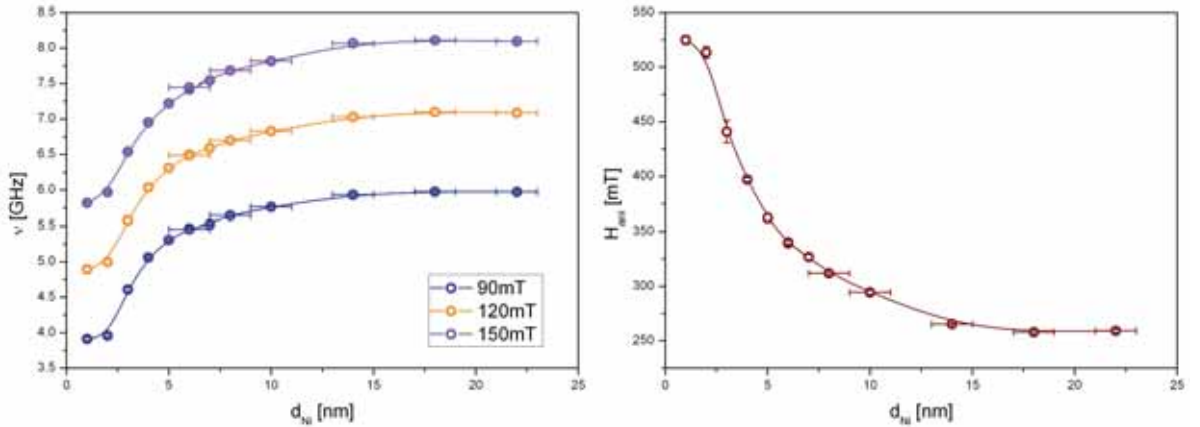


Figure 4.4: Precession frequencies for different external fields, left and the anisotropy field  $H_{ani}$  deduced from the Kittel fit, plotted as a function of the nickel thickness from 1 nm – 22 nm, for the Si/ $x$  nm Ni sample.

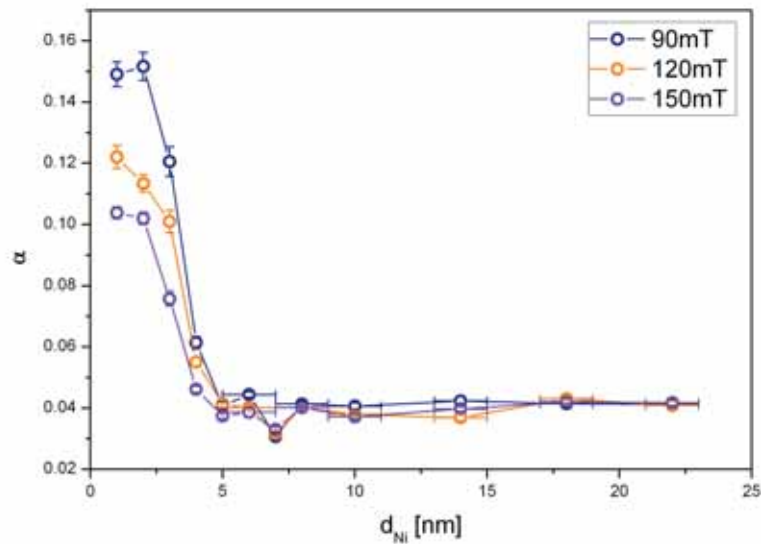


Figure 4.5: The damping parameter  $\alpha$  in respect of the nickel film thickness for the Si/ $x$  nm Ni sample, plotted for different external magnetic fields oriented  $30^\circ$  out-of-plane.

layer, presented above, excludes any non-local damping from the copper layer. The question arising at this point is the reason, why the damping increases for nickel layer thinner than 10 nm and, secondly, why this effect is smaller for larger external fields, while the damping does not depend on the external field for nickel thicknesses above 10 nm.

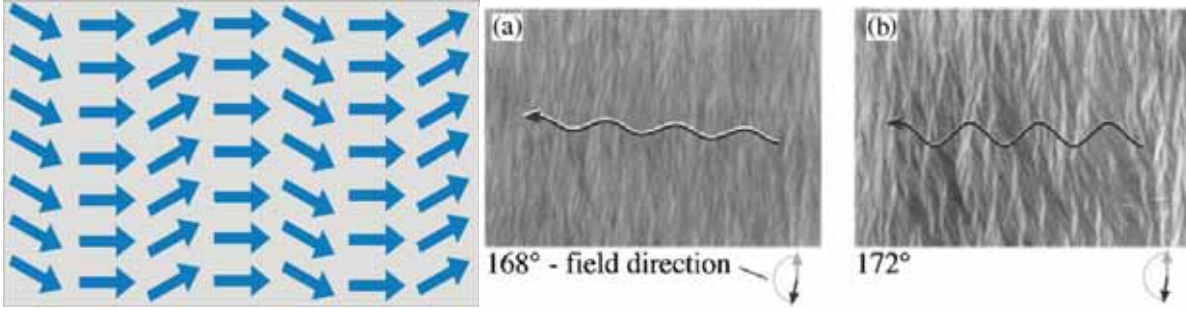


Figure 4.6: The ripple effect. Spins are not aligned parallel anymore, the directions are slightly tilted. A schematic drawing (left). Kerr images of magnetization processes in a field rotated by  $168^\circ$  and  $172^\circ$  from the easy axis in a  $\text{Ni}_{81}\text{Fe}_{19}(10\text{ nm})/\text{Fe}_{50}\text{Mn}_{50}(10\text{ nm})$  bilayer (right), taken from [5].

One possible answer to the first question is the magnetic ripple effect described in [18]. In that case the ripple effect holds as an explanation for the broadening of the FMR line width on a FeTiN sample. The name for this effect arises from a ripple-like alignment of the spins, as indicated in figure 4.6 which shows a schematic depiction on the left and Kerr microscopy recordings of a  $\text{Ni}_{81}\text{Fe}_{19}(10\text{ nm})/\text{Fe}_{50}\text{Mn}_{50}(10\text{ nm})$  bilayer in a rotated magnetic field. The directions vary from position to position through the film in a ripple-like manner. The origin of this tilting angle is a locally changing easy axis that deviates from the macroscopic magnetization direction. Within the slightly tilted directions, the magnetization precesses with slightly different frequencies. This leads to a broadening of the line width in FMR experiments. In the case of all-optical pump-probe experiments an area of  $30\ \mu\text{m}$  is probed at once and a superposition of all the spin precessions within this area is recorded as the oscillating magnetization. Thus the recorded  $\Delta\theta_k$  can not be described by equation 4.1. The involvement of several different frequencies into the precessions examined within the laser spot size, leads to recording rather a superposition of spectra, than a single one. This superposition of precessions is described for the case of a 7% deviation from the central frequency by:

$$\Delta\theta_k \sim \exp\left(-\frac{\Delta\tau}{\tau_\alpha}\right) \cdot \frac{1}{15} \sum_{i=-7}^7 \sin\left(2\pi(\Delta\tau - \tau_0) \cdot \left(1 + \frac{i}{100}\right) \cdot \nu\right). \quad (4.22)$$

The  $i$ 's indicate the variation from the central frequency involved.

We have started to test our model on the 10 nm nickel layer, whose  $\alpha(H_{ext})$  dependency could be explained within the macro spin model, because the damping parameter does not differ from the damping parameters for the thicker layers,  $\alpha_{d_{\text{Ni}}=10\text{ nm}} = \alpha_{d_{\text{Ni}}>10\text{ nm}} = 0.043$  and also  $\alpha_{d=10\text{ nm}}(H_{ext}) = \text{const.}$  is obeyed for the applied external magnetic fields. The fitting parameters  $\tau_\alpha$  and  $\nu$  from the spectra are taken as input for equation 4.22 to simulate the ripple effect. The aim was to find out whether there is a significant effect on the damping parameter, when several precession frequencies are involved. Using equation 4.22 by implementing frequencies varying by more than 7% results in a beating, that increases the precession amplitude again after 800 ps. Such

behavior was not observed within the experiments. Unfortunately, the delay time was experimentally limited to 1 ns, so it is not confirmed experimentally whether the precession amplitude increases for a delay time  $\Delta\tau > 1$  ns. This would allow to find out how large the deviation from the central frequency is exactly. The results for the superposition compared to the fit to the measured data can be viewed in figure 4.7. Here it is already visible that by superpositioning several slightly varying frequencies around a central frequency, the amplitude decreases stronger than in the single frequency case. Even though the damping constant is not changed, the apparent damping is strongly increased.

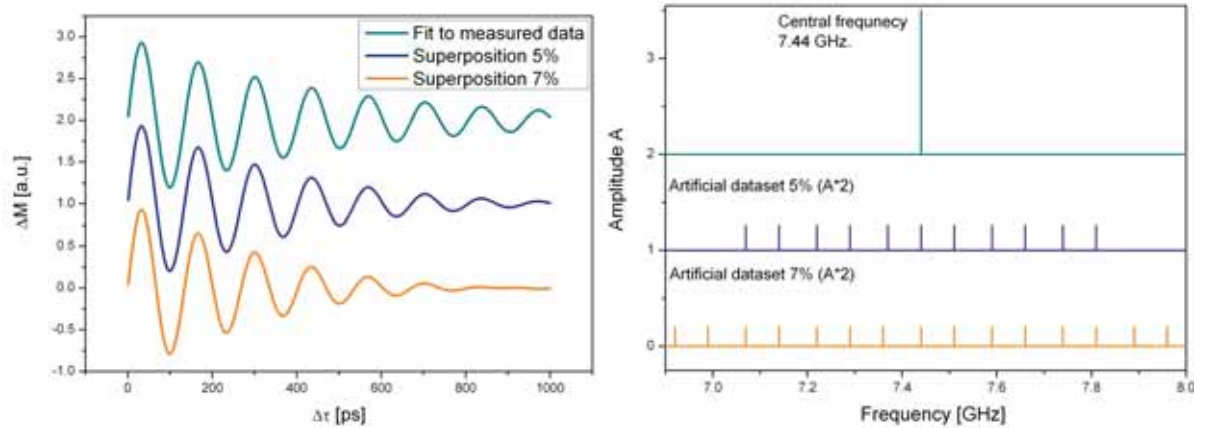


Figure 4.7: The fit to the measured data at 10 nm nickel layer thickness using a single sine function, compared to the artificially created spectra by the superposed functions with a frequency spectrum broadened by 5% and 7% (left). The frequencies involved into each superposition (right). The frequency amplitudes are divided by the number of frequencies involved.

To extract the apparent damping from the simulated artificial datasets, a single sine function model (equation 4.1) was fitted to these datasets again and the damping parameter was calculated according to the usual procedure. The broadening of the frequency by 5% resulted in a damping increase by 0.01 up to  $\alpha = 0.053$ . The 7% broadening even increased the damping parameter by 0.02 to  $\alpha = 0.063$ . The anisotropy field stayed constant at  $H_{ani} = 55$  mT, because there was no net frequency change in the "superposed" spectra. Varying the frequencies in equation 4.22 by 7% from the central frequency increased the beating over the exponential decay, so that fitting equation 4.1 did not match the superposition anymore. The variation of the frequencies by 5% in the sum function still allowed for a good fit to equation 4.1. Therefore, the latter will be considered for further calculations.

In the next step, reverse calculations were carried out with the data measured for a lower nickel thickness. In order to do this, data obtained at the 4 nm nickel thickness was chosen. At this thickness, the damping parameter is  $\alpha = 0.05 - 0.06$  for the different external fields. The simulation of the ripple effect on the data of the 10 nm

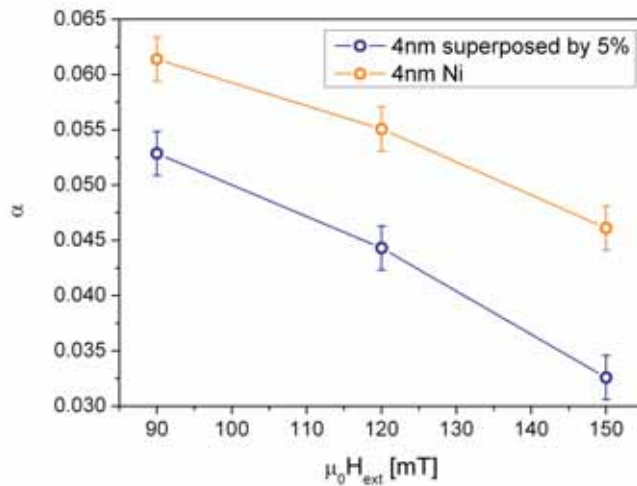


Figure 4.8: Damping parameter  $\alpha$  extracted from the measured data at 40 nm Ni, compared to the damping parameter calculated for the simulated artificial dataset from the superposed function for the 4 nm Ni.

thick nickel layer increased the value of the damping parameter to  $\alpha = 0.053$ , which is between the values obtained experimentally for the 4 nm thick nickel layer. In the reverse calculation a superposition function, equation 4.22, is fitted to the measured data for the 4 nm thick nickel layer and a different value for  $\tau_\alpha$ , the exponential decay, is obtained. The exponential decay increases by about 50%. The anisotropy field,  $H_{\text{ani}} \sim 400$  mT stays constant within this calculation. However, the increased  $\tau_\alpha$  leads to a smaller damping constant. It decreases to  $\alpha = 0.035 - 0.055$  for the different external magnetic fields that means, by about 0.01 for each field value. The corrected damping parameter values are around the experimentally obtained value of  $\alpha = 0.043$  for the 10 nm thick layer then, but still show a pronounced field dependence.

Thus, from figure 4.8 can be seen that the ripple effect can not be responsible for the total difference in the damping parameter obtained for nickel thicknesses below 10 nm in the different applied external magnetic fields. However, there are other effects contributing to measurement signal at these thicknesses. A major point is that for the thinner the nickel layer the measured spectrum has a much stronger exponential background, which has to be subtracted and makes a proper separation difficult. The higher the background of noncoherent excitations arises from a stronger demagnetization of the thinner films [6]. By fitting the measured spectrum to equation 4.1, the background  $B$  is also an exponential function containing parameters, which are fitted to the measured data. This leads to dependencies of the parameters, which can shift the exponential decay  $\tau_\alpha$  and then leads to a higher damping parameter  $\alpha$ . Especially for low external magnetic fields the precession amplitude measured on sample thicknesses below 10 nm is small and the precession frequency decreases, so that within one

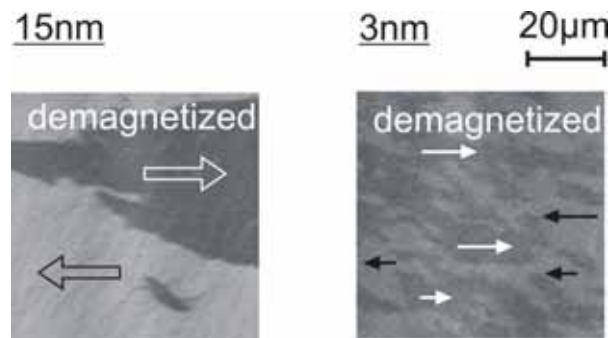
nanosecond only 2 or 3 precession periods can be recorded. Therefore, the inaccuracy in the parameters obtained from the fit increases, which contributes to a discrepancy between the damping parameters for the different magnetic fields.

To confirm a strong local variation of the anisotropy  $K_i$ , resulting in a frequency spread  $\nu_i$  below 10 nm, Kerr microscopy images have been examined. Here, the contrast does not allow to resolve ripple like fluctuations for field values higher than the saturation field. Therefore, the field range below was studied next.

The sample was situated in an external magnetic field oriented parallel to the sample surface. Two thicknesses were examined, one 15 nm and one 3 nm. In this experiment, the spatial magnetization distribution of the sample in an external field for each, one thickness below and one above 10 nm, was recorded. The Kerr microscope recordings are depicted in figure 4.9. In Figure 4.9a) the demagnetized sample at the two thicknesses, 15 nm (left) and 3 nm (right) is shown. Figure 4.9b) shows the recordings for the 15 nm thick layer and figure 4.9c) the recordings for the 3 nm thick layer. The depictions of the demagnetized sample already show that the domains in the 3 nm thick sample position are much smaller  $\leq 20 \mu\text{m}$ , than in the 15 nm thick sample position  $\sim 60 \mu\text{m}$ . Switching the external field from positive to negative, the magnetization turns almost uniformly from one to the other direction for the 15 nm thick layer, as can be taken from the pictures for 0.8 mT over 0 mT to  $-0.8 \text{ mT}$ .

At external fields larger than 1 mT domains of different directions build up. These domains are larger than  $20 \mu\text{m}$ . Further increasing the external fields, the domains of a single magnetization direction become larger. This is why by probing the sample with a laser spot of  $30 \mu\text{m}$  a macro spin behavior can be observed. The 3 nm thick nickel position on the other hand shows, several small domains of different magnetization directions turning, as the field magnitude grows. These domains are much smaller than  $20 \mu\text{m}$  and this way also smaller than the laser spot used to probe the time resolved magnetization change. The last picture on the bottom right in figure 4.9c) shows that even increasing the external field above saturation magnetization still leaves little domains pointing in slightly different directions. This considered to be the ripple effect, applied in the previous calculations, summing over differing precession frequencies. The decrease of the damping parameter  $\alpha$  for increasing external fields  $H_{ext}$  can be explained with different anisotropy fields  $H_{ani}$  involved. For the larger fields on one hand, the ripple effect becomes smaller since the deviation from the macroscopic magnetization direction are smaller. That means the frequency peak is sharper, the anisotropy field distribution smaller and the observed damping decreases. For lower external fields on the other hand, the ripple alignment is more distinct, the net anisotropy field is larger and so is the measured damping parameter. As mentioned above, the Kerr microscopy measurements were performed in an external field oriented in-plane, i.e. parallel to the sample surface. In the time-resolved MOKE measurements, the external magnetic field was oriented  $30^\circ$  out of plane. For this geometry, the ripple effect is expected to influence the sample even in fields larger than saturation magnetization.

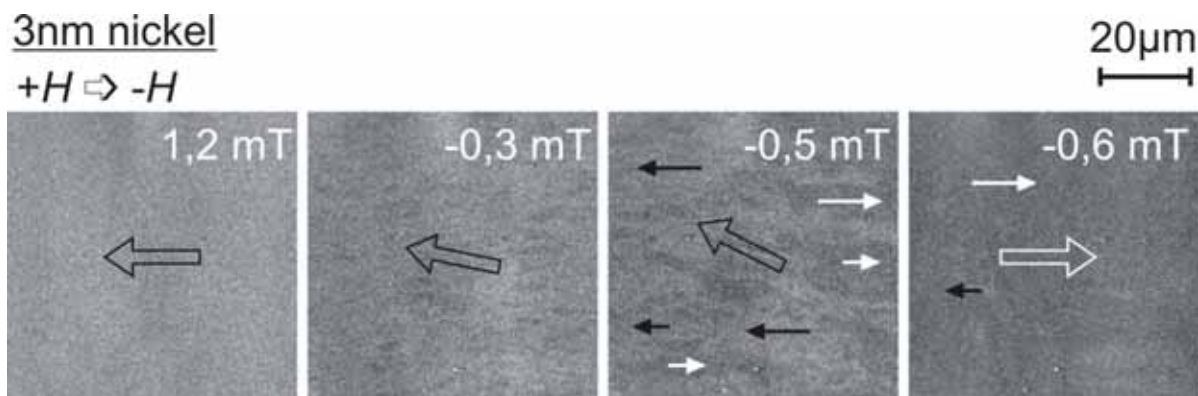
Concluding, it can be stated that the intrinsic damping of the nickel films studied is  $\alpha = 0.043(5)$ . The experimentally observed increase of damping for layers below 10 nm



(a) The domains of the demagnetized sample at 15 nm thickness (left) and at 3 nm (right).



(b) The domains, switching from positive to negative field, recorded at 15 nm nickel thickness.



(c) The domains, switching from positive to negative field, recorded at 3 nm nickel thickness.

Figure 4.9: Kerr microscopy recordings of the Si/ $x$  nm Ni sample with the external field applied in plane, along the wedge profile, provided by [12].

can be explained quantitatively by the occurring ripple effect. The increase in damping for lower external fields can be explained qualitatively from the Kerr microscopy recordings and the error arising from the subtracted background of the recorded signal. Unfortunately the Kerr angle resolution does not allow to see the extend of the ripple effect in external fields of the magnitude applied in our experiments.

## 4.3.2 Non-local Gilbert Damping with Vanadium

The non-local damping parameter is examined using a Si/Ni/V wedge sample. To determine the influence of an attached normal metal vanadium layer to the ferromagnetic nickel layer, two different samples were examined. First, with a constant vanadium layer thickness, Si/ $x$  nm Ni/3 nm V/1.5 nm Cu with  $1 \text{ nm} \leq x \leq 45 \text{ nm}$  and second, with a constant nickel layer thickness, Si/8 nm Ni/ $x$  nm V/2 nm Cu, with  $1 \text{ nm} \leq x \leq 45 \text{ nm}$ . The vanadium thickness for the sample was chosen to be 3 nm,

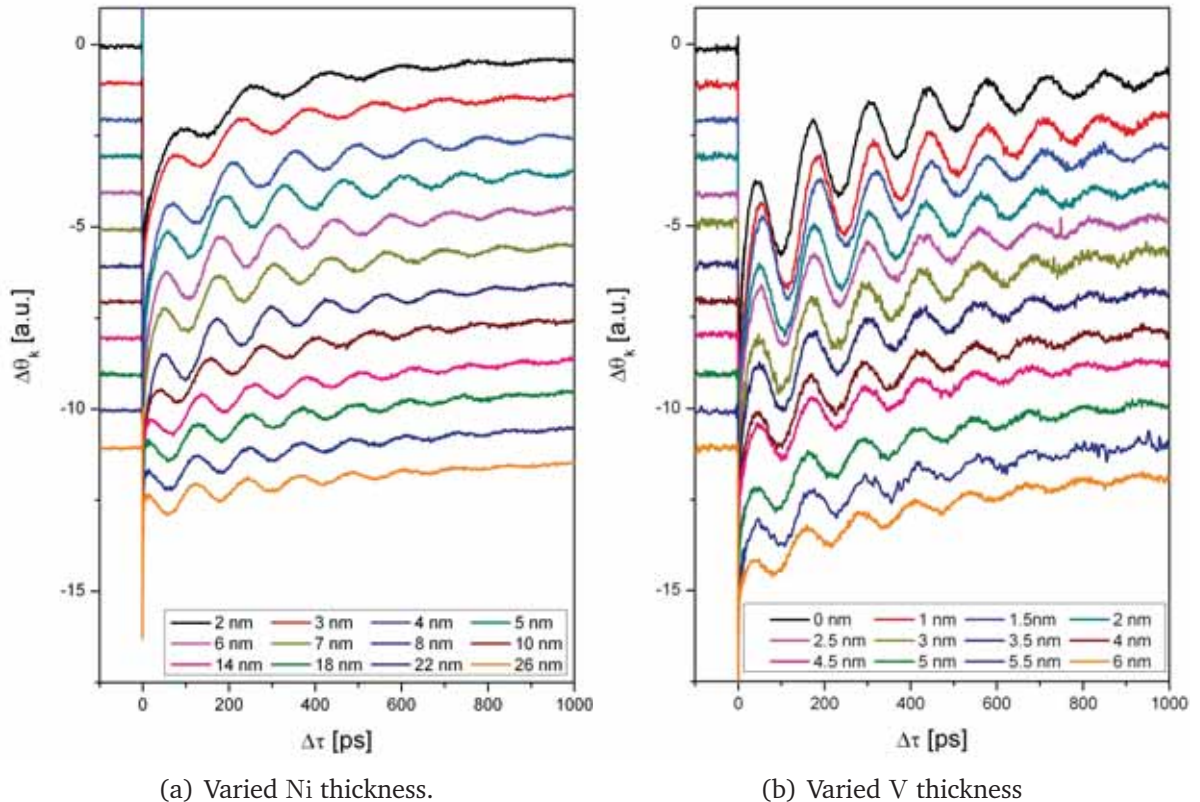


Figure 4.10: Spectra for varied nickel thickness from 1 – 28 nm measured on the Si/ $x$  nm Ni/3 nm V/1.5 nm Cu sample with a constant 3 nm vanadium layer (left) and on the sample Si/8 nm Ni/ $x$  nm V/2 nm Cu, with a constant 8 nm nickel layer and varied vanadium thickness from 0 – 6 nm (right) measured in an external field  $H_{ext} = 150 \text{ mT}$  oriented  $30^\circ$  out of plane.

because a thinner layer would have negligible influence on the damping. The MOKE signal on thicker layers is too weak, because not enough light is transmitted to be reflected on the nickel layer, where the Kerr rotation comes from. Therefore, the Si/8 nm Ni/ $x$  nm V/2 nm Cu sample with a constant nickel layer thickness could only be examined up to a vanadium thickness of 6 nm. At thicker vanadium layers, the recorded precession amplitude can no longer be distinguished from the noise. The

precession spectra for both samples, with the variable nickel layer thickness and the variable vanadium layer thickness are introduced in figure 4.10. The left side of figure 4.10 shows the spectra for a varied nickel thickness measured in a 150 mT external field. An increase in precession frequency is significant when increasing the nickel thickness up to 10 nm, after that the frequency stays constant. In the other case, when increasing the vanadium layer thickness, no change in frequency can be distinguished. The constant frequency predicts a constant anisotropy field for all vanadium thicknesses measured. At this point, no significant change in the damping parameter  $\alpha$  due to the vanadium layer thickness is expected.

In the following we will first analyze the sample with the varied vanadium thickness, before discussing the experimental results of the varied nickel layer sample. On

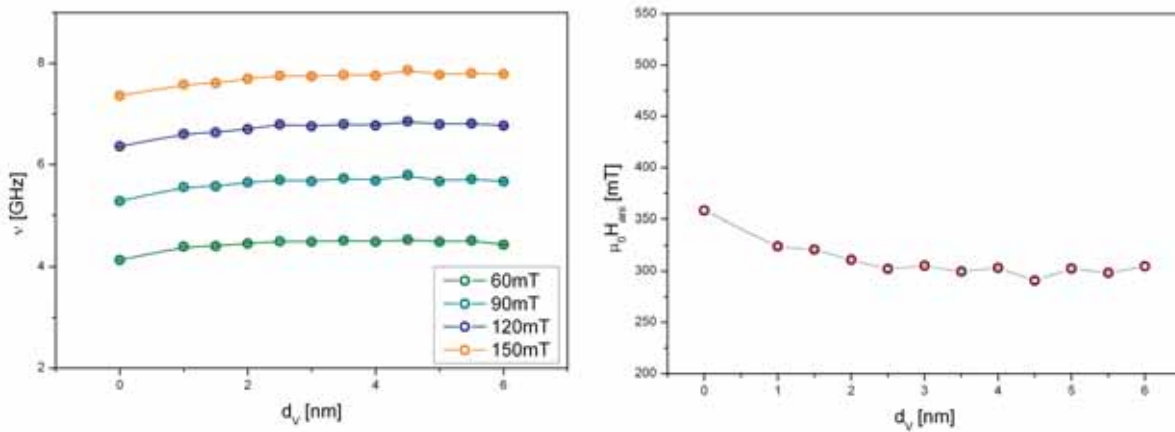


Figure 4.11: The precession frequencies  $\nu$  for different external fields  $H_{ext}$  (left) and the anisotropy fields  $H_{ani}$  (right) in respect of the vanadium layer thickness, measured on the Si/8 nm Ni/ $x$  nm V/2 nm Cu sample.

the left hand side in figure 4.11 can be seen more clearly than from the spectra that the precession frequency only slightly rises by about 0.2 GHz with the increase in the vanadium layer thickness. Consequently, the anisotropy drops slightly by around 20%, as the vanadium layer thickness increases from 0 – 2.5 nm. For larger thicknesses the anisotropy field stays constant at around 300 mT. These results indicate a relatively constant damping parameter  $\alpha$  independent from the vanadium layer thickness, especially for vanadium layers thicker than 2.5 nm.

The opposite is observed, when the nickel layer thickness is varied, as can be seen from figure 4.12. The precession frequency, shown on the left hand side, raises with the thickness of the nickel layer by about 2 GHz from 1 nm to 10 nm, in the same manner, as was already observed for the pure nickel wedge sample. For thicknesses above 10 nm there is no significant change in the precession frequency.

With the change in precession frequency also the anisotropy field  $H_{ani}$  changes. An increasing frequency usually implies a drop in the anisotropy field, so that in analogy to the frequency the anisotropy field decreases by about 50% as the the nickel layer

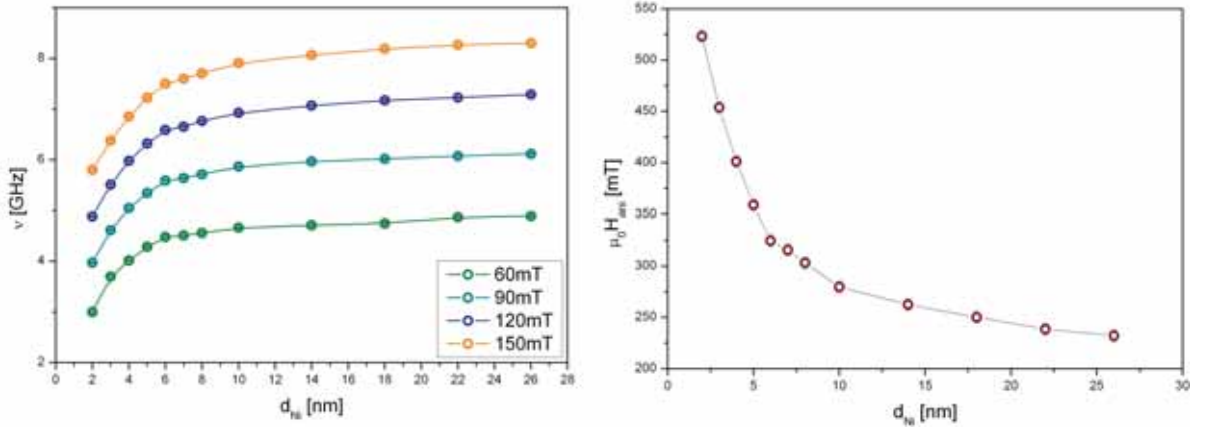


Figure 4.12: The precession frequencies  $\nu$  for different external fields  $H_{ext}$  (left) and the anisotropy fields  $H_{ani}$  (right) in respect of the nickel layer thickness, measured on the Si/ $x$  nm Ni/3 nm V/1.5 nm Cu sample.

thickness increases up to 10 nm. For nickel layers thicker than 10 nm the decrease of the anisotropy field becomes insignificant, but a slight change is still noticeable. Again, at this point we expect a drop in the damping parameter, when increasing the nickel layer thickness up to 10 nm and a rather constant  $\alpha$  for nickel layer thicknesses above 10 nm. From figure 4.13 can be seen that as concluded, vanadium does not have any influence on the damping parameter. Firstly, for the varied vanadium layer thicknesses,  $\alpha$  stays at a constant value of 0.040(5), which is around the value for the measurements on the pure nickel sample. The values also do not vary significantly for the different external fields applied. The slight drop of  $\alpha$  for the vanadium layer thickness above 5 nm originates from the bad reflection properties of vanadium. Secondly, there is no significant change in the damping parameter for the nickel layer thickness from 26 nm down to 10 nm, the value is about the value for the pure nickel layer measured. But in this case  $\alpha$  does not increase above the value of around 0.04 nm, until the nickel layer thickness decreases down to 5 nm. Only below a layer thickness of 5 nm the damping raises and shows a similar behavior as the reference pure nickel layer sample. It seems, that the vanadium layer has an influence on the ripple effect. This way, the increase of the damping parameter, a superposition of different precession frequencies, is repressed to lower nickel thicknesses. Once the damping rises for nickel thicknesses below 5 nm, the gap for the different applied magnetic fields arises, similar to the undamped nickel layer.

Comparing this result for non-local damping with the results presented in [7], it fits to the spin current model. For metals with  $Z < 50$ , namely aluminum  $Z = 13$  and copper  $Z = 29$ , the damping does not increase significantly, but stays at  $\alpha \approx 0.04$ . For palladium with  $Z = 46$  the value of alpha raises to about 0.05; dysprosium with  $Z = 66$  the damping increases to 0.065. Therefore, the negligible damping enhancement found out in our experiments with vanadium fits into this scheme.

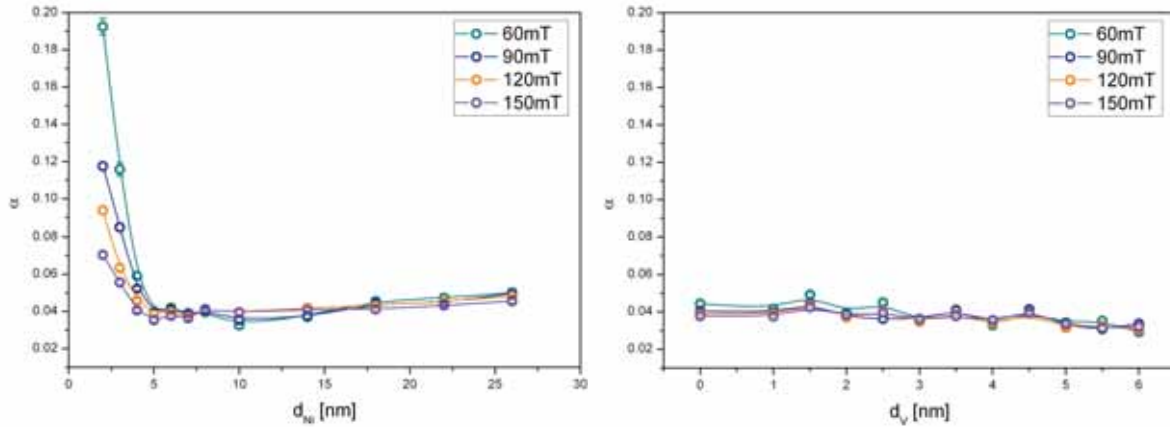


Figure 4.13: The damping parameters  $\alpha$  of the two samples. On the left side for varied nickel thicknesses with a constant vanadium damping layer thickness (Si/ $x$  nm Ni/3 nm V/1.5 nm Cu) and on the right side for a constant nickel layer thickness with a varied vanadium damping layer thickness (Si/8 nm Ni/ $x$  nm V/2 nm Cu).

#### 4.4 Results for the Local Gilbert Damping Experiments

In order to examine local Gilbert damping, four samples of 12 nm thickness were measured in the time resolved MOKE experiment, namely a pure permalloy sample,  $P_y$ , two samples doped with one and two percent dysprosium respectively,  $P_{y_1}Dy_{99}$  and  $P_{y_2}Dy_{98}$ , and one sample doped with two percent palladium,  $P_{y_2}Pd_{98}$ . These samples were prepared by MBE. The doping rate was estimated by the evaporation rates. To examine the outcome of these measurements on the permalloy samples doped by low percentage impurities we, will first have a look at the measured spectra. Beginning with figure 4.14, spectra for three differently doped samples measured in the same external field strength of 150 mT are presented. The impact of the impurities on the damping is already distinct from this depiction. For all three spectra the precession amplitudes are normalized to the same value. As a function of the delaytime  $\delta\tau$  however the amplitudes decline differently. For the undoped pure permalloy sample the precession amplitude barely declines after one nanosecond, as the top spectrum shows. In contrast to this, the amplitude of the two bottom spectra of samples doped with 2% palladium and dysprosium respectively, declines significantly after one nanosecond. The dysprosium doped sample is even damped stronger than the one doped with palladium.

Additionally, a look at the spectra measured in different external magnetic fields  $H_{ext}$  shows no change in precession frequency. In figure 4.15 the spectra for the pure 12 nm permalloy layer sample measured systematically in external fields of descending strength are depicted as an example. The spectra for the other samples show the same characteristics. This leads to the assumption, that damping is field independent and the same value for the damping constant  $\alpha$  should be calculated for all external fields

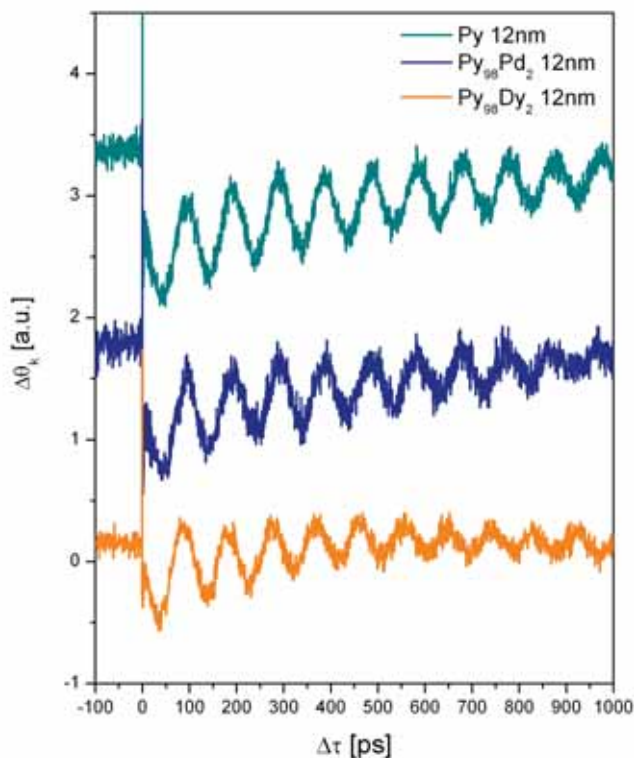


Figure 4.14: Spectra of three differently doped permalloy samples at the same external magnetic field, 150 mT and  $30^\circ$  out-of-plane. The beginning amplitudes of the three spectra are scaled to the same value.

occurring.

Further analysis confirms that the impurities indeed have an impact on the damping parameter. The next step, after extracting the precession frequency  $\nu$  and the decay time  $\tau_\alpha$ , is to find out the anisotropy fields. Figure 4.16 shows an increasing frequency, as the impurity amount is increased. The lowest frequencies occur for the pure permalloy sample. The doping with 2% palladium does not change the frequency significantly. However, the frequency is higher for the dysprosium doped sample and increases with the amount of dysprosium from 1% to 2%, which is clarified by the depiction of the anisotropy field versus the amount of impurities in figure 4.17. The anisotropy field increases linearly with the percentage of doping in this regime for dysprosium, by 100% per percentage of dopant, but increases only slightly for the 2% palladium doped sample. An influence on the anisotropy by rare earth doping is expected since the rare earths are highly anisotropic because of their 4f shell.

The final result, as assumed from the previous calculations, meets the expectations.

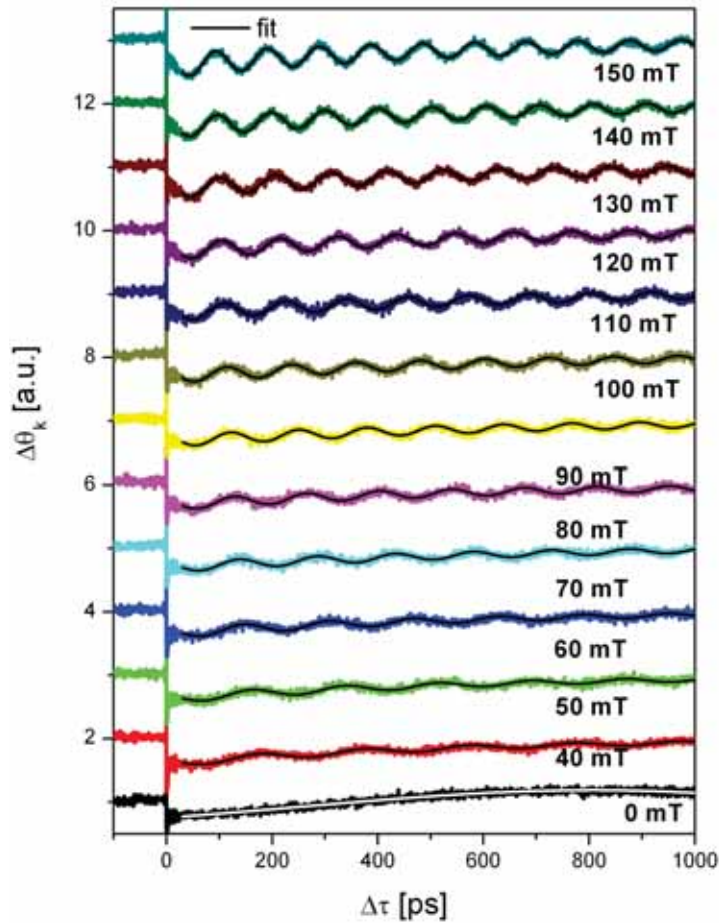


Figure 4.15: Spectra for the 12 nm pure permalloy sample measured in different external fields, in the  $30^\circ$  out-of-plane geometry and their fits.

As presented in figure 4.18, the damping is independent of the field, which means,  $\alpha$  is constant for the applied fields  $H_{ext}$ . The discrepancies appearing for the measurements in fields smaller than 90 mT are due to the fact, that precession amplitudes, as can be seen in figure 4.15, are small, and a precession is hardly recognizable. Furthermore, only two to three periods are observed in the spectrum. These two effects both make it more difficult to determine the appropriate decay time  $\tau_\alpha$ , so that the error for the estimated  $\alpha$  values in the small external fields is about twice as big as the calculated one.

The results show that dysprosium is a better damping material than palladium. The depiction in figure 4.19 makes it clear. One percent of dysprosium already has the effect of two percent of palladium impurities in the permalloy layer. The doping with dysprosium increases the damping parameter  $\alpha$  by about 50% per one percent of impurity. The results obtained performing these experiments, prove consistent with other experiments examining rare earth doped permalloy samples for damping.

Damping effects on rare earth doped permalloy were examined systematically by

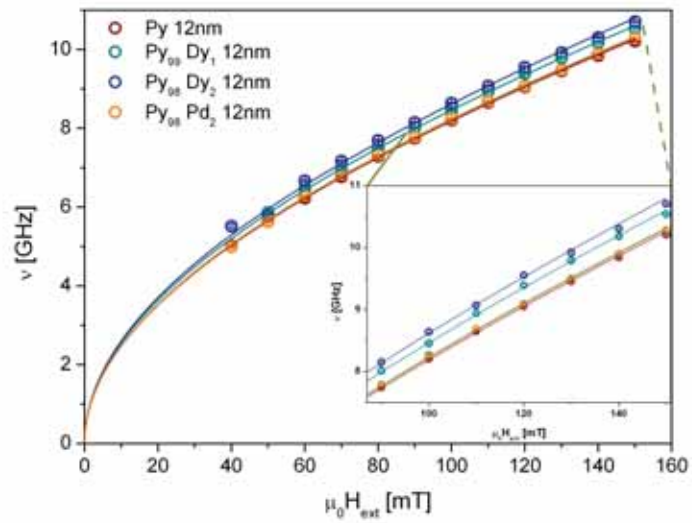


Figure 4.16: Precession frequencies for the differently doped permalloy samples, extracted from the measured spectra.

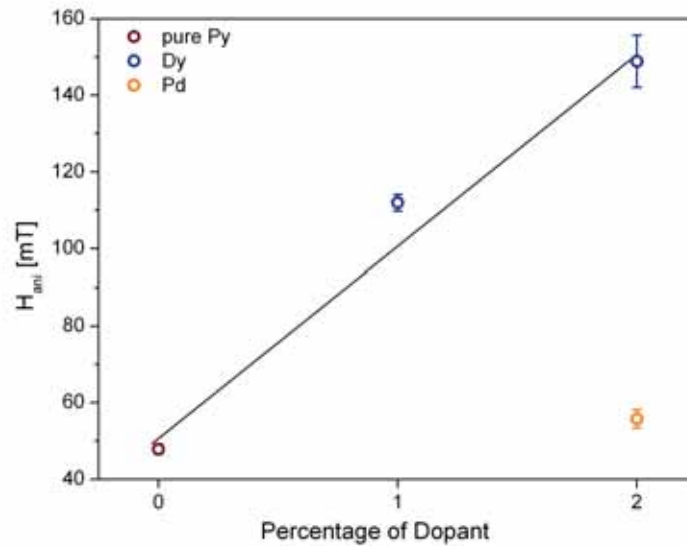


Figure 4.17: Anisotropy fields  $H_{ani}$  for the different impurities and amounts.

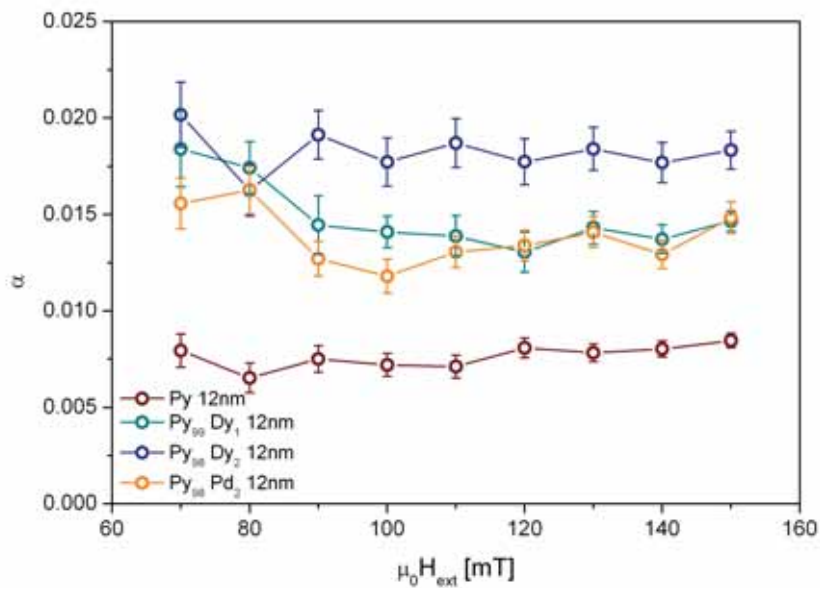


Figure 4.18: The damping parameter  $\alpha$  for the permalloy samples with different doping. Calculated using equation 4.3.

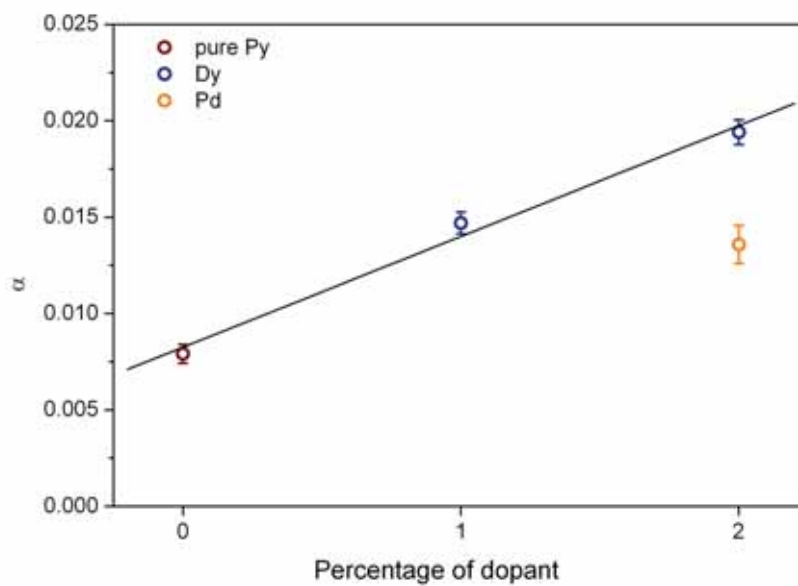


Figure 4.19: Comparison of the mean damping parameters for the differently doped samples.

Bailey et al. [21, 20, 22, 4] using the FMR technique. Samples were usually prepared using the cosputtering technique, obtaining permalloy thin films of 50 nm thickness with a uniform distribution of the impurities, give a damping parameter  $\alpha = 0.008$ . In 2006, Bailey et al. determined how the ion implantation technique, widely used in the semiconductor industry, can be used to produce low concentration impurity implantations into permalloy with a constant impurity concentration throughout the whole sample thickness [4]. Experiments with these samples reproduced the damping parameter values again. In [20] the estimated damping parameter is  $0.014 < \alpha < 0.043$  for samples doped with from 1% to 6% dysprosium. This agrees with the values determined in our all optical experiments. For the 1% dysprosium-doped sample, the damping is  $\alpha = 0.014$  and raises to  $\alpha = 0.02$  for the 2% dysprosium doped sample. There was no data found to compare the impact of palladium on the damping parameter, yet the extrinsic damping with transition metals is smaller than that of rare earths.

A novel theoretical explanation attempt for the additional extrinsic damping caused by rare earth impurities has been recently made by Hohlfeld [19]. Usually the s-d model has been chosen to describe the increase of damping by rare earth impurities. However, this model does not match the experimental data in [20]. The experiments show no increase in damping for samples doped with europium and gadolinium, but a constant ascent in damping for rare earth dopants from gadolinium to holmium. As far as europium and gadolinium are concerned, the s-d model also predicts no extrinsic damping for these. The failure of the s-d model begins, for the elements from terbium to ytterbium. The experimentally observed damping enhancement for terbium is slightly higher than predicted by the s-d model. For the following elements the damping enhancement even decreases in the s-d model, which is contrary to the experimental observations. The orbit-orbit model matches the experimental data for the elements europium to holmium and predicts a decreasing influence on damping for ytterbium. That is why Hohlfeld suggests this model, which accounts orbit-orbit coupling between the conduction electrons and the impurity ions. The conduction electrons orbital momentum of the ferromagnetic layer is coupled to the f electrons orbital momentum of the rare earth impurity in this model he found out a dependence of  $\alpha \propto (g_J - 2)^4$ . Magnetic moments need to be derived from their degrees of freedom. For the macro spin approximation the damping due to orbit-orbit coupling is of Gilbert form. The approach in this model is to apply a hamiltonian for the conduction, f and d electrons:

$$\hat{H} = \hat{H}_e + \hat{H}_f + \hat{H}_d. \quad (4.23)$$

This model should only hold for heavier rare earth metals, starting with samarium. It might fail for lighter elements, like cerium, where the fluctuations from valence electrons become significant. The first hamiltonian, the conduction electron hamiltonian  $\hat{H}_e = \sum_{k,\sigma} \epsilon_{k,\sigma} a_{k,\sigma}^\dagger a_{k,\sigma}$ , consists of the creation and annihilation operators with momentum  $k$  and spin  $\sigma$  and the energy  $\epsilon_{k,\sigma}$  of the conduction electrons including the Zeeman term. Secondly, for the localized rare-earth f electrons the kondo hamiltonian

$$\hat{H}_f = \Gamma \mathbf{S}_e \cdot \mathbf{S}_f + \lambda \mathbf{L}_e \cdot \mathbf{L}_f - \boldsymbol{\mu}_f \cdot \mathbf{H}. \quad (4.24)$$

holds. Here the  $\mathbf{S}_{e/f}$  and the  $\mathbf{L}_{e/f}$  are the spin and angular momentum, respectively. The first term, the spin-spin term is the s-f coupling used to reproduce the Curie temperatures in rare-earth metals. The prefactor  $\Gamma$  is of the order 0.1 eV. The last term is the Zeeman term. The middle term is essential for this model orbit-orbit. In order to get a nonzero contribution of the orbit-orbit term caused by a single impurity placed at the center, higher terms of the partial wave expansion for the conduction electron wave functions need to be included. The orbit-orbit prefactor  $\lambda$  is assumed to be a function relative to the angles of the  $\mathbf{k}$  vectors, this means that it is usually zero, except for  $k$  near the Fermi level. The unknown magnitude of  $\lambda$  is expected to be of the order of  $\Gamma$ . The two neglected terms in this model are first the spin-orbit term  $\mathbf{S}_e \cdot \mathbf{L}_f$ , because the crystalline electric field effect in transition metals is less than 0.1 meV. Apart from these, there is the spin-orbit coupling  $\mathbf{S}_f \cdot \mathbf{L}_f$  of the f electrons, which are in their ground state at room temperature, therefore this term does not contribute to the damping. The third hamiltonian in this compound, the Anderson Hamiltonian, for the host transition-metal ions in the absence of a Zeeman term is

$$\hat{H}_d = \epsilon_d d_\sigma^\dagger d_\sigma + \sum_k V_{kd} (a_{k,\sigma}^\dagger d_\sigma + d_\sigma^\dagger a_{k,\sigma}) + \frac{U}{8} \rho^2 - \frac{U}{2} \mathbf{S}_d \cdot \mathbf{S}_d - \boldsymbol{\mu}_d \cdot \mathbf{H}, \quad (4.25)$$

with  $\mathbf{S}_d$  being the spin operator of the d host electrons and the orbital momentum assumed to be quenched.  $V_{kd}$ , the virtual mixing parameter is of the order of 1 eV to 10 eV for transition metals, comparable to the Coulomb potential  $U$ . In order to establish spin independent orbit-orbit coupling between the d electrons and the f ions, the hybridization term between the conduction and d electrons is essential. For a decreasing  $V_{kd}$ , the localization of the magnetic moments increases and control the extent to which rare-earth-metal impurities enhance damping.

Conforming with this model, there is no additional damping by gadolinium impurities, since  $\mathbf{L}_f = 0$  as found out experimentally in [20]. Also doping with europium does not increase the damping. In this case it is believed that there are  $\text{Eu}^{2+}(4f^7)$  and not  $\text{Eu}^{3+}(4f^6)$  ions present, because then the f orbital moment is also zero. Also the double ionized state of ytterbium should not contribute to the damping. Besides this, the damping should increase when going from gadolinium to holonium, as the number of f moments increases.

For the palladium-doped sample the s-d model with the hamiltonian should hold:

$$\hat{H} = -J \mathbf{S}_e \cdot \mathbf{S}_d - \boldsymbol{\mu}_d \cdot \mathbf{S}_d. \quad (4.26)$$

This model predicts a smaller damping due to the smaller energies contributed as it is seen in the experiment.

## 4.5 Chapter Summary

The results show that all-optical pump probe experiments are a powerful tool to characterize magnetization dynamics on the sub nanosecond time scale, directly in the time domain.

Two different mechanisms for extrinsic damping have been introduced. One possibility is to increase the damping non-locally. The limits of the all-optical pump-probe technique arise from the penetration depth of the laser pulse for different materials. In the above examination of the sample damped with vanadium, the normal metal layer thickness was limited to 6 nm.

A qualitative explanation for the increase of damping in thin nickel layers below 10 nm was found and confirmed with Kerr microscopy. The experiments with vanadium as a non-local normal metal damping layer confirmed the spin-current theory, which predicts no significant increase in damping compared to the intrinsic damping of nickel and disqualifies vanadium as a damping material for non-local damping.

The other method to increase damping is a local one, namely by implementing impurities into the ferromagnetic material. The sample preparation for this method is technically more difficult to achieve. In order to implement a well defined and well distributed amount of impurities into a material, the deposition rate of both materials needs to be controlled simultaneously. For this purpose, equipment like MBE or cosputtering units are necessary. These techniques are more complicated and lead to smaller growth rates.

The magnetization precession damping with rare earths seems to be a promising way of damping, because the damping increases linearly with the impurity concentration [20]. Further experiments will prove whether the theoretical approach by Rebei and Hohlfeld [19] can describe the damping properties for the heavier rare-earths. One further interesting experiment would be to determine, whether higher impurity concentrations would increase the damping linearly and to which extend the damping parameter can be increased.

## 5 Summary

All-optical pump-probe experiments have been used to explore magnetization dynamics on the sub nanosecond time scale. This method is advantageous to the FMR technique, because the dynamics are observed directly in the time domain and do not have to be extracted from the frequency broadening of the magnetic resonance.

The two damping mechanisms introduced here have been partly examined in FMR and PIMMS experiments, so that some of the results could be compared directly with this work. First, the intrinsic damping of nickel was examined in order to have a reference for the following experiments. The damping parameter determined from the experiments for nickel layer thicknesses above 10 nm is  $\alpha = 0.043(5)$ . The observed increase in damping for layer thicknesses below 10 nm is explained with the magnetic ripple effect. The damping parameter dependence on the external magnetic field for the thinner layers is qualitatively explained with Kerr microscopy recordings.

One of the investigated damping mechanisms is the non-local damping. It was introduced with vanadium as a non-local damping layer, attached to a nickel layer. The low damping enhancement caused by the vanadium is expected and proves that the spin-current model is a valid explanation of this effect.

The second damping mechanism investigated is local damping by doping the ferromagnetic layer with low concentration impurities. The examined ferromagnetic material was permalloy. One sample was a 12 nm pure permalloy film, which provided the reference. The others were two samples doped with 1% and 2% dysprosium, respectively, and one doped with 2% palladium. The dysprosium-doped samples show a large damping enhancement, as expected for rare earths from the high anisotropy of the 4f shell. However, also palladium shows an increase in damping. The results obtained in our experiments conform with the results obtained by Bailey et al. for dysprosium doped permalloy [20]. The theoretical model was provided by Rebei and Hohlfeld [19]. Further experiments will show whether this model, which accounts orbit-orbit coupling for the damping enhancement caused by rare earth impurities, will hold for the heavier rare earths.

The results presented in this thesis show that magnetic damping is a broad field to be yet explored. The experiments carried out and described can be seen as a continuation of work done in the scope of a previous PhD thesis [7], where non-local Gilbert damping on nickel thin films with adjacent mainly transition metals as non magnetic damping layers, including palladium and chromium, as well as dysprosium, were systematically explored. In this thesis the damping properties of vanadium as a representative of the light transition metals were studied in contrast to the materials owning a high damping. Further expansions to use the all-optical approach to various problems in magnetization dynamics are currently made, by examining magnetization

dynamics of half-metals on  $\text{CrO}_2$  and nickel nanostructures [16].

## 5.1 Future Experiments

With this thesis we started to analyze the non-local damping coming from the 5B group transition metals. The light vanadium  $Z = 23$  does not cause any significant additional damping, as was expected from the theoretical model. It still needs to be confirmed that the damping should increase when going to niobium  $Z = 41$ , or to tantalum  $Z = 73$  in the 5B group; these should both show a larger additional damping, especially the latter.

Regarding the local damping in permalloy by rare-earths, it would be interesting to explore whether higher percentages of dysprosium alloyed into the permalloy influence the damping properties in the same way as found in the FMR experiments. Further, a systematic analysis, using the rare-earths from  $Z = 62$  to  $Z = 70$  as local damping materials, would show in how far the orbit-orbit coupling model is appropriate to describe damping by heavier rare earths with distinct f electrons. Especially terbium and holmium are very interesting, since for these materials a huge damping enhancement is predicted. Knowing these properties will give a better understanding of how to tailor materials with desired damping properties.

## 5.2 Other Techniques

One additional and very important technique to probe magnetization dynamics is the use of synchrotron radiation. Beam lines at synchrotrons can be tuned to use radiation of desired energies in the range of 100 eV to 1000 eV. The application of circularly or linearly polarized radiation produced in synchrotron light sources permits separate examination of the spin and orbital momentum, by tuning the beam energy to the desired absorption edges of the ferromagnetic material. The advantage of this method over the all-optical pump-probe experiments is the examination of element-specific single layers in multilayer alignments, but the time resolution of synchrotron pulses poses problems. Synchrotron pulse lengths depend on the electron bunches circulating in the storage rings. These bunches usually produce x-ray pulses of around 50 ps. In a special operation mode, called the low-alpha mode, x-ray pulses of only a few picoseconds duration (5 – 10 ps) can be achieved [2] at BESSY. Even shorter duration pulses can be created with the method called femtosecond slicing (fs-slicing). It produces x-ray pulses shorter than 150 fs [1] and is currently used at BESSY to study demagnetization processes, which happen on the timescale below one picosecond. However, in the future, an application of this technique is also imaginable for experiments on timescales up to one nanosecond, like the ones introduced in this thesis. Then, an examination of the magnetization dynamics for the ferromagnetic layer considered only could be recorded without the cross talk of the substrate and the non magnetic damping layer. This way the increase of the damping parameter for nickel thicknesses below 10 nm on

---

one hand, and the difference in damping for different external magnetic fields on the other hand may be understood better.



# Bibliography

- [1] *Status of the BESSY II femtosecond x-ray source*, 2004.
- [2] *Orbit stability in the 'low-alpha' optics of the BESSY light source*, 2006.
- [3] P. Bruno, Y. Suzuki, and C. Chappert, *Magneto-optical Kerr effect in a paramagnetic overlayer on a ferromagnetic substrate: A spin-polarized quantum size effect*, *Physical Review B* **53** (1996), 9214–9220.
- [4] V. Dasgupta, N. Litombe, W. E. Bailey, and H. Bakhru, *Ion implantation of rare-earth dopants in ferromagnetic thin films*, *Journal of Applied Physics* **99** (2006), 08G312.
- [5] O. de Haas, R. Schäfer, L. Schultz, K.-U. Barholz, and R. Mattheis, *Rotational magnetization processes in exchange biased  $\text{Ni}_{81}\text{Fe}_{19}/\text{Fe}_{50}\text{Mn}_{50}$  bilayers*, *JMMM* **260** (2003), 380–385.
- [6] M. Djordjević, M. Lüttich, P. Moschkau, P. Guderian, T. Kampfrath, R. G. Ulbrich, M. Münzenberg, W. Felsch, and J. S. Moodera, *Comprehensive view on ultrafast dynamics of ferromagnetic films*, *Phys. Stat. Sol* **3** (2006), 1347–1358.
- [7] Marija Djordjević Kaufmann, *Magnetization dynamics in all-optical pump-probe experiments: spin-wave modes and spin-current damping*, Ph.D. thesis, Georg-August-Universität, Göttingen, 2007.
- [8] Gerrit Eilers, *Grundlegende Untersuchungen zu Tunnelmagneto-widerstandselementen: Schichtrauigkeit, Tunnelbarriere und mikromagnetische simulationen*, Diplomathesis, Georg-August-Universität Göttingen, 2004.
- [9] M. Fähnle, *Nanosecond relaxation processes, theory and experiment*, SPP 1133 Workshop Göttingen, 2005.
- [10] M. Fähnle, R. Singer, D. Steiauf, and V.P. Antropov, *Role of nonequilibrium conduction electrons on the magnetization dynamics of ferromagnets in the  $s-d$  model*, *Physical Review B* **73** (2006), 172408.
- [11] Stefan Freundt, *Inerferometrische Kreuzkorrelation mit Titan-Saphir-Laserpulsen an GaAs*, Ph.D. thesis, Georg-August-Universität, 1994.
- [12] Christine Hamann, 2007, Kerr microscopy Measurements IFW Dresden.

- [13] Bert Koopmans, *Laser-induced magnetization dynamics*, Spin Dynamics in Confined Magnetic Structures II (B. Hillebrands and K. Ounadjela, eds.), Topics Appl. Phys., vol. 87, Springer-Verlag Berlin Heidelberg, 2003, pp. 253–320.
- [14] Mario Lüttich, *Wiederaufbau eines Titan-Saphir-Lasers und magnetische Simulation*, Diplomthesis, Georg-August-Universität, 2004.
- [15] A. T. J. Miltat and G. Albuquerque, *An introduction to micromagnetics in the dynamic regime*, Spin dynamics in Confined Magnetic Structures I (B. Hillebrands and K. Ounadjela, eds.), vol. 83, Springer-Verlag, Berlin Heidelberg, 2002, pp. 1–34.
- [16] Georg Müller, *Laser-induzierte Magnetisierungsdynamik in Halbmetallen und ferromagnetischen Nanostrukturen*, Diplomthesis, Georg-August-Universität Göttingen, 2007.
- [17] W. Nolting, *Grundkurs Theoretische Physik: Quantenmechanik*, vol. 5/1, Springer, Berlin, 2002.
- [18] J. O. Rantschler and C. Alexander, *Ripple field effect on high-frequency measurements of FeTiN films*, Journal of Applied Physics **93** (2003), 6665.
- [19] A. Rebei and J. Hohlfeld, *Origin of increase of damping in transition metals with rare-earth-metal impurities*, Physical Review Letters **97** (2006), 117601.
- [20] S.G. Reidy, L.Cheng, and W. E. Bailey, *Dopants for independent control of precessional frequency and damping in Ni<sub>81</sub>Fe<sub>19</sub> thin films*, Applied Physics Letters **8** (2003), 1254.
- [21] S. E. Russek, P. Kabos, R. D. McMichael, C.G. Lee, W. E. Bailey, R. Ewasko, and S. C. Sanders, *Magnetostriction and angular dependence of ferromagnetic resonance linewidth in tb-doped Ni<sub>0.8</sub>Fe<sub>0.2</sub> thin films*, Journal of Applied Physics **91** (2002), 8659.
- [22] H. Song, L. Cheng, and W. E. Bailey, *Systematic control of high-speed damping in doped/undoped Ni<sub>81</sub>Fe<sub>19</sub> (50 nm) bilayer thin films*, Journal of Applied Physics **95** (2004), 6592.
- [23] D. Steiauf and M. Fähnle, *Damping of spin dynamics in nanostructures: An ab – initio study*, Physical Review B **72** (2005), 064450.
- [24] J. Stöhr and H. C. Siegmann, *Magnetism from fundamentals to nanoscale dynamics*, Springer, Berlin Heidelberg, 2006.
- [25] Y. Tserkovnyak and A. Brataas, *Spin pumping and magnetization dynamics in metallic multilayers*, Physical Review B **66** (2002), 224403.

- [26] Y. Tserkovnyak, A. Brataas, and G. Bauer, *Enhanced gilbert damping in thin ferromagnetic films*, Physical Review Letters **88** (2002), 117601.
- [27] Y. Tserkovnyak, A. Brataas, G. E. W. Bauer, and B. I. Halperin, *Nonlocal magnetization dynamics in ferromagnetic heterostructures*, cond-mat **0409242 v3** (2006).
- [28] J.H. Van Vleck, *On the anisotropy of cubic ferromagnetic crystals*, Physical Review **52** (1937), 1178.
- [29] Chun-Yeol You and Sung-Chul Shin, *Generalized analytic formulae for magneto-optical kerr effects*, Journal of Applied Physics **84** (1998), no. 1, 541–546.
- [30] S. Zhang and Z. Li, *Roles of nonequilibrium conduction electrons on the magnetization dynamics of ferromagnets*, Physical Review Letters **93** (2004), 127204.



# Danksagung

An dieser Stelle möchte ich mich noch bei all denjenigen, die mich während des Studiums und der Entstehung dieser Arbeit begleitet haben, bedanken.

Zuerst gilt der Dank Herrn *Professor Markus Münzenberg* für die Aufnahme in seine Arbeitsgruppe und das interessante Thema, das nicht ausgeschöpft wurde. Sein mir von Anfang an entgegengebrachtes Vertrauen und seine Diskussionsbereitschaft waren eine große Hilfe.

Herrn *Professor Reiner Kirchheim* danke ich für die Übernahme des Korreferats.

Marija Djordjević Kaufmann und Kai Bröking gilt der Dank für die gewissenhafte Korrektur dieser Arbeit.

Für die Experimentelle Zusammenarbeit im fs-Labor bedanke ich mich bei Marija Djordjević Kaufmann, Georg Müller und Zhao Wang. Für die Hilfestellung bei der Herstellung von Proben geht der Dank an Gerrit Eilers und Anne Parge.

Bei meinen Bürokollegen Gerrit Eilers und Zhao Wang bedanke ich mich für die gute Atmosphäre.

Meinen Eltern und meiner Schwester danke ich, nicht nur für die Finanzierung des Studiums, sondern auch für ihre fortwährende Unterstützung und Geduld.

Als nächstes folgt eine Aufzählung von Freunden, die das Programm außerhalb des Studiums gefüllt haben, und zum Teil (die anderen werden trotzdem mit aufgezählt) Wert darauf legen, an dieser Stelle namentlich aufzutauchen: Britta Kreilein, Philipp Willroth, Kai Bröking, Daniel Broxtermann, Nina Grabinski, Simon Hügelmeier, Katharina Lesch und Thomas Rademacher.